Polar Auroral Arcs

Anita Kullen

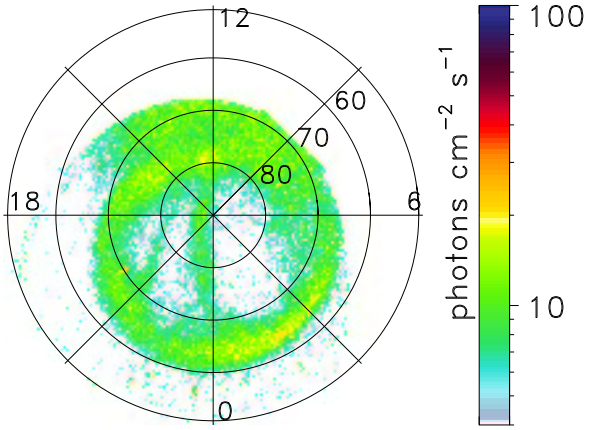

Doctoral Thesis
Alfvén Laboratory
Division of Plasma Physics
Royal Institute of Technology

Stockholm 2003

The cover picture shows an ultraviolet image of a theta aurora in the northern ionosphere taken by Polar UVI at 22:30 UT on 11 February 1999.

ISBN 91-7283-541-9

Printed by Universitetsservice US AB, Stockholm 2003.

Kullen, Anita

Polar auroral arcs

Doctoral Thesis.
Division of Plasma Physics, Alfvén Laboratory, KTH, Stockholm, Sweden.
May, 2003.

Abstract
This thesis focuses on large-scale auroral arcs which occur poleward of the main auroral oval. The work consists of two parts: The first part is a statistical study where the role of the solar wind for the occurrence and evolution of polar arcs is investigated. The second part consists of a model explaining polewardly moving arcs in terms of large-scale changes of the magnetotail topology.

The statistical study is based on UV images of the auroral oval provided by the Polar satellite and solar wind data from the ACE spacecraft. The study confirms many previous results regarding the strong dependence of the evolution of polar arcs on the direction of the interplanetary magnetic field (IMF): northward IMF seems to be a precondition for most polar arcs to occur, the east-west component of the IMF (IMF B_y) controls the location of the arcs. A new finding is the correlation between arc occurrence and high values of the solar wind energy flux. Based on their spatial evolution a new categorization of polar arcs is presented. It is shown that each polar arc type appears for a characteristic combination of solar wind parameters.

The model developed in this thesis explains the evolution of those polar arcs which typically occur after an IMF B_y sign change. It is shown that an IMF B_y induced twisting of the magnetotail changes after an IMF B_y sign reversal successively such that in an intermediate state near-Earth and far tail regions are oppositely twisted. Field lines originating in the high-latitude region of the far tail plasma sheet map high into the near-Earth tail lobes producing in the ionosphere a bridge of closed field lines which spans the entire polar cap. The tailward propagation of the twist rotation corresponds to a poleward motion of the closed field line bridge. This bridge is interpreted as the mapped region of a moving polar arc. In a first step it is demonstrated with a modification of the T89 model that a tail magnetic field topology as described above actually leads to a bifurcation of the polar cap boundary. In a second step these ideas are tested with the GUMICS-4 code, a magnetohydrodynamic model. Different constant IMF clock angle cases and IMF B_y sign change runs are examined in detail leading to a refinement of the polar arc model. The importance of northward IMF becomes clear from the simulation results: Only during northward IMF does non-zero IMF B_y lead to a long and highly twisted tail which makes a displacement of closed field lines into the polar cap possible.

Keywords: polar arc, transpolar arc, interplanetary magnetic field (IMF), solar wind-magnetosphere coupling, magnetotail twist.

Contents

Acknowledgments

I am grateful to Prof. Göran Marklund and Dr. Lars Blomberg for giving me the possibility to perform PhD studies at the Alfvén Laboratory. The space plasma group has been a stimulating environment, not only due to the highly qualified scientists but also due to the nice atmosphere among the colleagues, including the administration staff. I was especially lucky to have such nice office mates as Dr. Nickolay Ivchenko during the first years and later Sónia Figueiredo.

I thank my supervisor Dr. Lars Blomberg for his support, his encouragement to connect with other researchers abroad, and for the high degree of freedom he gave me in performing this thesis. The work benefited a lot from numerous scientific discussions with all members of the group. I would like to acknowledge in particular Dr. Tomas Karlsson and Dr. Nickolay Ivchenko. Their continuous interest in the progress of my work and the numerous debates we had about physics were invaluable for me. Special thanks to Bengt-Harald Nilsson who kept the computers always running and was reachable all-day round in emergency cases.

For the possibility to spend two entire summers at the University of Washington, Seattle, I express my gratitude to Prof. George Parks and Dr. Mitch Brittnacher. Dr. Mitch Brittnacher, functioning as my supervisor in Seattle, helped using and interpreting Polar UVI data and always carefully listened to my ideas. Without his encouragement, I would never have started the comprehensive statistical work on polar arcs.

Many thanks to Dr. Pekka Janhunen at FMI, Helsinki, for giving me the possibility to work on MHD simulations with his GUMICS-4 code. He gave me not only practical help with the evaluation of the simulation runs but also took the time to answer my numerous scientific questions. With his broad knowledge and deep insight into physics it was a real pleasure discussing research with him.

These last years would never have been as interesting, as chaotic and as fun if there would not be my two children Mikael and Anna, born during this time. Numerous babysitters helping out on many different occasions did not only make it practically possible to perform this thesis but also helped a great deal keeping up the courage. My warmest thanks go to Antje Grots and to my brothers Hans and Kai for all those months they took care of the children in such a perfect way. Also the French and German grandparents 'hopped in'

whenever needed, and spoiled their grandchildren to the maximum. My brother Rolf deserves to be mentioned for his moral support. Thanks to my father who, despite occasional ironic comments about 'spending the beauty of youth in front of formulas', always encouraged me to fulfill my studies properly. Most of all, I am indebted to my husband Olivier, for giving up Paris for Stockholm, for his patience and support during the course of this work (it was indeed needed), and last but not least for introducing proper (French) food at home.

I am happy that so many people I met during the recent years became close friends. Thanks to Regine Hock, Gesa Weyhenmeyer, Anneli Gustafsson, Claes Håkansson, Wendy Kreß, Till Burkert and Martin Wendt for all the nice time we spent together, and I apologize for leaving out my friends back in old Germany, many of which I had the pleasure to see as guests in our home.

List of papers

The thesis is based on the papers listed below. In the introduction part they are referred to as Paper 1 - Paper 4.

1. Kullen, A. and L. G. Blomberg, The influence of IMF B_y on the mapping between the Earth's magnetotail and its ionosphere, *Geophys. Res. Lett., 23*, 256, 1996.

2. Kullen, A., The connection between transpolar arcs and magnetotail rotation, *Geophys. Res. Lett., 27*, 73, 2000.

3. Kullen, A., M. Brittnacher, J. A. Cumnock, and L. G. Blomberg, Solar wind dependence of the occurrence and motion of polar auroral arcs: a statistical study, *J. Geophys. Res., 107*, 1362, Nov 2002.

4. Kullen A., and P. Janhunen, Relation of polar auroral arcs to magnetotail twisting and IMF rotations: a systematic MHD simulation study, submitted to *Ann. Geophys*, 2003.

Chapter 1

Introduction

Polar lights have stirred man's imagination, curiosity and fear probably as long as Earth has been inhabited. There are numerous descriptions of the aurora preserved from many different historical epochs and cultures (Eather, 1980). In regions where the aurora rarely occurs, people became horrified when suddenly mysteriously moving curtains of light appeared in the sky. Reports of auroral observations speak of flames or battlefields forming in the night sky. These visions were often interpreted as an omen of forthcoming calamity. In the myths and tales of people living in the arctic regions where the aurora is a recurrent phenomenon many references to it can be found. The most widespread interpretation in mythology is that of it being the spirits of the dead, who, depending on the local version fight or play ball with each other.

There were few scientific attempts to explain the aurora before modern times. Probably the first attempt for a scientific explanation was, as of many other subjects, given by Aristoteles. In his book 'Meteorologica' around 350 B.C. he suggested that heat from the Sun causes a vapor to rise from the Earth's surface and collide with the element fire which then bursts into flame. A remarkable discussion of aurorae appears in 'The kings mirror', a medieval Norwegian chronicle: "However, it is true of northern lights as of many others of which we have no sure knowledge, that thoughtful men will form opinions and conjectures about it and will make such guesses as seem reasonable and likely to be true. Some think [...] it is possible that these lights shine forth from the fires that encircle the outer ocean. Others have suggested that during the hours of night when the Sun's course is beneath the Earth, an occasional gleam of its light may shoot up into the sky [...] But there are still others who believe that the frost and the glaciers have become so powerful there that they are able to radiate forth these flames."

700 years had to pass until a deeper understanding of the northern lights was reached. It was not before the discovery of the electron and how its motion is governed by electric and magnetic fields, that the foundation for our present

understanding of auroral lights has been established. In the 19th century, the classical electromagnetic theory was developed. The discovery of the atom and its dissociation into electron and nucleus followed at the turn of the century. In the 1950's 'space age' began with rocket and satellite experiments allowing in-situ measurements in space. Now, that researchers could measure directly in space a much better knowledge about polar lights and the near-Earth space environment was gained.

Today we know that the aurora is mainly caused by electrons moving with high speed from space towards the Earth until they collide with gas particles of the outer atmosphere some 100 km above the Earth. These collisions cause gas particles to release energy in the form of light. Depending on the atmospheric particle hit, the light has a different wavelength, i.e., the aurora has another color. These light emissions are produced day and night by a never ending stream of electrons flowing into the atmosphere in the arctic regions. The northern lights are actually accompanied by southern lights. This can be seen from beautiful satellite images of the nightside Earth as the one shown in the left image of Figure 1.2. The aurora forms huge ovals around the northern and southern magnetic poles with a thickness of about 200 km and a diameter of about 1500 km.

The reason why the aurora could be observed by Chinese, Greek and Roman scholars although they lived far from the arctic regions, is its dynamic reaction on solar activity. The Sun not only radiates light, it also emits continuously a thin gas of charged particles, the solar wind. The solar wind is sensitive to electric currents and magnetic fields, such that it interacts with the Earth's own magnetic field in a complicated way. At times, the Sun is more active and massive eruptions on its surface appear which are felt as geomagnetic storms at the Earth. The geomagnetic field becomes strongly disturbed, the aurora brightens and the entire auroral ovals expand to lower latitudes.

The formation of an auroral oval is fairly well understood. The currents producing the aurora flow along magnetic field lines. Knowing the magnetic field topology in the near-Earth space gives the location of the aurora. The Earth's dipole field creates a comet-like cavity in the solar wind flow, called the magnetosphere, in which the geomagnetic field dominates. Due to the strongly deformed magnetospheric field, field-aligned currents encounter the Earth atmosphere in a zone extending over 5-10 degrees latitudes around the magnetic poles.

At the beginning of the 1980's the first global satellite images of the auroral oval became available. In 1981 a surprising image was received from the DE-1 spacecraft (Frank et al., 1982). A broad band of aurora was seen in the middle of the auroral oval, reaching from the nightside to the dayside part of the oval. It was named 'transpolar arc', others called the arising auroral morphology 'theta aurora' due to its resemblance with the Greek letter θ. The right image of Figure 1.2 shows a typical transpolar arcs. Scientists were astonished by this finding. Applying standard magnetosphere models, auroral arcs are not

Figure 1.1: Auroral display near Fairbanks on 1 March 2003 (Photo: J. Curtis).

expected to occur inside the auroral oval. Since the first transpolar arc was reported many more large-scale auroral arcs have been detected poleward of the oval, showing a variety of different shapes and motions. Not all stretch over the entire oval, their length varies between about 100 km (small-scale sun-aligned arcs) and about 4000 km (transpolar arcs). Small-scale sun-aligned arcs were actually known much before as they are easily detected from the ground (the first scientific report has been written by (Mawson, 1916)) but, their origin is even less understood. To use a correct description that includes all types of arcs poleward of the auroral oval, the expression 'polar auroral arcs' is used from here on. Despite many detailed studies, a complete understanding of polar auroral arcs is still missing.

The subject of this thesis is the investigation of large-scale polar auroral arcs. It is examined when and why they occur, how they are connected to

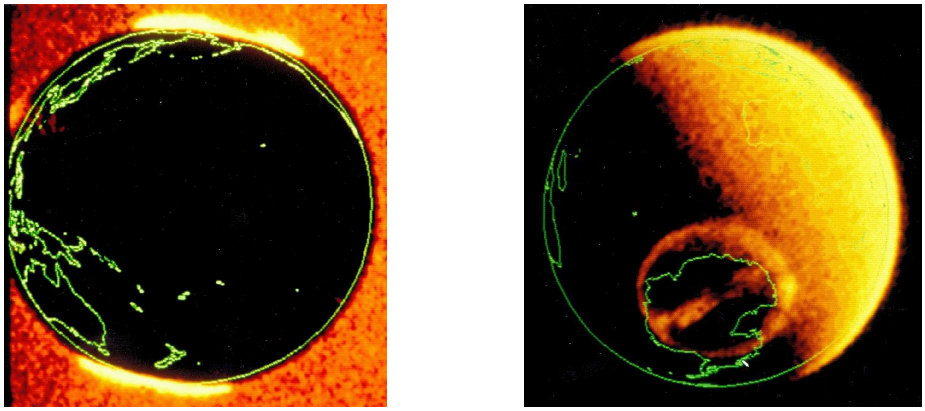

Figure 1.2: Global auroral UV images taken by the DE-1 spacecraft. Left: The northern and southern auroral ovals. Right: a transpolar arc (DE-1 SAI Photo Gallery).

the magnetosphere topology and to what extent the solar wind influences their appearance. In the next two chapters a short introduction to space plasma physics is given. It covers the physics of the magnetosphere and ionosphere. It follows a description of the magnetosphere models used to investigate the connection between magnetosphere and polar arcs (chapter 4) and a description of spacecraft instruments used for a statistical study of polar arcs (chapter 5). The results of this work and outstanding problems are summarized in the last chapter. The scientific work is presented in the form of four papers published in (Paper 1-3) or submitted to international scientific journals (Paper 4).

Chapter 2

Sun-Earth environment

2.1 The solar wind and the magnetosphere

The physical characteristics in the Earth's magnetosphere are defined mainly by two entities, the solar wind and the geomagnetic field. Understanding their interaction is a major goal of space plasma physics. It allows not only to understand the near Earth space environment but also how the space environment of other planets forms.

The Sun's interior consists of a highly ionized gas, called a plasma. In the extremely dense core of the Sun nuclear reactions take place that create temperatures exceeding the binding energies of the atoms. The ionization is caused by collisions in the heated gas. Due to a huge difference in pressure between the Sun and the surrounding space, the solar plasma spreads deep into space where it is referred to as the solar wind. Some characteristic values of the solar wind and other space plasmas are found in Table 2.1.

The solar wind reaches the Earth after about 3-4 days and has near the Earth typical velocities of about 450 km/s.

Table 2.1: Properties of different plasma populations in space

Plasma population	n_e (m^{-3})	T_e (K)	λ_D (m)	B (nT)	Chemical composition
Interior of Sun	10^2	10^7	7×10^{-9}	1×10^8	H^+, He^{++}
Solar wind	10^7	10^5	7×10^1	5	H^+, He^{++}
Plasma sheet	10^6	10^7	2×10^2	10	O^+, He^+, H^+
Tail lobes	10^4	10^5	4×10^2	25	O^+, He^+, H^+
Ionosphere	10^{12}	10^3	2×10^{-3}	5×10^4	$NO^+, O_2^+, O^+, He^+, H^+$

It does not encounter the Earth's atmosphere directly. The strong magnetic field of the Earth shields the near-Earth environment such that the solar wind is forced to flow around the cavity dominated by the terrestrial field. This cavity is called the magnetosphere. On the dayside the magnetosphere is compressed by the solar wind, on the nightside it forms an up to 200 Earth radii (R_E) long tail, the magnetotail. Due to its interaction with the solar wind the magnetosphere has a complicated structure, containing several current systems and regions of different plasma populations. Figure 2.1 illustrates the main regions within the magnetosphere.

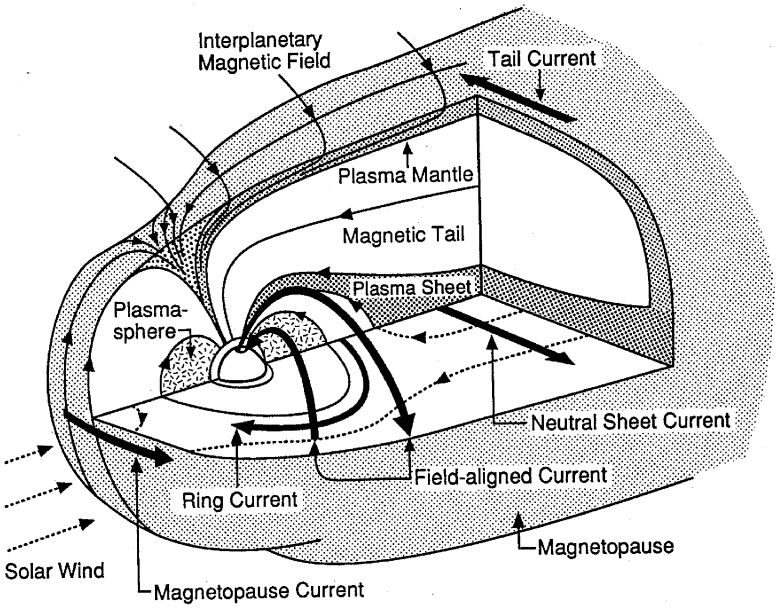

Figure 2.1: Schematic representation of the Earth's magnetosphere (Kivelson and Russell, 1995).

The magnetic field of the Earth is in a first approximation a dipole field that is generated in the fluid outer core of the Earth by a self-exciting dynamo process. Electrical currents flowing in the slowly moving molten iron generate the magnetic field. Near the surface of the Earth the geomagnetic field has a magnitude of about 30000 nT. It decreases as r^{-3} radially outward. At a distance of about 10 R_E the magnetic pressure of the geomagnetic dipole field is reduced to such an extent that its value is comparable to the kinetic pressure of the solar wind. At that distance sunward of the Earth the boundary between solar wind and magnetosphere (the magnetopause) forms. Along the magne-

topause the charged solar wind particles are repelled by the strong geomagnetic dipole field. Depending on their charge they gyrate in the presence of the geomagnetic field in different directions carrying a net current in the duskward direction. The magnetopause current shields and compresses the Earth dipole field at the same time. It closes along the tailward part of the magnetopause. Due to the supersonic speed of the solar wind, a bow shock appears in front of the magnetopause which makes the physics in this region more complicated than sketched here. The decelerated and heated solar wind plasma in the bow shock region moves in a several R_E wide layer, called magnetosheath, around the magnetopause.

Inside the magnetosphere two large-scale current systems appear. The ring current flows at a distance of 4 to 8 R_E in westward direction around the Earth and further compresses the geomagnetic field inside this region. On the tailward side, the ring current merges smoothly into the neutral sheet current (also called cross-tail current). The neutral sheet current flows in an 8 R_E thick sheet along the equatorial plane of the magnetotail and closes as the tail current along the northern and southern parts of the tail magnetopause. Seen from the Sun, the tail currents form a theta like current system. The cross-tail current is connected to a tailward stretching of the magnetotail field lines. Both the ring and the tail current systems are connected to a non-uniformity of the surrounding magnetic field. The magnetic field gradient causes a drift in opposite direction for oppositely charged particles such that a net current occurs.

The current systems and associated magnetic field regions are embedded in plasma regions of different densities and temperatures. In steady state, the plasma tries to fill regions of weak magnetic fields to balance the total pressure. The tail current sheet with its weak magnetic field consists of plasma with a high plasma pressure. This region is called the plasma sheet. At higher latitudes the magnetic field strength increases. The two low-pressure regions north and south of the plasma sheet are denoted as the lobes.

The highest density of high-energetic particles is found in the two Van-Allen belts. Their particle populations contribute to the ring current. The very high density occurs because in the belt regions the topology of the magnetic field resembles bottle throats at its northern and southern ends in which charged particles are trapped. The high-energetic particles are created by cosmic rays inside these belts. They are mirrored at the bottle ends and thus, bounce back and forth between the high latitude regions of the Earth.

2.2 The interplanetary magnetic field

The solar wind contains a weak magnetic field, called the interplanetary magnetic field (IMF). In the near-Earth space environment the IMF consists mainly of the Suns own magnetic field. It is generated by large-scale motions of conducting fluids operating just below the convective zone of the Sun. Near the

Sun this field is highly variable, further out it has a more dipole-like structure. The solar magnetic field is carried by the solar wind outward from the Sun such that its field lines become stretched and enclose a heliospheric current sheet. Due to the rotation of the Sun, the field lines do not point radially outward, but form an Archimedean spiral. The heliospheric current sheet is nonuniform and unfolds like a ballerina skirt around the Sun-Earth plane. From an observer on the Earth this is registered as frequent variations of the IMF.

When studying the magnetosphere, the direction of the IMF is usually given in GSM coordinates. In this coordinate system, the x-axis points from the Earth to the Sun and the y-axis lies perpendicular to the Earth's magnetic dipole so that the xz-plane contains the dipole axis. The positive z-axis is in the same sense as the northern magnetic pole. An expression used frequently for describing the relation between the IMF B_y and IMF B_z components is the IMF clock angle. It is the angle between the IMF vector in the yz-plane and the positive z-axis ranging from 0 degrees for pure northward to 180 degrees for pure southward IMF. The average distribution of the IMF near the Earth is shown in Figure 2.2. It shows that the IMF B_x and B_y components have usually opposite signs and are larger than the IMF B_z component. This is due to the spiral form of the IMF lines, making at 1 AU an angle of about 45° to the x-axis. Typical values of the IMF near the Earth are 5-10 nT but can rise up to 30 nT.

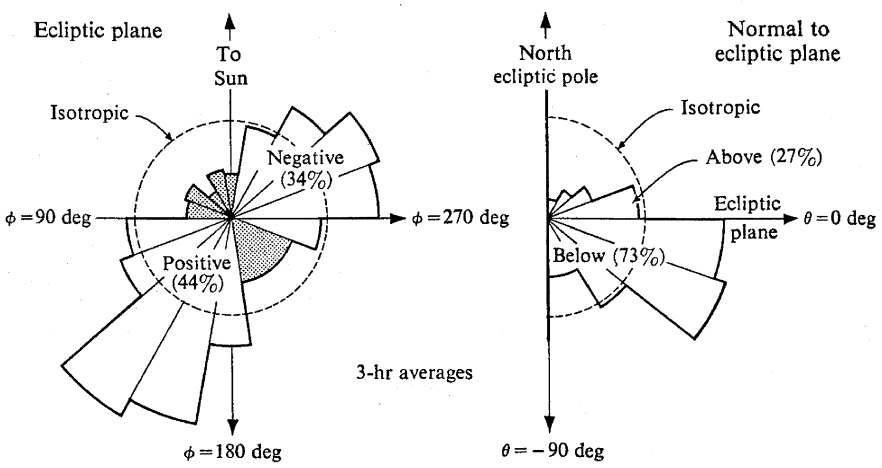

Figure 2.2: The average distribution of the IMF at 1 AU (Wilcox and Ness, 1965).

The energy density of the interplanetary magnetic field (IMF) is negligible compared to the kinetic energy density of the solar wind. Consequently the shape of the magnetosphere is mainly defined by the solar wind flow. However,

the shielding of the magnetosphere from the solar wind is not complete. Due to the existence of the IMF, a small amount of mass and energy is transported into the magnetosphere. The degree of the solar wind-magnetosphere coupling depends strongly on the direction of the IMF. Several energy coupling parameters have been proposed that show a good correlation with the level of geomagnetic activity in the auroral zones (AE index). They all involve the solar wind velocity and the IMF and indicate that the solar wind energy input is much higher during southward than during northward IMF. One well-known parameter is the Akasofu-Perreault epsilon parameter $\epsilon = vB^2 sin^4(\theta/2) l_0^2/\mu_0$ where θ is the IMF clock angle, μ_0 the magnetic permeability in free space and l_0 corresponds to the effective cross section of the coupling region (Akasofu, 1980).

The IMF direction has a strong influence on the magnetotail structure. During a southward orientation of the IMF the tail is often in a dynamic state with frequent outbreaks of so called magnetic substorms. They involve a strong expansion of the entire magnetotail followed by a collapse and are connected to strong geomagnetic and auroral activity near the Earth. During northward IMF the magnetotail is in steady state, its length is inversely proportional to the strength of the IMF B_z component (Gombosi et al., 1998). The IMF B_y component changes the shape of the magnetotail. It causes a twisting of the entire plasma sheet along the x-axis (Tsyganenko, 1998) and the magnetic field lines are strongly bent in dawn-dusk direction. The field line bending corresponds to an extra B_y field that occurs in the tail and has the same direction as IMF B_y (Lui, 1986).

2.3 Magnetic reconnection

The behavior of a plasma in the presence of a magnetic field changes radically with the degree of conductivity. It can be shown that for plasmas with an infinite conductivity, no magnetic diffusion through the plasma appears. This means, the magnetic field lines are tied to the fluid and move with the plasma. One speaks of frozen-in flux of the magnetic field. For a plasma with a finite conductivity magnetic field and plasma are partially decoupled and the magnetic field can diffuse through the plasma. The thin and highly ionized solar wind belongs to the high-conductivity plasmas. Hence, the IMF is attached to the flowing solar wind plasma.

Near the magnetopause the principle of frozen-in flux breaks down. Magnetic diffusion makes it possible for the IMF, transported by the solar wind toward the dayside magnetopause, to merge with the magnetospheric field. This process is also referred to as reconnection. The efficiency and the location of the reconnection process are strongly dependent on the direction of the IMF. As illustrated in Figure 2.3a, IMF and the magnetosphere field are anti-parallel at the dayside magnetopause only when the IMF has a negative B_z component, i.e., a southward pointing IMF component. Field lines originally with both ends attached

at the Earth, (closed field lines) merge with solar wind field lines. They become open, i.e., only one end is attached to the Earth, the other end is attached to an IMF field line. Due to the principle of frozen-in flux in the undisturbed solar wind, the open end of the field line is carried in tailward direction. In the tail, northern and southern open field lines reconnect along a second reconnection line creating sunward moving closed field lines and tailwardly moving IMF field lines. The open tail field lines are located in the lobes while the closed field lines fill the plasma sheet.

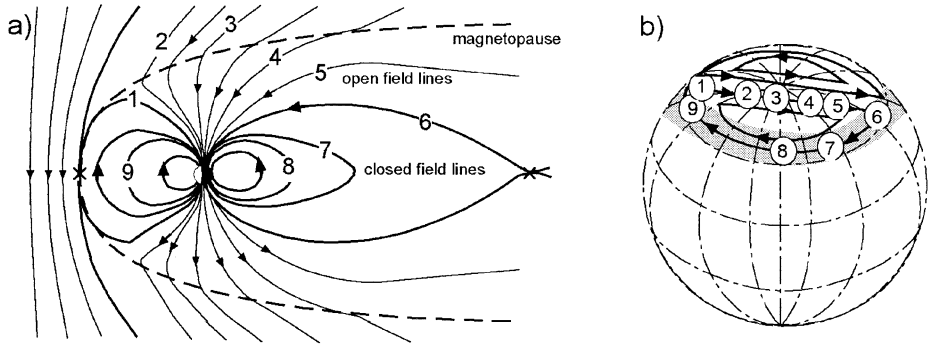

Figure 2.3: Reconnection and flux tube convection for southward IMF a) in the magnetosphere and b) in the ionosphere (Dungey, 1961).

During northward IMF B_z, the interplanetary magnetic field and the magnetosphere field have at the dayside magnetopause the same direction. This makes dayside reconnection impossible. It has been suggested that during northward IMF the magnetosphere is completely closed to the solar wind and the only interaction would arise due to viscous interaction at its boundary layers (Axford and Hines, 1961). However, reconnection can occur even during northward IMF, but at the high-latitude near-Earth tail lobes. Several field line circulations are possible. The most commonly accepted scenario is depicted in Figure 2.4a. Field lines having been opened during a preceding period of southward IMF reconnect with IMF lines at the high-latitudes lobes to create new, open field lines at the dayside and modified IMF field lines at the nightside, moving in a tailward direction. Computer simulations indicate that northward IMF, not preceded by southward IMF would lead to a completely closed magnetosphere (e.g., Gombosi et al., 1998). The northward and southward state of the magnetosphere are the most extreme cases, leading to a closed or open magnetosphere, respectively. In reality the IMF is never completely steady during many hours, as necessary for reaching these extreme states. The influence of the other IMF components and IMF fluctuations lead to a deviation from these simple models.

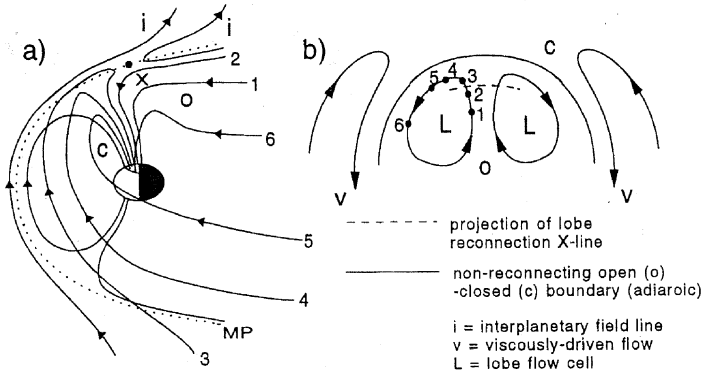

Figure 2.4: Reconnection and flux tube convection for northward IMF a) in the magnetosphere and b) in the ionosphere (Lockwood, 1987).

There have been different views on where on the magnetopause reconnection occurs. In the component merging theory, reconnection occurs where the IMF first encounters the magnetosphere (Sonnerup, 1974), in the anti-parallel merging theory (Crooker, 1979), it appears where the fields are completely anti-parallel to each other. The case for pure IMF B_y illustrates clearly that the two theories predict two different merging sites. In the component merging theory the field lines merge along a tilted line through the x-axis. In the anti-parallel merging theory merging occurs in two separated regions in the northern dusk (dawn) and southern dawn (dusk) lobes for duskward (dawnward) IMF B_y. Numerical modeling results indicate that anti-parallel merging is the most probable one. But there are observations in favor of the component merging theory (Russel et al., 1985). In reality, reconnection occurs not constantly at one single line. Observations indicate that reconnection occurs in form of periodic flux transfer events at the magnetopause (Kim et al., 2002).

2.4 The ionosphere

The ionosphere is the transition layer between the neutral atmosphere and the fully ionized magnetosphere and thus only partially ionized. The main source of ionization is the solar UV radiation, but also energetic particle precipitation from the magnetosphere into the atmosphere contributes significantly to the ionization. The composition and electron density of the ionosphere varies with local time, latitude and altitude. At daytime, the ionization due to UV radiation dominates, the magnetospheric particle precipitation is most intense in the regions of the auroral oval. The maximum electron density is at about 250 km

above the Earth because the neutral particle density increases towards lower altitudes, but the ionization decreases due to atmospheric absorption of the UV radiation. A full ionization of the ionosphere is prevented by the frequent recombination of ions and electrons.

Due to the low ionization and the high density of the ionospheric plasma the orbits of charged particles are disturbed by frequent collisions with neutrals such that they react in a different way to electromagnetic forces than the magnetospheric plasma. The conductivity becomes non-isotropic, hence the currents and plasma motions are more complicated than in the magnetosphere. The peak values of the conductivities in the plane perpendicular to the magnetic field (Pedersen and Hall currents) occur at around 100-130 km altitude.

The low-latitude part of the ionosphere belongs to the so called plasmasphere in which the plasma corotates with the Earth. In the high-altitude part of the polar ionosphere, the plasma motions are determined by the large-scale circulation of the magnetospheric flux tubes. The collision frequency at around 1000 km is decreased to such low values that the plasma becomes tied to the magnetic field. The circulation performed by the ionospheric footprints of magnetic field lines corresponds to a plasma convection in the same direction. As illustrated in Figure 2.3b, a two-cell convection pattern emerges in the southward IMF case. The tailward motion of the newly opened field lines corresponds to an anti-sunward plasma flow at the highest latitudes. The earthward motion at the dawn and dusk magnetotail flanks leads in the ionosphere to a sunward flow at lower latitudes. For northward IMF the ionospheric convection pattern is reversed (see Figure 2.4b). A sunward flow appears on highest latitudes. At lower latitudes the plasma drift returns into anti-sunward direction. Equatorward of these cells two additional cells occur that are probably caused by viscous interaction at the magnetosphere boundary. In general the convection pattern is much more complicated than sketched here. The other IMF components and temporal changes have to be taken into account. Size and form of the cells are strongly dependent on the IMF B_y direction, during northward IMF there appear more than 2 cells but the number of cells can vary.

2.5 The aurora

The magnetosphere acts in some sense like a huge dynamo, driven by the solar wind. As electrons are free to move parallel to the magnetic field in a collisionless plasma (as long as the gradients of the magnetic field are small) currents having their source region in the magnetotail flow along the magnetic field lines into the high-latitude ionosphere. Due to the finite resistivity of the ionospheric plasma, the ionosphere acts as a load in the solar wind-magnetosphere coupling system of which the aurora is the visible signature.

The aurora occurs at around 100 km altitude above the Earth. The light emissions of the aurora are produced when neutral atoms or molecules are ex-

cited by collisions with precipitating electrons. Dependent on which type of particle and to which energy level it is excited, photons of a certain energy and wavelength are emitted when the particle returns to a lower energy state. The most commonly visible colors of the auroral are green (emitted by Oxygen atoms) and red (emitted by molecular Nitrogen or high-altitude Oxygen atoms).

The currents producing the aurora flow in thin sheets along the magnetic field lines from the magnetosphere down into the ionosphere and parallel to it back into the magnetosphere again. The currents reach the ionosphere in two concentric rings. The statistical field-aligned current pattern as determined by Iijima and Potemra (1976) is shown in Figure 2.5. The poleward and equatorward rings are denoted as Region 1 and Region 2, respectively. The Region 2 currents map to the ring current in the near-Earth magnetosphere, the Region 1 current to the tail plasma sheet. As can be seen from Figure 2.5, the upward current sheet is located on the dawn side of the downward current sheet.

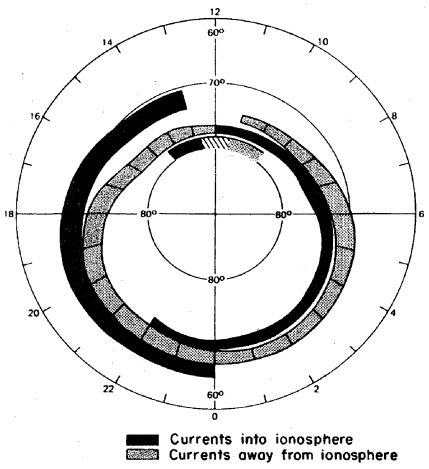

Figure 2.5: Statistical distribution of field-aligned currents into and out of the ionosphere during low geomagnetic activity (Iijima and Potemra, 1976).

The auroral emissions in the main auroral oval are diffuse and often quite weak. They extend over a wide latitude range. The diffuse aurora is produced by precipitating particles of about 1 keV that originate in the tail plasma sheet. Very bright and active auroral displays are often seen near the poleward boundary and on the dusk side of the auroral oval and are called discrete aurorae. Discrete auroral arcs are caused by highly energetic electrons with energies of of several keV having their source region in the plasma sheet boundary layer. These electrons gain their energy from an acceleration process that involves U-shaped field-aligned electric double layers, a process which is not yet fully

understood.

The luminosity and size of the auroral oval depends strongly on the direction of the IMF. During a southward orientation of the IMF, the auroral oval is usually very bright and active and substorms occur periodically (a substorm causes a sudden brightening and a large expansion of the nightside auroral oval until it recovers to its original state). For persistent northward IMF the auroral oval is strongly contracted, the auroral emissions are weak and auroral arcs occur often poleward of the auroral oval inside the so called polar cap. Small-scale sun-aligned arcs are nearly constantly observed inside the polar cap during northward IMF, large-scale polar arcs occur less frequently. The motion of polar auroral arcs is governed by the dawn-dusk component of the IMF (Figure 2.6). Arcs near the side of the auroral oval which lies in the direction of the IMF B_y component move slightly poleward while polar arcs in the middle of the polar cap or on the other oval side move into the direction of IMF B_y (Valladares et al., 1994). Observations in recent years indicate that large-scale moving polar arcs may be triggered by IMF B_y or IMF B_z sign changes (Cumnock et al., 2002, Chang et al., 1998).

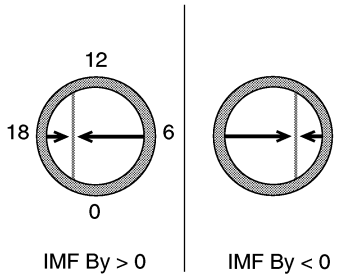

Figure 2.6: Statistical results of IMF B_y dependent motion of small-scale sun-aligned arcs by Valladares et al., (1994).

The boundary of the auroral oval is assumed to coincide with the boundary between open and closed field lines. The plasma sheet origin of particles causing the aurora indicates that the entire region of main auroral oval lies inside the region of closed field lines. The polar cap is defined as the region of open field lines and lies poleward of the auroral oval. Auroral arcs occurring inside the polar cap may have different source regions depending on their size. Although there are many indications small-scale sun-aligned arcs lie on open field lines, their source region is still unclear (Bonnell et al., 1998). Large-scale polar arcs have been found to have similar particle characteristics as the auroral oval, but with slightly lower energies. It is generally agreed on that large-scale arcs map to the plasma sheet and thus are located on closed field lines (e.g., Frank and Craven, 1988).

Chapter 3

Basic space plasma physics

3.1 Definition of plasma

A plasma is generally defined as a gas of charged particles which has an equal amount of negative and positive charges and reacts to electromagnetic forces in a collective way. To obtain quasi-neutrality any externally applied potential must be shielded within a distance that is essentially shorter than the scale length on which the system is defined as a plasma. $\lambda_D = \sqrt{(\epsilon_0 k_B T_e / n_e q^2)}$ defines the radius of the shielding, where ϵ_0 is the permittivity of free space, k_B the Boltzmann constant, q the elementary charge, T_e and n_e the electron temperature and density, respectively. A high electron density and low thermal motions allow a shielding within a short distance. Another requirement for a gas to behave like plasma is that the collision frequency with neutrals is low enough that the motion of the charged particles is dominated by electromagnetic forces.

3.2 Single particle description

The paths of neutral gas particles are determined by random collisions with other particles. Their collective motions are described within the classic fluid mechanical theory. In plasmas the interaction between charged particles and external electromagnetic fields have to be taken into account as well.

In the single particle approach the influence of externally applied electromagnetic forces on a single particle is studied. This description is strictly speaking only valid for plasmas where particle-particle interactions and electromagnetic fields induced by particle motions themselves are small compared to externally applied fields. However, the single particle description helps understanding the behavior of plasma particles in the presence of electromagnetic fields.

The velocity of a single particle moving in an electromagnetic or other force field can be derived from the Lorentz force ($md\mathbf{v}/dt = q(\mathbf{v} \times \mathbf{B}) + \mathbf{F}$). In a

homogeneous magnetic field a charged particle gyrates around the magnetic field line with the gyrofrequency $\omega = qB/m$. If any external force is applied in the presence of a magnetic field the gyrating particle drifts with the velocity v_D perpendicular to the applied force and to the magnetic field ($\mathbf{v_D} = \mathbf{F} \times \mathbf{B}/qB^2$). In the presence of an electric field all particles drift in the same direction, in a curved magnetic field or a gravitation field, differently charged particles drift in opposite directions, thus a net current occurs (for example, the ring current is caused by a B-field gradient drift and a curvature drift, the earthward plasma drift along the plasma sheet is a $\mathbf{E} \times \mathbf{B}$ drift). The large-scale currents appearing in geophysical plasmas cannot be calculated from single particle motions only. The particle gyromotions produce an additional current if there is a population gradient. Although the size of the current cannot be calculated by single particle motions, the direction of the currents is given correctly.

For a complete description of the plasmas properties it is necessary to take all particles into account. However, even with the fastest computers it is not possible to calculate the motion of each single particle in the presence of self-generated and externally applied electromagnetic fields and taking the interaction with other particles into account. The most fundamental approximation is given in the kinetic plasma theory where each particle species is described by a statistical distribution function which depends on time, space and velocity. In many cases, though, it is sufficient to know the macroscopic properties of the plasma where the physical quantities are defined as the average value over the entire particle distribution within one volume element. This is done in the magnetohydrodynamic description where the plasma is treated like a fluid.

3.3 Magnetohydrodynamic description

In the single-fluid magnetohydrodynamic (MHD) approach the entire plasma is treated as one fluid. The plasma is assumed to consist of only two particle species (electrons and ions) that form two sets of fluid equations which are then reduced to single-fluid equations. Density, current and velocity of the plasma fluid are defined as $\rho = n_i m_i + n_e m_e$, $\mathbf{j} = q n_i \mathbf{v_i} - q n_e \mathbf{v_e}$, and $\mathbf{v} = (n_i m_i \mathbf{v_i} + n_e m_e \mathbf{v_e})/\rho$ where i and e describe the quantities for ions and electrons, respectively.

In a plasma quasi-neutrality always holds in sufficiently large scales $L >> \lambda_D$ such that an equal amount of negatively and positively charged particles $n = n_i = n_e$ can be assumed.

Most geophysical plasmas can be considered to behave like ideal gas in an adiabatic state. An ideal gas is in thermal equilibrium. It is isotropic and uniquely defined by the temperature, thus the pressure becomes a scalar $p = nkT$. In the adiabatic state all changes in the system take place without heat exchange.

For the thin and highly ionized magnetospheric and solar wind plasmas it can be assumed that the plasma is collisionless. The plasma conductivity can be

considered to be infinitely large. The electric field reduces to zero in the frame moving with the fluid. However, in an arbitrary reference frame a convection electric field appears due to the Lorentz transformation. (The non-relativistic Lorentz transformations show that the electric field changes with the change of the reference frame, the magnetic field not: $\mathbf{E}' = \mathbf{E} + \mathbf{v} \times \mathbf{B}$ and $\mathbf{B}' = \mathbf{B}$, where $\mathbf{E}$ and $\mathbf{B}$ detect the fields in the reference frame at rest, $\mathbf{E}'$ and $\mathbf{B}'$ are the values of the fields in the reference frame moving with the velocity $\mathbf{v}$. The part of the electric field which is induced by the motion of a magnetized plasma $\mathbf{v} \times \mathbf{B}$ is called the convection electric field).

$$\mathbf{E} + \mathbf{v} \times \mathbf{B} = 0 \tag{3.1}$$

This equation corresponds to Ohm's law $\mathbf{j} = \sigma_0(\mathbf{E} + \mathbf{v} \times \mathbf{B})$ with an infinite conductivity.

In a fluid mass, momentum and energy have to be conserved. From this principle the basic MHD equations can be derived. The continuity equation describes the conservation of mass. The increase or decrease of mass inside a volume corresponds to the flux of mass which enters or leaves a volume through its surface.

$$\frac{\partial \rho}{\partial t} + \nabla \cdot (\rho \mathbf{v}) = 0 \tag{3.2}$$

The equation of motion gives the conservation of momentum. It relates the temporal change of the velocity to the forces acting on the fluid. In a collisionless geophysical plasma, the gravitational and collisional forces vanish. In case the pressure is not uniform a force arises which has to be included in the equation of motion. The force drives the fluid in the direction opposite to the pressure gradient in a try to remove the non-uniformity. As the charged particles of a plasma react on electromagnetic forces the Lorentz force $q(\mathbf{E} + \mathbf{v} \times \mathbf{B})$ has to be added. The $\mathbf{v} \times \mathbf{B}$ term means that an induced electric field affects the particles to reduce this field again. In the equation the force term associated with the electric field $\Sigma_{s=i,e}(n_s q_s \mathbf{E})$ disappears for a quasi-neutral plasma.

$$\rho \frac{d\mathbf{v}}{dt} = -\nabla p + \mathbf{j} \times \mathbf{B} \tag{3.3}$$

The equation of state describes the conservation of energy in the system. For an adiabatic fluid the adiabatic equation of state has to be used which says that the heat flux p/ρ^γ must be conserved. ($\gamma = C_p/C_v \sim 5/3$ is the adiabatic constant)

$$\frac{d}{dt}(p\rho^{-\gamma}) = 0 \tag{3.4}$$

In plasmas the Maxwell's equations have to be added. They describe the interaction between charges and electromagnetic forces.

$$\nabla \times \mathbf{E} = -\frac{\partial \mathbf{B}}{\partial t} \quad \text{(Faraday's law)} \tag{3.5}$$

$$\nabla \times \mathbf{B} = \mu_0 \mathbf{j} \quad \text{(Ampère's law)} \tag{3.6}$$

$$\nabla \cdot \mathbf{B} = 0 \tag{3.7}$$

The last Maxwell equation $\nabla \cdot \mathbf{E} = \rho_q/\epsilon_0$, also called Poisson's equation, is dropped here because the charge density $\rho_q = q(n_i - n_e)$ becomes zero when quasi-neutrality is assumed. In Ampères law the displacement current $\partial \mathbf{E}/\partial t$ can be neglected because only long time variations are of interest in the MHD approach. This means electric fields change in an MHD plasma only when $\partial \mathbf{B}/\partial t$ is nonzero or the reference frame is changed.

Equations (3.1) to (3.6) can be reduced to four conservative equations of the form $\partial \rho_a/\partial t = -\nabla \cdot \mathbf{F_a}$ where ρ_a is the density of a physical quantity and $\mathbf{F_a}$ is its flux.

$$\frac{\partial \rho}{\partial t} = -\nabla \cdot (\rho \mathbf{v}) \tag{3.8}$$

$$\frac{\partial \mathbf{v}}{\partial t} = -\frac{\nabla p}{\rho} - (\mathbf{v} \cdot \nabla)\mathbf{v} - \frac{B^2}{2\rho\mu_0} + \frac{(\mathbf{B} \cdot \nabla)\mathbf{B}}{\rho\mu_0} \tag{3.9}$$

$$\frac{\partial}{\partial t}\left(\frac{p}{\gamma - 1} + \frac{\rho v^2}{2} + \frac{B^2}{2\mu_0}\right) = -\nabla \cdot \left(\frac{\gamma p}{\gamma - 1}\mathbf{v} + \frac{\rho v^2}{2}\mathbf{v} + \frac{\mathbf{B} \times (\mathbf{v} \times \mathbf{B})}{\mu_0}\right) \tag{3.10}$$

$$\frac{\partial \mathbf{B}}{\partial t} = \nabla \times (\mathbf{v} \times \mathbf{B}) \tag{3.11}$$

The number of variables has been reduced to $\rho, p, \mathbf{v}$ and $\mathbf{B}$ by using $\mathbf{E} = -\mathbf{v} \times \mathbf{B}$ and $\mathbf{j} = \nabla \times \mathbf{B}/\mu_0$. To derive the energy equation (3.10), the equation of state has been rewritten (using the continuity equation) to $\rho dp/dt = -\gamma p \nabla \cdot \mathbf{v}$. Combining this equation with the equation of motion yields (3.10). The expression in the bracket of the left hand side represents the total energy density, consisting of the thermal, the kinetic and the magnetic energy densities. The right hand side describes how these energies flow, the pointing vector $\mathbf{E} \times \mathbf{B}/\mu_0$ describes the transport of the electromagnetic energy.

Equations (3.8) to (3.11) are the complete set of MHD equations in conservative form. It describes all properties of an ideal MHD fluid when taking into account that the magnetic field has to stay divergence free (eq. 3.7).

3.4 Ionospheric electrodynamics

The ionosphere, being the layer between the fully ionized, collisionless magnetosphere and the atmospheric neutral gas layer is only partially ionized. Due to

its high particle density the ionospheric plasma belongs to the collisional plasmas. Most collisions occur between charged particles and neutrals. They are described by the collision frequency ν_{sn} of neutrals with electrons and ions for $s = e$ and $s = i$, respectively.

As the ionosphere is not an ideal conductor, ideal MHD cannot be applied. Fortunately, other approximations can be made to simplifying the conservation equations: The ionospheric plasma can be considered to be in steady state because the response of the plasma to changing forces occurs very quickly. Another assumption that can be safely made is to regard the ionospheric plasma as homogeneous, i.e. the pressure gradients in the plasma are negligible. In the ionosphere induced electric fields can be neglected because the magnetic field variations near the Earth are generally small compared to the entire field strength. Faraday's law reduces to $\nabla \times \mathbf{E} = 0$ and the electric field becomes a potential field.

$$\mathbf{E} = -\nabla\phi \tag{3.12}$$

As quasi-neutrality holds in all plasmas, the charge density $\rho = n_i q - n_e q$ becomes zero. Consequently, the continuity equation for charges $\Sigma_{s=i,e}(\partial\rho_s/\partial t = -\nabla\cdot(\rho_s \mathbf{v_s}))$ reduces to zero and the current $\mathbf{j} = qn(\mathbf{v_i} - \mathbf{v_e})$ becomes divergence free

$$\nabla \cdot \mathbf{j} = 0 \tag{3.13}$$

With these approximations the equation of motion can be simplified considerably. Only a collisional term has to be added. It describes the momentum which is lost through collisions. The neutrals are considered to be at rest such that only the charged particles have a velocity $\mathbf{v_s}$. For the steady state ionosphere, the left hand side disappears ($m_s d\mathbf{v_s}/dt = 0$). The equation of motion can be written for each particle species $s = i, e$ as

$$0 = q_s(\mathbf{E} + \mathbf{v_s} \times \mathbf{B}) - m_s \nu_{sn} \mathbf{v_s} \tag{3.14}$$

From this equation using $\mathbf{j} = qn(\mathbf{v_i} - \mathbf{v_e})$ Ohm's law can derived. In the ionosphere the conductivity becomes non-isotropic and can be expressed as a tensor $\hat{\sigma}$.

$$\mathbf{j} = \hat{\sigma}\mathbf{E} \tag{3.15}$$

This equation is easier to interpret when splitting the current into a component parallel and a component orthogonal to the magnetic field:

$$\mathbf{j} = \mathbf{j}_{||} + \mathbf{j}_{\perp} = \sigma_0 \mathbf{E}_{||} + \sigma_P \mathbf{E}_{\perp} - \sigma_H \frac{\mathbf{E} \times \mathbf{B}}{B} \tag{3.16}$$

where $||$ and $\perp$ refer to the directions parallel and perpendicular to the magnetic field. The Pedersen, Hall and parallel conductivities are defined as

$$\begin{aligned}
\sigma_P &= \sum_{s=i,e} \left(\frac{nq^2}{m_s}\right) \frac{\nu_{sn}}{\nu_{sn}^2 + \omega_{sn}^2} \\
\sigma_H &= \sum_{s=i,e} -\left(\frac{nq^2}{m_s}\right) \frac{\omega_s}{\nu_{sn}^2 + \omega_s^2} \\
\sigma_0 &= \sum_{s=i,e} \left(\frac{nq^2}{m_s}\right) \frac{1}{\nu_{sn}}
\end{aligned}$$

ν_{sn} is the collision frequency and $\omega_s = q_s B/m_s$ the gyrofrequency of the electrons and ions for $s = e$ and $s = i$, respectively. The expression for the parallel conductivity shows that parallel to the magnetic field, the particle motions are only influenced by collisions.

The Pedersen and Hall conductivities are connected to currents with the same name flowing parallel and orthogonal to the electric field. These currents flow mainly in the so called dynamo layer at 50 to 150 km height where the Hall and Pedersen conductivities reach their maximum (the conductivities are height-dependent because they both include the height-dependent collision frequencies). The ion motion contributes to a large part to the Pedersen current which flows parallel to the electric field. The Hall current flows perpendicular to $\mathbf{E}$ and $\mathbf{B}$ and is caused mainly by $\mathbf{E} \times \mathbf{B}$ drifting electrons. The different behavior of ions and electrons depends on the different ratios between gyro- and collision frequencies for each species. In the dynamo layer, electrons have a much higher gyrofrequency than collision frequency such that their motions are dominated by the electromagnetic forces. The much heavier ions have a lower gyrofrequency. They collide with neutral particles much before they have done even a part of their gyration which allows them to partly move in the direction of the electric field.

In magnetospheric and solar wind plasma the conductivity is extremely high, which means the electric field parallel to the magnetic field vanishes. In these plasmas the large-scale electric field in a plane perpendicular to the magnetic field maps along the field lines. Even at ionospheric heights, the parallel electric field is much smaller than the perpendicular electric field. Hence, it is possible to integrate the physical quantities along the magnetic field lines. The Pedersen and Hall conductances are defined as $\Sigma_P = \int \sigma_P dz$ and $\Sigma_H = \int \sigma_H dz$ and the height-integrated perpendicular currents is $\mathbf{J}_{\perp} = \int \mathbf{j}_{\perp} dz$ where z is the

direction along the magnetic field line (which is in the high-latitude ionosphere approximately the z-direction). The height-integrated Ohm's law becomes

$$\mathbf{J}_\perp = \Sigma_P \mathbf{E}_\perp - \Sigma_H \frac{\mathbf{E} \times \mathbf{B}}{B} \tag{3.17}$$

Due to zero divergence of the currents $\nabla \cdot \mathbf{J}_{||} + \nabla \cdot \mathbf{J}_\perp = 0$ the field-aligned current can be expressed as

$$\mathbf{j}_{||} = -\nabla \cdot \mathbf{J}_\perp \tag{3.18}$$

Replacing $\mathbf{J}_\perp$ by equation (3.17) and using $\mathbf{E} = -\nabla\phi$ an electrostatic equation is derived that correlates the field-aligned currents flowing between the magnetosphere and the ionosphere with the ionospheric potential distribution.

$$j_{||} = \Sigma_P \nabla^2 \phi + \nabla\Sigma_P \cdot \nabla\phi - \nabla\Sigma_H \cdot \frac{\nabla\phi \times \mathbf{B}}{B} \tag{3.19}$$

For the calculation of the conductances, it is necessary to know the electron density $n(z)$ that depends strongly on altitude, latitude and daytime. In a rough approximation one can express the change of the electron density as

$$\frac{dn_e}{dt} = q_\nu - \alpha n_e^2 \tag{3.20}$$

where q_ν gives the production rate due to UV radiation and electron precipitation and α the rate at which the charged particles recombine. (the calculation of q and α is rather difficult as both depend on many different parameters). The density can be calculated in steady state by equating the production due to UV radiation and electron precipitation and recombination rates.

Chapter 4

Magnetosphere models

While much of our knowledge about the ionosphere is gained by a large amount of observations (multiple ground-based instruments, rockets, spacecrafts) it is much more difficult to get the same amount of information from the magnetosphere and especially the magnetotail. Due to the large extent of the magnetotail with only a few satellites within it simultaneously, only snapshots of the tail situation in localized regions are taken. It is often difficult to determine in which tail region the measurements are taken as it takes a long time for a satellite to cross the magnetotail and IMF conditions may change rapidly. The average structure of the magnetotail for different IMF directions can be examined by collecting a large amount of data and treating it in a statistical way (e.g., Owen et al. 1995, Kaymaz et al., 1994). However, when the interest lies in understanding the magnetospheric reaction on dynamic changes in the solar wind, it is not possible to gain a global picture based exclusively on satellite data. Several tens of satellites would need to fly simultaneously in the magnetotail to reach this goal.

It has proven extremely difficult to recreate space plasma conditions in laboratories. To date, some laboratories succeeded to recreate reconnection near a magnetized body in a plasma fluid but those results are only a very rough approximation of reality, of which only the most fundamental processes can be studied (Yamada, 1999).

To explore the dynamic evolution of the magnetosphere, numerical modeling has become an important tool. Due to the enormous capacity of modern computers it is possible to run 3D-simulations of the entire magnetosphere and solar wind environment and thus gain a global picture of the coupling between magnetosphere and solar wind.

4.1 Vacuum superposition model

A qualitative understanding of how the magnetic field configuration in the near-Earth space environment depends on the IMF direction, can be gained by studying simple vacuum superposition models. In such models a uniform IMF field is added on a dipole field where the plasma impact on the magnetic field configuration is completely neglected by assuming vacuum (Cowley, 1973). As the magnetopause shape is mainly created by the impact of the solar wind flow with the geomagnetic field, it can not be recreated in vacuum superposition models. Also the tailward stretching of the magnetic field does not occur in such models. However, these models describes the main properties of the magnetic field topology in the plane perpendicular to the solar wind flow fairly well.

Figure 4.1 shows the resulting field line topology for (from left to right) southward, duskward and northward IMF. The main features expected for the different IMF directions occur. For southward IMF, the IMF and dipole field lines reconnect along an equatorial merging line. For duskward IMF the reconnection is displaced toward the northern dusk and southern dawn lobes. In the northward IMF case the IMF is separated from the dipole field by a closed surface except at the north and south poles, indicating a minimum reconnection rate.

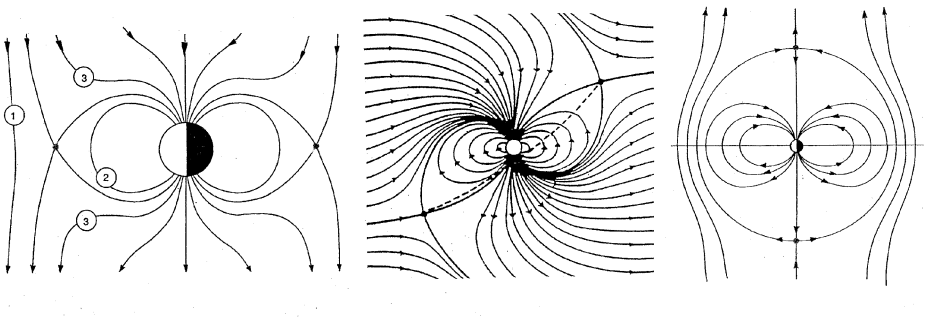

Figure 4.1: Vacuum superposition for a) southward b) duskward and c) northward IMF (Parks, 1991; Kaymaz, 1993). The figures show the yz-plane at $x = 0$.

An extended superposition model has been developed by Crooker et al. (1990) which takes the partial shielding of the magnetic fields along the magnetopause into account. In addition to the superposition of a uniform IMF on a dipole field, the model allows via currents along a spheric magnetopause partial shielding of both the IMF penetration into and the dipole field leakage out of the magnetosphere. This model shows a very good agreement in the yz-plane with mid-tail observations (Kaymaz and Siscoe, 1998) and MHD simulation results. To demonstrate the similarity between the Crooker et al. (1990) model and MHD models, Figure 4.2 shows the open (grey) and closed (white) field line

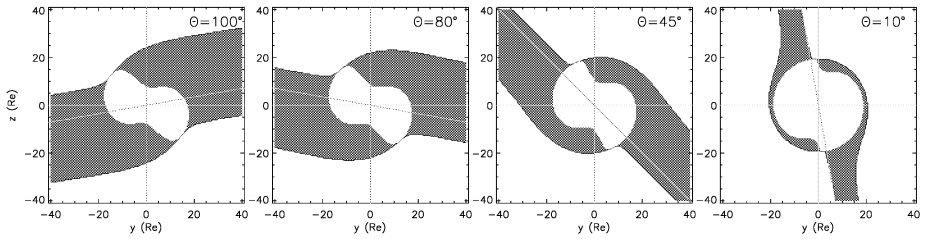

Figure 4.2: The regions of open and closed field lines in the extended vacuum superposition model by Crooker et al. (1990). The plots show for different IMF clock angles the regions of open (grey) and closed (white region enclosed by the grey region) field lines for a cross section at $x = -5\mathrm{R_E}$ of a spheric magnetosphere with a radius of $R = 20\mathrm{R_E}$ for equal IMF penetration and dipole leakage.

regions of the Crooker et al. (1990) model for the different IMF clock angles studied in the MHD simulations of Paper 4 (compare Fig. 4.2 with Paper 4, second row of Figure 1).

As can be seen from Figure 4.2, a thickening of the twisted closed field line region and a thinning of the open field line region for small clock angles appear. The open field lines are oriented along the IMF direction with a small, anticlockwise (looking tailward) displacement from it. The closed field line region in the Crooker et al. (1990) model is thicker than expected in the magnetotail because of the missing tailward field line stretching. From the Crooker et al. (1990) vacuum superposition model the clock angle dependent topological changes can be easily understood: The draping of the IMF field lines around the tail is caused by the shielding of the IMF from the tail. The deviation from an entirely symmetric draping pattern occurs due to the leakage of the dipole field into space.

4.2 Empiric magnetosphere model

Due to the large data sets from spacecraft measurements in the near Earth environment over many years, several empiric models have been developed that reproduce the magnetospheric magnetic field as realistically as possible. Although they do not allow insight into mechanisms that create the magnetic field topology, they provide to date the most realistic magnetosphere field for average steady state conditions. This makes them for certain tasks superior to fully developed MHD models. Empiric magnetic field models are a good tool to trace field lines or particles between different regions of the magnetosphere, to fit observations into the global magnetospheric structure or to study the temporal change of the magnetospheric topology using a stepwise change of the model field (Jordan, 1994).

The Tsyganenko 1989 model (T89) is one of the most widespread semi-empiric magnetic field models of the magnetosphere (Tsyganenko, 1989). It sums the contributions to the magnetospheric field from the main current systems and the Earth dipole field. It can be chosen if the geomagnetic field is represented by a pure dipole field or by the more accurate empiric IGRF model. The ring current, the cross tail current and the magnetopause tail current are all expressed by analytic functions that are parameterized by free parameters. These have been fit to a large dataset of IMP and HEOS spacecraft measurements. A smooth transition is done from the ring current to the cross tail current. The parts of the tail current system which flow along the magnetopause are simulated with planar current sheets at $\pm 30 R_E$. In this model the magnetopause is not explicitly specified, the standoff distance, magnetopause current and shielding of the solar wind are empiric fits to the data. The model is sensitive to the Earth dipole tilt and the disturbance level of the inner-magnetospheric field, given by the K_p index. These two quantities are needed as input for the model.

With this method a field distribution is achieved that corresponds to the standard magnetotail fairly well. However, there are some limitations of the model (Fairfield, 1991; Stern and Tsyganenko, 1992). The T89 model was primarily developed to represent the magnetotail between 4 and 70 R_e tailward from the Earth such that in the region inside 4 R_e and the dayside region are less well represented. For low K_p values the B_z component gets too small or even negative in the near-Earth tail center and at the flanks.

In Paper 1 and Paper 2 the T89 model is modified to examine the effect of topological changes inside the magnetotail on the field line mapping between the tail and the ionosphere. In both papers, the pure dipole field is chosen and dipole tilt and K_p index are set to zero to represent the simplest standard magnetosphere during quiet times. As the magnetopause is not explicitly given, there exist no open field lines, all field lines closed at some point far downtail. As an artificial polar cap boundary, the high-latitude boundary of those closed field lines can be chosen, that have their origin in the tail current sheet earthward of 70 R_E.

4.3 Magnetohydrodynamic model

The GUMICS-4 code is a global magnetohydrodynamic model of the magnetosphere. It has been developed by Pekka Janhunen at FMI, Finland (Janhunen, 1996). A description of its newest version has recently been published by Palmroth (2003). In Paper 4 this MHD model is used to examine the validity of the results from Paper 1 and Paper 2 in the framework of MHD.

The simulation box used in the GUMICS-4 model extends from 32 R_E sunward to 224 R_E tailward of the Earth. In the yz-plane, the box has a dimension of 128×128 R_E. The shell at a distance of 3.7 R_E from the Earth is defined as

the boundary between the magnetosphere and the ionosphere. Magnetic field lines map from this shell to the high-latitude ionosphere above 60 degrees latitude. In the model the high-latitude ionosphere is assumed to be planar and is discretized into a 3D grid with 20 nonuniform levels of height. The MHD model needs as input parameters solar wind speed, solar wind pressure, IMF B_y, IMF B_z and dipole tilt. All runs start with a magnetic dipole field in a uniform low-density plasma.

The overall structure of the MHD model is sketched in Figure 4.3. The solar wind and the magnetosphere regions are treated with the ideal MHD equations (3.7) to (3.11). The ionosphere is described with the electrostatic equation (3.19). The shell around 3.7 R_E from the Earth is set as the boundary between the magnetosphere and the ionosphere. The boundary conditions at this shell are updated with a new potential distribution every 4 seconds by solving the ionospheric equations. To do this, the magnetospheric field-aligned currents are calculated along the boundary and are mapped down to the ionosphere where the corresponding potential is calculated and mapped back to the boundary. For the calculation of the conductances in equation (3.19), the height-dependent ionospheric electron density is needed. It is solved from the recombination and ionization production rates at different altitudes about the Earth (eq. 3.20). The ionization is assumed to be caused by solar UV radiation and electron precipitation. The UV radiation is predefined in the model, the electron precipitation rate depends on the magnetospheric source plasma density and temperature which are obtained from the MHD variables (Janhunen and Huuskonen, 1993).

In the code all physical quantities are calculated with time steps of less than a second for a mesh containing about 130000 grid cells. The time steps and the grid size are not constant throughout the simulation box. The code uses subcycles in areas where the time step is refined and a semi-automatic grid-refinement is used which depends on the gradients of the physical quantities. The mesh size can vary between 0.1 and 8 R_E. To save some computation time, the threshold for the grid refinement depends on location, that is, smaller gradients are required to refine the grid in the near Earth region than, for example, in the distant tail. The time steps are smaller in the near-Earth region and larger in the distant tail. They obey the Courant-Friedrichs-Lewy condition which states that the time step must everywhere be smaller than the travel time at which information is transferred.

The MHD equations (3.8) to (3.11) belong to the type of nonlinear partial differential equations and are solved by using the finite volume method as discretization method. Since the finite volume method is based on the integral formulation of the conservation laws, it guarantees the discrete conservation property in arbitrary grids. The nonlinear and time-dependent problem with discontinuous data constitutes a so called Riemann problem, here solved by a Roe solver. Despite a grid refinement at sharp gradients, the numerical solution leads sometimes to unphysical values of the magnetic field and the pressure. To

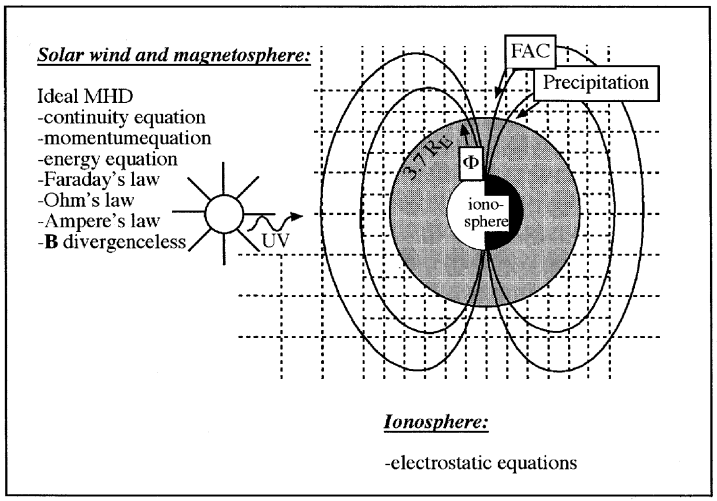

Figure 4.3: The overall structure of the GUMICS model (Palmroth, 2003).

keep the magnetic field divergence free, the method of elliptic cleaning is used. To reduce the numerical errors leading to negative pressure values, the equation system is modified by decomposing the magnetic field into a background (dipolar) field and an external field. The pressure can be calculated using only the external part of the magnetic field and corresponding part of the total energy.

An evaluation of the model shows that features which depend on the conservation laws or which involve the pressure balance are well reproduced (Janhunen and Palmroth, 2001). This includes the magnetopause, the bow shock, the cross-tail and magnetopause current systems, the plasma sheet and tail lobes. Features that depend on different parallel/perpendicular physics or multiple temperatures are badly reproduced. Unfortunately, this concerns many of the auroral phenomena.

Chapter 5

Instrumentation

For a statistical study of polar arcs appearing during 3 winter months in 1998/1999 UV images from the POLAR spacecraft and solar wind data from the ACE solar wind monitor are used (Paper 3). The main parameters of these two spacecrafts are here briefly described.

5.1 The Polar UV imager

POLAR was launched in early 1996 into an 86^o inclination orbit, with an apogee of 9 R_E in the northern hemisphere and a perigee of 1.8 R_E. Since then it moved slowly equatorward. In winter 1998/1999 apogee was approximately at 55 degrees latitude.

The UV experiment is one of four instruments of the Polar spacecraft. It is a two dimensional spatial imager which produces global images of the Earth's auroral regions in the far ultraviolet wavelength range (Torr et al., 1995). The UV camera has an 8-degree field of view which allows to imagine the entire auroral region above 60 degrees latitude at spacecraft altitudes greater than 6 R_E. It is mounted on a pointable despun platform. This allows, in spite of the spacecraft rotation, a constant imaging of the auroral zone for a significant fraction of Polars' orbit. In winter 1998/1999, the UV instrument provided global auroral images of the northern hemisphere, during approximately 10 hours during each 18-hour orbit. During an additional 4 hours, at least some part of the oval was visible. The resolution of the images is 0.5 degrees in latitude at apogee; thus a single pixel projected to 100 km altitude from apogee is approximately 50x50 km. Away from apogee the imager can detect even smaller spatial scales.

The UV camera images the aurora every 37 seconds in the ultraviolet region of the spectrum using four narrow band filters. The peak wavelength and bandwidth of each filter are listed in Table 5.1. The integration times are 18 and 36 seconds, respectively. The system has been designed to provide ten orders

of magnitude blocking against longer wavelength (primarily visible) scattered sunlight. Both nightside and sunlit auroral features can be recognized on the images. Still, the dayside part of the aurora appears much less sharp and only bright auroral structures can be recognized. For the statistical study in Paper 3 the LBH long filter is chosen, where wavelengths between 160 and 180 nm are passed. The LBH emissions are the result of excitation of N_2 by electron impact. N_2 is most common at lower layers of the ionosphere at about 120 km altitude. Since the emissions in the wavelengths passed by the filter are not significantly absorbed by the atmosphere, the intensity of the emission is nearly directly proportional to the electron energy flux into the ionosphere. The dynamic range of the UV instrument is extremely high. It can be positioned within an overall gain range of 10^4, allowing measurement of both the very weak polar cap emissions and very bright aurorae. The overall sensitivity of the instrument is about 10 Rayleigh which is equivalent to being able to detect objects more than 100 times fainter than the eye can detect.

Table 5.1: The different UV filters on Polar

Filter	Peak Wavelength	Bandwidth
1304	130.4 nm	40 nm FWHM
1356	135.6 nm	50 nm FWHM
LBH short	150.0 nm	141 - 158 nm (10 % of peak)
LBH long	170.0 nm	164 - 178 nm (10 % of peak)
Solar	180.0 nm	176 - 190 nm (10 % of peak)

Two malfunctions on the Polar UVI experiment slightly reduce the image quality: The sharpness of the images is reduced by a periodic wobble of the spacecraft. The wobbling is caused by the unsuccessful deployment of one of the electric field booms. Perpendicular to the wobble the image resolution is unaffected. In the wobble direction, the images are smeared by a maximum of 10 pixels. To protect the UV camera against contamination, an aperture door is closed over the lens during times the UV camera is not operating. Due to an instrument malfunction the door is sometimes closed even during operation times. This happened during 20 percent of the time which is covered by the statistical study in Paper 3. As the door is a transparent MgF window, measurements can still be made when it is closed but the image sensitivity is reduced by about 50 percent so that faint polar auroral arcs cannot be detected.

5.2 The ACE solar wind monitor

The Advanced Composition explorer (ACE) orbits about the L1 Lagrange point upstream in the solar wind since mid 1997. As the typical distance between ACE and Earth is around 200 R_E, large time delays about one hour have to

be taken into account. The solar wind conditions may have changed slightly when they reach the magnetopause. However, looking for large-scale changes, small deviations from the correct solar wind situation are negligible. Due to its continuous monitoring during the time period the statistics is performed it is the most suitable satellite for a statistical analysis covering several months of data.

For the statistical study in Paper 3, 5-minute averaged ACE data have been used to correlate the auroral precipitation pattern with solar wind proton number density, the solar wind bulk speed and the interplanetary magnetic field. The IMF is measured by the Magnetic Field Experiment (MAG) on board ACE. The Solar Wind Electron, Proton, and Alpha Monitor (SWEPAM) measures the solar wind plasma electron and ion fluxes. Further details about the MAC instrument can be found in Smith et al. (1998), the SWEPAM instrument is described in McComas et al. (1998).

Chapter 6

Summary of results and outlook

Understanding of the dynamics of the magnetosphere-ionosphere system, the coupling between the two regions, and its dependence on interplanetary conditions in particular, is of fundamental importance to almost every aspect of magnetospheric and ionospheric physics. During periods of southward IMF the relationships between auroral morphology and the large-scale magnetosphere topology are quite well established. The state of the magnetosphere during northward IMF has gained far less attention in the research community. As a result, it is much less explored. The nearly closed state of the magnetosphere during northward IMF is indicated by the absence of strong auroral activity such as large-scale substorms. The generally weak auroral emissions reflect the low rate of energy coupling between the solar wind and the magnetosphere. However, the existence of auroral arcs poleward of the main oval during northward IMF, and their often dynamic evolution, indicates that a positive IMF B_z component does not automatically mean that the magnetosphere turns into a quiet steady state. Studying polar auroral arcs not only improves the knowledge of this auroral phenomenon itself but also enhances the insight into the ionosphere-magnetosphere coupling during northward IMF.

6.1 Statistical results

Large-scale polar auroral arcs have been known since the late 1970's. However, it has for a long time been unclear how they emerge and what causes their motion. A major obstacle toward a better understanding were the limitations of the available datasets. The entire evolution of large-scale polar arcs could not be followed in detail due to a limited field of view (ground-based cameras) or a non-continuous coverage of the auroral zone by global imagers on satellites

(DE-1, Viking). A stationary solar wind monitor sunward of the Earth was missing, so that only in single cases polar arcs could be compared to solar wind data when satellites (like IMP-8 or ISEE-3) were directly in front of the Earth. It was not before the mid 1990's that a much better coverage became available. The UVI instrument on the Polar spacecraft produced in 1998/1999 during 75% of the time every minute global auroral images. The stationary ACE solar wind monitor collects since 1997 continuously solar wind data at 220 R_E sunward from the Earth. These two spacecraft provide a very good data material for a statistical study of large-scale polar auroral arcs. For the first time the entire time evolution of each polar arcs and the corresponding solar wind data could be studied.

Paper 3 presents the results of such a statistical study. All polar arcs visible in the Polar UVI images of the northern polar cap are registered during the period of three winter months in 1998/1999. The comparison of over 200 different polar arc events leads to the recognition of repeated patterns in the arc evolution which results in a new categorization into five different arc types: bending arcs, oval-aligned arc, moving arcs, midnight arcs and multiple arcs. Figure 6.1 shows a schematic of how the first four arc types develop in time. Polar arcs that are too short, faint or short-lived are excluded from the above categorization. As could be expected, no clear dependence on solar wind parameters is found for those events. Of the remaining clear polar arc events not all can be sorted into the above groups because of missing UV images during major parts of their evolution. This reduces the number of large-scale polar arcs studied in detail to 74 events.

Due to continuous monitoring by ACE, the solar wind conditions during polar arc events can be compared to the average solar wind distribution of the entire statistical time period. Binning the data into four intervals that correspond to an equal solar wind distribution during the statistical time period, any deviation from the average solar wind distribution is easily detected. This allows conclusions regarding the importance of different solar wind parameters for the occurrence of polar arcs: the IMF and the solar wind velocity play a significant role for the polar arc occurrence while the influence of the solar wind density seems to be negligible. The often neglected time history of the solar wind around each event is taken into account as well. It reveals that the evolution of a polar arc depends crucially on IMF conditions one to two hours before its appearance. This result indicates that slow changes in the entire magnetosphere topology may be involved in the formation of a polar arc.

A detailed comparison with solar wind parameters confirms many previous results regarding the IMF control of polar arcs, especially the IMF B_y dependent arc motion and the recently discovered role of IMF B_y and IMF B_z sign changes as a trigger mechanism of polar arcs. Here, it is shown that the different IMF clock angle rotations cause different types of arcs to occur: bending arcs are connected to IMF B_z sign changes and moving arcs to IMF B_y sign changes. In fact, it is found that each arc type identified from images is related to an entire

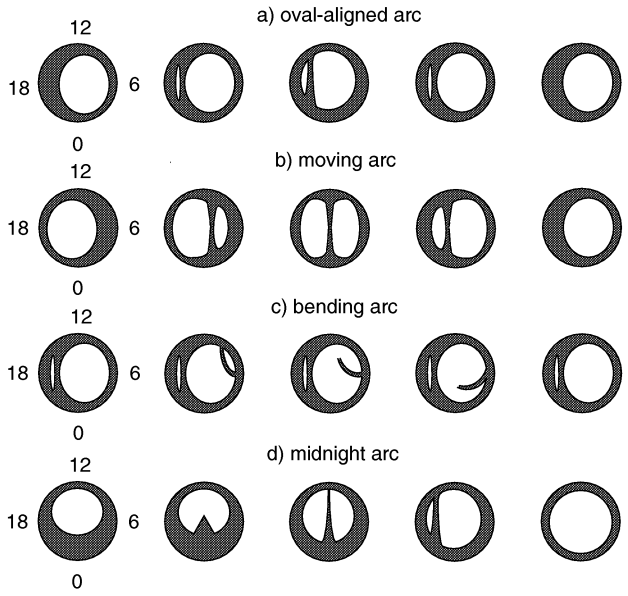

Figure 6.1: Schematic showing the temporal evolution of all clear polar arc types introduced in the study except multiple arcs.

set of characteristic solar wind conditions (Table 6.1).

Marking all existing polar arcs on a time axis results in a pattern with a clear clustering of polar arc events around several days and the lack of such during others. This can not be entirely explained by the sign of the IMF B_z component (being positive when polar arcs occur and negative during their absence) nor by a correlation with any other solar wind parameter. After performing a statistical analysis, the dependence of polar arcs on a high electromagnetic energy flux of the solar wind is found. A parameter is introduced (anti-epsilon $= vB^2cos^4(\theta/2)l_0^2/\mu_0$) connecting the high occurrence frequency of polar arcs to both northward IMF and high solar wind energy. It would be interesting to find out whether the energy dumped into the polar cap in form of particle precipitation of large-scale polar arcs is related to the anti-epsilon parameter as well. Further research is necessary to investigate this relation. Based on the statistical and modeling results of this thesis it is here suggested that for northward IMF the solar wind energy is not (as for southward IMF) stored in the magnetosphere. Instead, large-scale topological changes of the magnetotail are enforced, which force a fraction of closed field lines to map into the polar cap (Paper 2 and 4). With this topological deformation, the possibility for auroral arcs to occur on closed field lines poleward of the main oval arises.

Table 6.1: Main characteristics of the different polar arc types

arc type	lifetime	IMF	$\|v\|$	$\|IMF\|$
bending arcs:	0.5 h	B_z sign change	average	average
oval-aligned arcs:	0.5-4 h	$\|B_y\| \sim B_z^+$	average	high
moving arcs:	2 h	B_y sign change	high	high
midnight arcs:	1.5 h	varying	high	average
multiple arcs:	2 h	varying	high	high

The categorization of polar arcs given in this statistical study should be regarded as only one step toward a better understanding of polar arcs. The enormous variety of different polar arc evolutions would allow to sort events into more (sub)groups than proposed in Paper 3. This requires, though, a much larger dataset. In the existing work the number of events per group is as small as 6 to 28 events. As the categorization into different polar arc types is exclusively based on the visual differences in the UV images it is disregarded that the brightenings seen on the UV images can in fact be caused by different particle populations. A detailed particle analysis of each arc type would be necessary to find out whether different polar arc types represent the same auroral phenomena (only their shape being dependent on the IMF trigger) or whether these are fundamentally different types of polar arcs being caused by different mechanisms. Especially the rarely occurring midnight arcs and the more common but extremely faint bending arcs deserve a more detailed study. So far, these two arc types have hardly been reported in literature. Understanding the arc motion of the simple arc types is a prerequisite for the interpretation of more complicated multiple arc events.

Not included in this statistical work is a (simultaneous) analysis of both hemispheres. Such an examination, based on global auroral images would help to find out about the differences between summer and winter conditions but also to gain more insight in possible symmetries between arc motions in the northern and southern polar cap, as expected from magnetosphere modeling. However, it is very difficult to discern the faint polar auroral arcs on the dayglow background within the bright summer polar cap.

A subject, mentioned only briefly in Paper 3 is the connection between substorms and arcs. Some polar arcs fade shortly after a substorm onset, others survive the onset up to 2 hours, in a third scenario a substorm-like brightening 'moves up' along the arc. This is an exciting research subject as the two auroral phenomena are caused by distinctively different mechanisms. Substorms occur due to instabilities inside the tail whereas polar auroral arcs are probably connected to large-scale changes of the tail topology. Their simultaneous occurrence can help to gain more insight into the magnetosphere-ionosphere coupling processes during a transitional phase between the state of the magnetosphere typical for northward IMF and typical for southward IMF.

6.2 Model results

A detailed review of polar arc models is given in Paper 3. The different polar arc models are discussed with regard to the new findings of the statistical study. Here, only those models are mentioned which have a connection to oval-aligned or moving polar arcs. Those two arc types are addressed in the second part of the thesis. With the help of magnetosphere models, the topological link between the magnetotail and the polar cap boundary is examined in detail and leads to a new polar arc model for moving polar arcs.

The source region of field-aligned currents associated with large-scale polar arcs has been generally agreed on to be the plasma sheet or its boundary layer. This means that large-scale polar arcs lie on closed field lines. In case a polar arc appears near an oval boundary (oval-aligned arc), it can be assumed that this arc lies at the outermost boundary of the closed field line region which is polewardly extended at that oval side. The poleward expansion occurs when the plasma sheet is strongly twisted, as typical for non-zero IMF B_y (Meng,1981; Makita 1991). This is shown in detail in Paper 1. However, a polar arc, located in the center of the polar cap along the Sun-Earth line (such as moving arcs during part of their life-time), does not map into the plasma sheet but into the open field line region of the tail lobes, if a standard magnetosphere topology is assumed where a butterfly shaped plasma sheet reaches high latitudes only near the flanks. To resolve this contradiction, different topologies of the magnetotail have been proposed. Many models include a bifurcation of the tail plasma sheet in some way or another, but can not explain how this topology may arise (Frank et al., 1986, Huang et al., 1989, Chang et al., 1998).

The polar arc model presented in this thesis does not need such a plasma sheet bifurcation for a bridge of closed field lines to appear in the middle of the polar cap. Observations show that a moving polar arc occurs after an IMF B_y sign change during northward IMF (Cumnock et al., 2002). It is known that the magnetotail is twisted for nonzero IMF B_y. Thus, the magnetotail will after an IMF B_y sign reversal undergo a reconfiguration which will finally lead to a twisting of the tail into the opposite sense. The basic idea of this model is that the magnetotail does not react at once on a change of the IMF but will change successively, starting at the near-Earth tail and ending at the far magnetotail. This means, the rotation of the magnetotail twist will occur further downtail with a time delay such that in an intermediate state the earthward and tailward regions of the plasma sheet will be oppositely twisted (Figure 6.2). During the transition period the closed field line region is no longer identical with the plasma sheet region. Field lines that originate in the far tail plasma sheet map into the near-Earth tail lobes and further into the polar cap. The polar cap is bifurcated by a bridge of closed field lines which is interpreted as the location of a possible polar arc. The tailward propagation of the twist rotation corresponds to a poleward motion of the closed field line bridge, as expected for a moving polar arc. With this model, the occurrence and motion of a moving polar arc

finds its natural explanation in the large-scale tail reconfiguration as a reaction to an IMF B_y sign change.

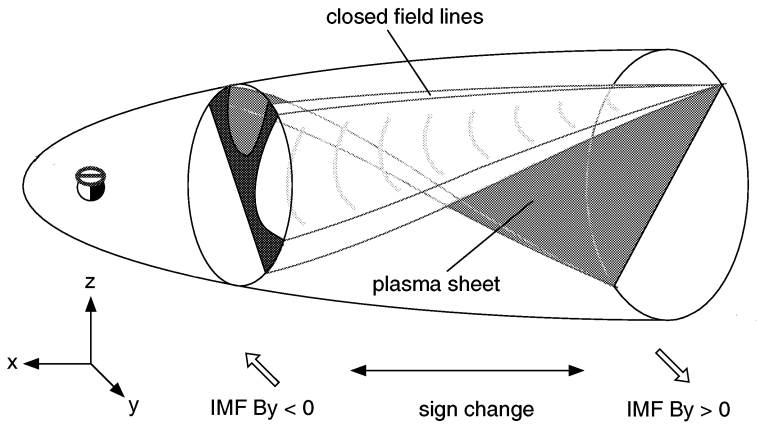

Figure 6.2: The tail model for moving arcs: A rotation of the tail twist caused by an IMF B_y sign change leads to a bifurcation of the closed field lines in the near-Earth tail. The bifurcated region maps to a polar auroral arc which moves from one side of the oval to the other while the rotation of the tail twist propagates tailward.

In Paper 1 the method is described, which transforms the standard magnetospheric field of the T89 model into a state typical for non-zero IMF B_y. The IMF B_y induced effects in the magnetotail include the bending of the magnetic field lines and a twisting of the tail plasma sheet. The manipulation of the tail field to include the IMF B_y effects is done by a superposition of magnetic field components. The extra B_y field, responsible for the dawn-dusk bending of the field lines is chosen such that it corresponds to the observed additional field that occurs for non-zero IMF B_y (Kaymaz et al., 1994). To create a twisting of the current sheet similar to that shown in Kaymaz et al., 1994 a B_x field is added which moves the return points of the magnetic field lines away from the equatorial plane (the position of the B_x sign reversal gives the location of the current sheet). Observations indicated a tailward increase of the tail twisting but the degree of the twisting has to be guessed. A strong tailward increase of the plasma sheet twist is assumed, basically because only a strong tail twist leads to any clear displacement of the polar cap boundary. Observations by Owen et al. (1995) and the simulation results of Paper 3 show that this assumption holds only for northward IMF conditions.

The effects of the new field on the mapping between tail and ionosphere are studied in detail. Mapping from the tail current sheet (B_x sign reversal) to the

Earth gives the boundary between the open and closed field lines. In the paper it is shown that a clockwise (looking tailward) twisting of the magnetotail current sheet is connected to a poleward (equatorward) displacement of the polar cap boundary at the morning (evening) side of polar cap boundary. The bending of the closed field lines leads to a displacement of the ionospheric footprints in dawn-duskward direction such that the entire polar cap boundary is rotated in clockwise direction when looking toward the Sun.

In Paper 2 the same modified version of the T89 model as in Paper 1 is used, but a gradual change of the magnetotail twist and field line bending in downtail direction is enforced. As the T89 model is time independent, a stepwise motion of the location of the twist reversal center is assumed to correspond to a tailward progression of the IMF B_y sign change. Mapping from the tail current sheet to the Earth results in a bar of closed field lines poleward of the polar cap boundary. The tailward displacement of the sign reversal region results in a more poleward displacement of the closed field line bar. This bar of closed field lines is interpreted as the location where a moving polar arc may occur. To keep the magnetic field divergence free an additional term is added at the tail flanks around the region where the tail twist is zero. It has the same sign as IMF B_y earthward of the twist reversal location. This additional component changes the mapping results very little but indicates that an IMF B_y induced change of the tail topology is not linear but moves from the flanks to the tail center. From B^2 isocontour plots of tail cross sections it can be seen that the tail plasma sheet (assumed to approximately follow B^2 isocontours) is not bifurcated, but only the closed field line region.

In Paper 1 and Paper 2, the mapping is done from the tail current sheet between -10 and -60 R_E to the ionosphere and the T89 modification is done to correspond the changes inside the magnetotail only, not the dayside of the magnetosphere. In a consequence the closed field line region does reach the noon part of the polar ionosphere, neither does in Paper 2 the bar of closed field lines poleward of the oval reach to the dayside. Furthermore, the closed field line bar does not move over the entire polar cap. The absence of plasma populations and their interaction with the magnetic field, the time independence of the model and the absence of field-aligned currents producing the aurora limits the model's predicting power. However, the model results clearly show that a magnetic tail topology is possible where the closed field line region in the tail and the polar cap are bifurcated but not the plasma sheet.

In Paper 4 different synthetic runs are performed with the GUMICS-4 MHD code. They include several constant IMF runs for different IMF clock angles and two IMF B_y sign change runs with different change rates during northward IMF. The constant IMF runs are done to find out about the effect of different ratios between IMF B_z and IMF B_y on the magnetotail topology.

The simulation results show the importance of northward IMF for the occurrence of closed field lines on very high latitudes. The tailward length and the shape of the closed field line region vary strongly for different clock angle direc-

tions. For southward IMF the closed field line region is quite short, extending only to 20 R_E in tailward direction. The length increases with decreasing clock angle. Only during nearly northward IMF (in the constant and the sign change case) the tail becomes longer than 80 R_E. In that case, the far tail closed field line region maps high into the near-Earth tail lobes. The plasma sheet twist increases tailwardly. Only for a long tail, the far tail plasma sheet twist is large enough for field lines to map to high latitudes in the near Earth tail. In Paper 3 it has been shown that during solar wind conditions with several hours of constant IMF with a nonzero B_y and a northward B_z component only the oval-aligned arc type occur. The oval-aligned arc occurs on the dawn (dusk) oval side for dawnward (duskward) IMF. In Paper 1 and in the simulations this is the oval side where the polar cap boundary is on very high latitudes. The results confirm that oval-aligned arcs occur on the poleward boundary of the closed field line region which maps to a strongly twisted magnetotail, as is the case only for a strong northward IMF component.

The IMF B_y sign change runs confirm the polar arc model proposed in Paper 2. In the simulations the bridge of closed field lines moves over the entire polar cap for the B_y sign change case. Furthermore, the MHD simulations reveal several new aspects. As indicated in the model results of Paper 2, the magnetosphere reacts with a time delay not only in tailward direction but also from the flanks to the tail center. In contrast to the T89 model where a linear change of the tail twist was enforced, the tail plasma sheet starts to twist into the new direction at the flanks such that in an intermediate state it gets a horizontal 'S' shape. Comparing the simulation results for the slow and the fast IMF B_y sign change runs shows that the different change rates of the IMF B_y reversal do not result in major differences of arc motion and tail configuration despite the thickness of the bifurcated region in polar cap and magnetotail.

From these results it follows that currents producing polar arcs originate in the far tail. The main oval has its source region much closer to the Earth. This would explain the rapid changes of the polar arcs, sometimes broadening, sometimes nearly disappearing while the main oval keeps its circular shape. To test these ideas, it would be necessary to study the relationship between auroral oval boundary and polar cap boundary during constant northward IMF in detail.

Several steps are missing toward a complete understanding of the evolution of a moving polar arc. The biggest question arises about the lack of polar arc currents in the simulations. The reported bridge of closed field lines crossing the model polar cap does not correspond to field-aligned currents at this location. In fact, the MHD results do not indicate any localized current sheet inside the polar cap. Such thin current sheets can apparently not be created in an global MHD model. Here, the limitations of a large-scale magnetosphere MHD code becomes visible and it is not obvious how to overcome this problem.

The polar arc life time appearing in the simulations is a factor 2 or 3 shorter than observed. Whether this can be explained by too short a model tail or

by too fast a reconfiguration of the tail toward a new steady state situation or if some fundamental physical mechanism is not appearing in MHD, remains to be studied. Studying the magnetotail would help to understand where the discrepancies between model simulations and observations occur. There have been observational studies dealing with the twisting of the magnetotail due to nonzero IMF B_y (Kaymaz et al., 1994; Owen et al., 1995) but tail observations during a rotation of the IMF clock angle have not been published yet. Such observations could be compared with the simulation results of Paper 4. Most promising would be a conjunction study including polar arc images or, alternatively, a statistical study focusing on the magnetotail current sheet motion after an IMF B_y sign change.

One note of caution has to be added. To understand the basic mechanism that causes polar arcs, idealized solar wind conditions have been assumed in this work: the solar wind and the IMF conditions applied on the model are either constant or change linearly. In reality, the solar wind variations are frequent and complicated. They influence the magnetosphere on many different time scales. Some solar wind changes have a direct effect on the auroral precipitation pattern, i.e., solar wind pressure pulses causing an immediate brightening at the dayside auroral oval or IMF B_z northturns triggering a substorm within minutes. Other changes, like an IMF B_y sign reversal, involve large-scale tail reconfigurations that take more than 40 minutes. Internal instabilities may occur periodically, like periodic substorm cycles within a magnetic storm. The magnetospheric response to certain solar wind conditions can involve several different time scales and is not easy to decompose into its components.

In summary, several aspects of polar auroral arcs have been examined in detail in this thesis. The auroral precipitation pattern of polar arcs has been studied extensively. A clear connection between polar arc morphology and solar wind parameters has been shown. This result suggests that certain solar wind conditions serve as a trigger for magnetospheric changes which allow large-scale polar arcs to occur. For two types of polar arcs (oval-aligned and moving arcs) the solar wind-magnetosphere-ionosphere coupling has been studied in detail. Both occur for small IMF clock angles, either transitionally (moving transpolar arcs) or constantly (oval-aligned arcs), and the magnetotail is long and highly twisted at its tailward end. This tail topology causes field lines to map poleward of the average polar cap boundary. The polewardly displaced closed field line region is a probable location for polar arcs to occur. The occurrence and motion of a moving polar arc is explained with a simple magnetotail reconfiguration, triggered by an IMF B_y sign change during northward IMF B_z. For the other polar arc types it remains to be shown whether these are triggered by similar mechanisms as proposed for moving arcs or whether these are more probable to fit into the framework of polar arc models suggested by other authors.

References

Akasofu, S.-I., The solar wind-magnetosphere energy coupling and magnetospheric disturbances, *Planet. Space Sci., 28*, 495, 1980.

Axford, W. I., and C. O. Hines, A unifying theory of high-latitude geophysical phenomena and geomagnetic storms, *Can. J. Phys., 39*, 1433, 1961.

Bonnell, J., R. C. Elphic, S. Palfery, R. J. Strangeway, W. K. Peterson, D. Klumpar, C. W. Carlson, R. E. Ergun, and J. P. McFadden, Observations of polar cap arcs on FAST, *J. Geophys. Res., 104*, 12:669, 1999.

Chang, S.-W. et al., A comparison of a model for the theta aurora with observations from Polar, Wind and SuperDARN, *J. Geophys. Res., 103*, 17:367, 1998.

Cowley, S. W. H., A qualitative study of reconnection between the Earth's magnetic field and an interplanetary field of arbitrary orientation, *Radio Science, 8*, 903, 1973.

Crooker, N. U., Dayside merging and cusp geometry, *J. Geophys. Res., 84*, 951, 1979.

Crooker, N. U., G. L. Siscoe, and F. R. Toffoletto, A tangent subsolar merging line, *J. Geophys. Res., 95*, 3787, 1990.

Cumnock, J. A., J. R. Sharber, R. A. Heelis, L. G. Blomberg, G. A. Germany, J. F. Spann, and W. R. Coley, Interplanetary magnetic field control of theta aurora development, *J. Geophys. Res., 107*, 17:489, 2002.

Dungey, J. W., Interplanetary magnetic field and the auroral zones, *Phys. Rev. Lett., 6*, 47, 1961.

Eather, R. H., *Majestic Lights*, AGU, Washington DC, 1980.

Fairfield, D. H., On the average configuration of the geomagnetic tail, *J. Geophys. Res., 84*, 1950, 1991.

Frank, L. A., J. D. Craven, J. L. Burch, and J. D. Winningham, Polar view of the Earth's aurora with Dynamic Explorer, *Geophys. Res. Lett., 9*, 1001, 1982.

Frank, L. A., et al., The theta aurora, *J. Geophys. Res., 91*, 3177, 1986.

Frank, L. A., and J. D. Craven, Imaging results from Dynamics Explorer 1, *Rev. Geophys., 26*, 249, 1988.

Gombosi, T. I., D. L. DeZeeuw, R. M. Hberli, K. G. Powell, and P. Song, The length of the magnetotail for northward IMF: Results of 3D MHD simulations, in *Physics of Space Plasmas,*, ed. T.Chang and J.R. Jasperse, vol. 15, p. 121, MIT Press, Cambridge, 1998.

Huang, C. Y., J. D. Craven, and L. A. Frank, Simultaneous observations of a theta aurora and associated magnetotail plasmas, *J. Geophys. Res., 94*, 10137, 1989.

Iijima, T., and T. A. Potemra, Field-aligned currents in the dayside cusp observed by Triad, *J. Geophys. Res., 81*, 5971, 1976.

Janhunen, P., and A. Huuskonen, A numerical ionosphere-magnetosphere coupling model with variable conductivities, *J. Geophys. Res., 98*, 9519, 1993.

Janhunen, P., GUMICS-3 - A global ionosphere-magnetosphere coupling simulation with high ionospheric resolution, *ESA Sympos. Proc., SP-392*, 233, 1996.

Janhunen, P., and M. Palmroth, some observational phenomena are well reproduced by our global MHD while others are not: remarks on what, why and how, *J. Adv. Space Res., 28*, 1685, 2001.

Jordan, C. E., Empirical models of the magnetospheric magnetic field, *Rev. Geophys., 32*, 139, 1994.

Kaymaz, Z., Empirical studies of the magnetosheath and tail field and current structure, and model comparisons, *PhD Thesis*, University of California, Los Angeles, 1993.

Kaymaz, Z., G. L. Siscoe, J. G. Luhmann, R. P. Lepping, and Ch.T. Russell, Interplanetary magnetic field control of magnetotail magnetic field geometry: IMP 8 observations, *J. Geophys. Res., 99*, 11:113, 1994.

Kaymaz, Z., and G. L. Siscoe, Open geometry of the magnetotail cross section, *J. Geophys. Res., 99*, 14:829, 1998.

Kim, K.-H., N. Lin, C.A. Cattell, Y. Song, and D.-H. Lee, Evidence for component merging near the subsolar magnetopause: Geotail observations, *Geophys. Res. Lett., 29*, 10:1029, 2002.

Kivelson, M.G., and C. T. Russell (Eds.), *Introduction to Space Physics*, Cambridge University Press, Melbourne, Australia, 1995.

Lockwood, M., Solar wind magnetosphere coupling, *Technical report 97/53*, EISCAT Scientific Association, 1997.

Lui, A. T. Y., Polar wind influence on magnetotail configuration and dynamics, in *Solar wind magnetosphere coupling*, Ed. Y. Kamide and J. A. Slavin, 671, 1986.

Makita, K., C.-I. Meng, and S.-I. Akasofu, Transpolar auroras, their particle precipitation, and IMF B_y component, *J. Geophys. Res., 96*, 14:085, 1991.

Mawson, D., Auroral observations at the Cape Royds Station, Antarctica, *Trans. Proc. Roy. Soc. S. Aust., XL*, 151, 1916.

McComas, D. J., S. J. Bame, P. Barker, W. C. Feldman, J. L. Phillips, P. Riley, and J. W. Griffee, Solar Wind Electron Proton Alpha Monitor (SWEPAM) for the Advanced Composition Explorer, Space Sci. Rev., 86, 563, 1998.

Meng, C.-I., Polar cap arcs and the plasma sheet, *J. Geophys. Res., 8*, 273, 1981.

Owen, C. J., J. A. Slavin, I. G. Richardson, N. Murphy, and R. J. Hynds, Average motion, structure and orientation of the distant magnetotail determined from remote sensing of the edge of the plasma sheet boundary layer with $E > 35$ keV ions, *J. Geophys. Res., 100*, 185, 1995.

Palmroth, M., Solar wind-magnetosphere interaction as determined by observations and a global MHD simulation, *PhD Thesis*, FMI, Helsinki, 2003.

Parks, G. K., *Physics of Space Plasmas: An Introduction*, Addison-Wesley Publ. Comp., Redwood City, 1991.

Russell C. T., J. Berchem, and J. G. Luhmann, On the source region of flux transfer events, *J. Adv. Space Res., 5*, 363, 1985.

Smith, C. W., J. L'Heureux, N. F. Ness, M. H. Acuna, L. F. Burlaga, and J. Scheifele, The ACE magnetic fields experiment, Space Sci. Rev., 86, 613, 1998.

Sonnerup, B. U. ., Magnetopause reconnection rate, *J. Geophys. Res., 79*, 1546, 1974.

Stern, D. P., and N. A. Tsyganenko, Uses and limitations of the Tsyganenko magnetic field models, *EOS Transactions, AGU, 73*, 489, 1992.

Torr, M. R., et al., A far ultraviolet imager for the international solar-terrestrial physics mission, *Space Sci. Rev., 71*, 329, 1995.

Tsyganenko, N. A., A magnetospheric magnetic field model with a warped tail current sheet, *Planet. Space Sci., 37*, 5, 1989.

Tsyganenko, N. A., Global configuration of the magnetotail current sheet as derived from Geotail, Wind, IMP 8 and ISEE 1/2 data, *J. Geophys. Res., 103*, 6827, 1998.

Valladares, C. E., H. C. Carlson Jr., and K. Fukui, Interplanetary magnetic field dependency of stable sun-aligned polar cap arcs, *J. Geophys. Res., 99*, 6247, 1994.

Wilcox, J. and N. Ness, Quasi-stationary corotating structure in the interplanetary medium, *J. Geophys. Res., 70*, 1233, 1965.

Yamada, M., Review of controlled laboratory experiments on physics of magnetic reconnection, *J. Geophys. Res., 104*, 14:529, 1999.

Paper 1

GEOPHYSICAL RESEARCH LETTERS, VOL. 23, NO. 18, PAGES 2561-2564, SEPTEMBER 1, 1996

The influence of IMF B_y on the mapping between the Earth's magnetotail and its ionosphere

A. Kullen and L. G. Blomberg

Division of Plasma Physics, Alfvén Laboratory, Royal Institute of Technology, Stockholm, Sweden

Abstract. It is well known that the dawn-dusk component of the interplanetary magnetic field (IMF) creates asymmetries in the magnetotail. The main effects are a weak nonuniform penetration of IMF B_y into the tail and a rotation of the whole tail current sheet. In this study we modify the Tsyganenko (1989) model to simulate the IMF B_y induced tail effects. By field line mapping we examine how different regions of the magnetosphere and ionosphere are influenced by the IMF B_y tail effects. The plasma sheet is shown to rotate around the central axis of the magnetotail. The mapping from the plasma sheet to the ionosphere for nonzero IMF B_y shows a change in the geometry of the auroral oval. The whole oval rotates, a local bulge occurs near midnight and the thickness of the oval is different in the morning and the evening sector. Simple geometrical considerations show that the tilting of the field lines caused by IMF B_y leads to a rotation of the oval, whereas the rotation of the tail current sheet is reponsible for the thickness variations along the oval. These results fit very well with the observed auroral distribution for an IMF with a dawnward or duskward direction.

Introduction

It was discovered very early on that there is a correlation between the y-component of the interplanetary magnetic field (IMF) and the y-component of the magnetic field in the magnetotail [*Meng and Anderson*, 1974]. The main part of the IMF B_y is shielded from the tail, but about $10\%-20\%$ of the IMF B_y penetrates into it. Later it was found that the penetration of IMF B_y is nonuniform. The shielding is stronger in the lobes than in the plasma sheet [*Fairfield*, 1979; *Lui*, 1986], it is stronger in the center of the tail than near the magnetopause flanks [*Cowley and Hughes*, 1983; *Pudovkin*, 1991], and it is stronger in the far tail than near the Earth [*Sergeev*, 1987]. A rotation of the tail current sheet has been reported by several authors [e.g., *Sibeck et al.*, 1986; *Tsyganenko*, 1990; *Hammond et al.*, 1992]. It seems that the rotation increases with distance from the Earth. *Cowley* [1981] suggested that the rotation could even reach 90° in the very far tail. A recent study of satellite data by Kaymaz et al. [1994] confirms the asymmetries which are created by IMF B_y. Figure 1a is a schematic which shows the IMF B_y effects on the tail.

The effects of IMF B_y on the geometry of the auroral oval have been observed from many satellite pictures of the auroral oval [e.g., Jankowska et al., 1990; *Elphinstone et al.*, 1990]. The whole auroral oval rotates in a clockwise (anticlockwise) direction for duskward (dawnward) IMF B_y in the northern hemisphere. The morning sector of the auroral oval gets narrower (broader) and the evening sector gets broader (narrower) for positive (negative) IMF B_y. This leads to a translation of the poleward oval boundary towards higher and lower latitudes for the broader and narrower side, respectively [*Lassen and Danielsen*, 1978]. A local bulge of the poleward auroral oval boundary appears around 21 MLT(3 MLT) for positive (negative) IMF B_y. In Figure 1b the change of the geometry of the auroral oval is shown schematically.

IMF shielding has been discussed in the context of magnetosheath field line draping [*Siscoe and Sanchez*, 1987; *Ohtani and Kokubun*, 1991]. There have also been some explanations for the (nonuniform) penetration of IMF B_y in the tail [e.g., *Cowley*, 1981; *Moses and Crooker*, 1985; *Voigt and Hilmer*, 1985; *Sergeev*, 1987] and related effects. Cowley explained 1981 an assumed uniform B_y penetration field in terms of efficiency of reconnection, but usually the shielding of the main part of the IMF has not been discussed in this context.

With this study we attempt to clarify how IMF B_y-induced effects on the magnetotail influence other parts of the magnetosphere and ionosphere. We model the IMF B_y effects on the tail by changing an existing model of the magnetospheric magnetic field. With field line mapping we study how the geometry of the magnetotail, the plasma sheet and the auroral oval change for IMF B_y and estimate the associated current systems. The validity of the results is closely related to the relevance of the chosen model. In this study we use the semiempirical Tsyganenko 1989 (T89) model. It is very flexible (K_p index, dipole tilt as input), is based on a large dataset, and is valid out to $x = -70R_E$ in the far tail. However, there are some limitations of the model [e.g., *Fairfield*, 1991; *Stern and Tsyganenko*, 1992 and references therein; *Kaufmann et al.*, 1993]. Of importance here is the fact that for low K_p levels the B_z values at the neutral sheet are too low, and on the flanks ($|y| > 25R_E$) they are even negative. Hence the neutral sheet flanks map to much too low latitudes in the ionosphere and have to be neglected.

Paper number 96GL02305
0094-8534/96/96GL-02305$05.00

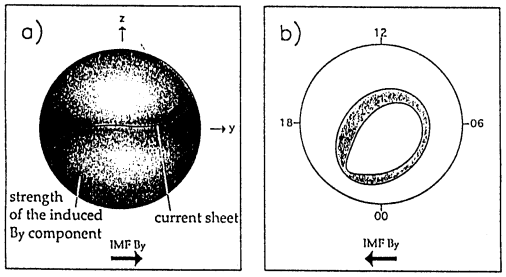

Figure 1. a) A schematic showing the effects of IMF B_y on the magnetotail: Nonuniform penetration of IMF B_y and nonuniform rotation of the current sheet. b) A schematic showing the effects of IMF B_y on the auroral oval: Rotation of the auroral oval, narrowing (broadening) of the morning (evening) sector of the oval and a local bulge near midnight.

The Model

To represent the effects of IMF B_y in the tail, a magnetic field is superimposed on the T89 model. We have attempted to create a magnetic field which resembles qualitatively the IMF B_y penetration field in the tail and the current sheet rotation in the study of *Kaymaz et al.* [1994]. To get the conditions of a quiet magnetosphere with a plane neutral sheet, we set K_p index and dipole tilt to zero.

The divergence-free added magnetic field has the following components

$$B_x = B_{y,IMF}[-c_3 y - \frac{2c_2 b_3}{b_2^2} y e^{-(\frac{y}{b_2})^2+\frac{x}{b_3}}], \quad (1)$$

$$B_y = B_{y,IMF}[c_1 e^{-(\frac{x}{b_1})^2} + c_2(1 - e^{-(\frac{y}{b_2})^2})e^{\frac{x}{b_3}}, \quad (2)$$

$$B_z = 0. \quad (3)$$

The two terms of B_y create a nonuniform B_y field, which is stronger in the plasma sheet than in the lobes (e^{-z^2}), stronger near the boundary than in the center ($1 - e^{-y^2}$) and decreases with distance from the Earth (e^x). The first term of B_x gives the rotation of the current sheet. The current sheet is defined here as the surface which separates the field lines directed away and towards the Earth ,i.e. the turning points of the field lines in the current sheet where B_x changes sign. The rotation of the current sheet increases with distance from the Earth because the B_x term is only dependent on IMF B_y and dominates in the far tail where the magnetospheric field is very weak. The second term is necessary to make the added magnetic field divergence free. It is small compared to the first term. We chose the following coefficients: $b_1 = 8R_E$, $b_2 = 20R_E$, $b_3 = 20R_E$, $c1 = 1.3$, $c2 = 0.7$ and $c_3 = 0.04R_E^{-1}$. The coefficient b_3 is equal to the corresponding coefficient in the T89 model. The other coefficients are chosen so that the IMF B_y penetration and the current sheet rotation

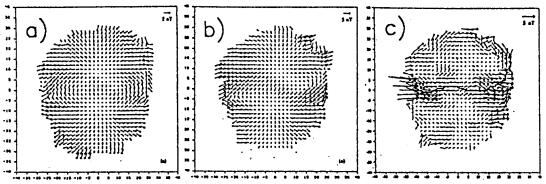

Figure 2. Figures 2a, 2c and 2e from Kaymaz et al. [1994]. They show $-25R_E > x > -40R_E$ average vector plots from IMP 8 data a) for all IMF directions, b) for IMF $B_y > 0$ and c) the difference vector field with overlayed current sheet.

in the mid-tail are of approximately the same value as in the study of Kaymaz et al.

Figure 2 gives the cross section vector plots of Kaymaz et al. for average IMF conditions, for $B_{y,IMF} > |B_{z,IMF}| > 0$ and the difference vector field between the first two vector plots. The corresponding vector plots of our modelling are shown in Figure 3. There, the unmodified T89 model, the modified T89 model for positive IMF B_y and the superposed magnetic field are given.

The mapping from the tail plasma sheet to the ionosphere gives qualitatively the form of the auroral oval. The far tail plasma sheet region maps to the poleward auroral oval boundary, which is assumed to be close to the boundary between open and closed field lines. Figure 4 shows the ionospheric footprints of field lines coming from the tail neutral sheet. Except for the flanks, the field line mapping gives quite a reasonable auroral oval distribution.

The Effects of the Added Magnetic Field on the Tail

The By component causes a twisting of the magnetic field lines. For IMF $B_y > 0$ the added B_y field causes a displacement of the open field lines in the direction of the negative (positive) GSM y-axis for the northern (southern) hemisphere and IMF $B_y > 0$. The closed field lines are tilted in this case as shown in Figure 6a. The effect is reversed for negative IMF B_y.

The B_X component is related to the rotation of the tail plasma sheet. Figure 5 gives the isocontours of B^2. The rotation of the isocontours for

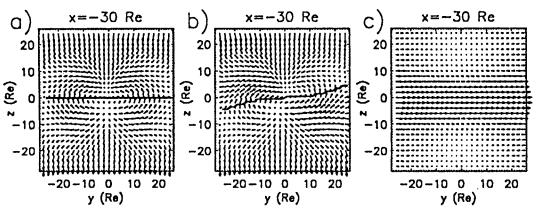

Figure 3. Tail cross section and current sheet of the T89 model (tilt=0, $K_p = 0$ at $x = -30R_E$ a) for $B_y = 0$, b) for $B_y = 5$nT and c) the added B field.

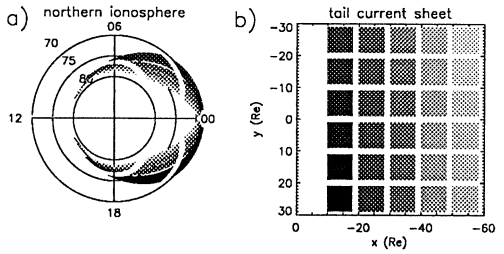

Figure 4. Current sheet mapping to the ionosphere with the unmodified T89 model. a) The areas at the tail current sheet which are used for the field line mapping. b) The projection from the current sheet to the ionosphere.

non-zero IMF B_y is related to the current sheet rotation. Unlike the lobes, the plasma sheet is characterized by low magnetic pressure ($B^2/2\mu_0$) and comparatively high plasma pressure. The isocontour line dashed in Figure 5 can be taken to represent qualitatively the boundary of the plasma sheet. The Figure shows that the plasma sheet rotates because of the current sheet rotation due to the B_x term. Because of the nonuniformity of the rotation, the plasma sheet reaches high latitudes at the dusk and dawn flanks for the northern and southern hemispheres, respectively.

The Effects of the Added Magnetic Field in the Ionosphere

The By component results in a rotation of the auroral oval. Figure 6a shows a schematic explaining the rotation of the auroral oval. Because of the tilting of the closed field lines for $B_y > 0$ their ionospheric connection points are displaced towards dusk (dawn) in the northern (southern) ionospheres. The rotation of the oval is strongest at high latitudes. The high latitude field lines come from the far tail regions and are therefore influenced most strongly by IMF B_y.

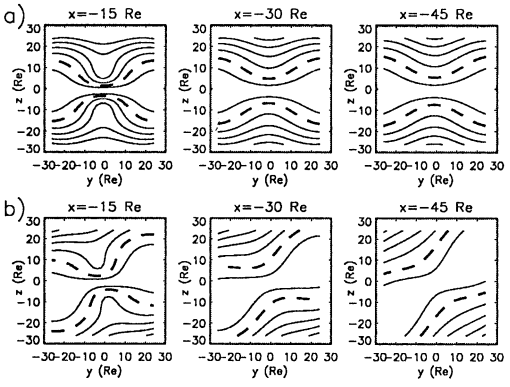

Figure 5. B^2 isocontours (arbitrary units) at different tail cross sections a) for the undisturbed T89 model and b) for the modified T89 model. The dashed line gives an approxiamte plasma sheet boundary.

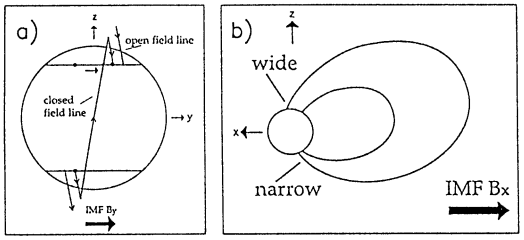

Figure 6. a) A schematic explaining the twisting of the field lines and rotation of the auroral oval under IMF B_y influence. b) A schematic illustrating the increase (decrease) of the separation between field line connection points in the southern (northern) ionosphere for superposed negative B_x on the tail.

The Bx component causes a broadening (narrowing) of the oval at dusk (dawn) and a bulge near midnight. The addition of a negative B_x component on a dipole field results in an increase (decrease) of the latitudinal separation of field line footprints in the northern (southern) ionosphere. This is illustrated in Figure 6b. A positive B_x gives the opposite result. As in our model the superposed B_x component is negative on the duskside and positive on the dawnside of the magnetotail (for $B_y > 0$), the dusk- and dawnward current sheet maps to wider and narrower areas in the northern hemisphere, respectively.

Final results for mapping to the ionosphere under IMF By influence. Figure 7 shows the re-

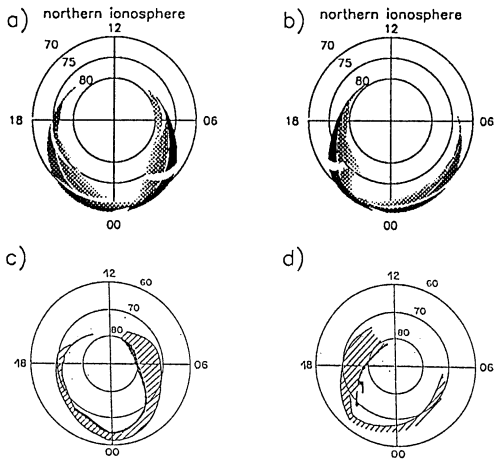

Figure 7. Comparison between Viking satellite images and the model results for the auroral oval. a) Model auroral oval for weak, negative IMF B_y and b) for strong, positive IMF B_y. c) Satellite image for weak, negative IMF B_y and d) for strong, positive IMF B_y. The satellite pictures are from Jankowska et al. [1990], their Figures 3a and 4a.

sulting ionospheric pattern of field lines coming from the tail current sheet under weak (3.5nT) and strong (7.0nT) IMF B_y. All the expected asymmetries of the auroral oval occur: narrowing (broadening) of the morning (evening) sector and rotation of the entire oval, a local bulge near midnight and displacement of the poleward oval boundary towards higher and lower latitudes at dusk and dawn, respectively. The comparison with satellite images for non-zero IMF, like the Viking images in Figure 7 shows a good qualitative correspondence. Although not shown in this paper the field line mapping gives qualitatively the same results even with other coefficients. The sensitivity of the results to the choice of the coefficients is discussed in detail by *Kullen* [1996].

Conclusions

(i) The good agreement of the model results with satellite data leads us to believe that the quantitative expressions chosen for the perturbation field describe the real conditions reasonably well. This allows us to draw physical conclusions from the field line mapping results.
(ii) Consideration of IMF B_y effects is of importance when discussing topological connections between the ionosphere and the magnetotail.
(iii) The mapping from the tail to the ionosphere for a non-zero IMF B_y reproduces all of the expected changes of the auroral oval. Thus, asymmetries in the tail and in the ionosphere are closely related.
(iv) The plasma sheet rotates with the current sheet and gets broader at the flanks, reaching several R_E north and south of the equatorial plane near dusk and dawn, respectively.

Acknowledgments. We are grateful to Carl-Gunne Fälthammar, Göran Marklund and Tomas Karlsson for valuable discussions. This work was carried out while Anita Kullen, a student of the University of Karlsruhe was doing her degree thesis project at the Alfvén Laboratory in Stockholm. She gratefully acknowledges the hospitality and support of the Alfvén Laboratory and the support of her German supervisor Edith Borie. This work was funded in part by the Swedish National Space Board.

References

Cowley, S.W.H., Magnetospheric asymmetries associated with the y-component of the IMF, *Planet.Space Sci., 29*, 79, 1981.

Cowley, S.W.H. and Hughes, W.J., Observation of an IMF sector effect in the Y magnetic field component at geostationary orbit, *Planet.Space Sci., 31*, 73, 1983.

Elphinstone, R.D., J.S. Jankowska, J.S. Murphree, and L.L. Cogger, The configuration of the auroral distribution for interplanetary magnetic field Bz northward. 1. IMF Bx and By dependencies as observed by the Viking satellite, *J.Geophys.Res., 95*, 5791, 1990.

Fairfield, D.H., On the average configuration of the geomagnetic tail, *J.Geophys.Res., 84*, 1950, 1979.

Fairfield, D.H., An evaluation of the Tsyganenko magnetic field model, *J.Geophys.Res., 96*, 1481, 1991.

Hammond C.M., M.G. Kivelson, and R.J. Walker, Planetary magnetotails: magnetic configuration and nonthermal plasma *Ph.D.thesis*, Univ.of Calif. LA, 1992.

Jankowska, K., R.D. Elphinstone, J.S. Murphree, L.L. Cogger, D. Hearn and G. Marklund, The configuration of the auroral distribution for interplanetary magnetic field Bz northward. 2. Ionospheric convection consistent with Viking observations, *J.Geophys.Res., 95*, 5805, 1990.

Kaufmann, R.L., D.J. Larson, P. Beidl, and Ch. Lu, Mapping and energization in the magnetotail. 1. magnetospheric boundaries, *J.Geophys.Res., 98*, 9307, 1993.

Kaymaz, Z., G.L. Siscoe, J.G. Luhmann, R.P. Lepping and Ch.T. Russell, Interplanetary magnetic field control of magnetotail magnetic field geometry: IMP 8 observations, *J.Geophys.Res., 99*, 11:113, 1994.

Kullen, A., The influence of the y component of the interplanetary magnetic field on the structure of the magnetotail and the auroral oval , *Degree Thesis*, KTH Stockholm, 1996.

Lassen, K. and C. Danielsen, Quiet time pattern of auroral arcs for different directions of the interplanetary magnetic field in the yz plane, *J.Geophys.Res., 83*, 5277, 1978.

Lui, A.T.Y., Solar wind influence on magnetotail configuration and dynamics, *Solar wind magnetosphere coupling*, Ed. Y.Kamide and J.A. Slavin, 671, 1986.

Meng, C.-I. and K.A. Anderson, Magnetic field configuration in the magnetotail near 60 Re, *J.Geophys.Res., 79*, 5143, 1974.

Moses, J.J. and N.U. Crooker, High-latitude convection on open and closed field lines for large IMF By, *J.Geophys.Res., 90*, 11:078, 1985.

Ohtani, S. and S. Kokubun, Magnetic properties of the high-latitude tail boundary: draping of magnetosheath field lines and tail-aligned current, *J.Geophys.Res., 96*, 9521, 1991.

Pudovkin, M.I., A model of the dayside magnetosphere and breakups in the cusp region, *Proceedings of the Cluster Workshop*, Eur.Space Agency Spec. Publ., 330, 1991.

Pudovkin, M.I., A model of the dayside magnetosphere and breakups in the cusp region, *Proceedings of the Cluster Workshop*, Eur.Space Agency Spec. Publ., 330, 1991.

Sergeev, V.A., Penetration of the By component of the IMF into the tail of the magnetosphere, *Geomagn. Aeronomy, 27*, 528, 1987.

Sibeck, D.G., J.A. Slavin, E.J. Smith, B.T. Tsurutani, and R.P. Lepping, Twisting of the geomagnetic tail, *Solar Wind-Magnetosphere Coupling*, Ed. Y. Kamide and L.A. Slavin, 731, 1986.

Siscoe, G.L. and E. Sanchez, An MHD model of the complete open magnetotail boundary, *J.Geophys.Res., 92*, 7405, 1987.

Stern, D.P. and N.A. Tsyganenko, Uses and limitations of the Tsyganenko magnetic field models, *EOS,Transactions, AGU, 73*, 489, 1992.

Tsyganenko, N.A., A magnetospheric magnetic field model with a warped tail current sheet, *Planet.Space Sci., 37*, 5, 1989.

A. Kullen and L. Blomberg, Division of Plasma Physics, Alfvén Laboratory, Royal Institute of Technology, S-100 44 Stockholm, Sweden. (e-mail: kullen@plasma.kth.se, blomberg@plasma.kth.se)

(received June 5, 1996;
revised July 11, 1996; accepted July 11, 1996.)

Paper 2

GEOPHYSICAL RESEARCH LETTERS, VOL. 27, NO. 1, PAGES 73-76, JANUARY 1, 2000

The Connection Between Transpolar Arcs and Magnetotail Rotation

A. Kullen

Division of Plasma Physics, Alfvén Laboratory, Royal Institute of Technology, Stockholm, Sweden

Abstract. Recent observations show that the evolution of transpolar arcs (TPA's) are often associated with a sign change of the dawn-dusk component of the interplanetary magnetic field (IMF). It is known that a nonzero IMF B_y causes a twist of the tail plasma sheet. In this study it is assumed that a sign change of IMF B_y causes the magnetotail to rotate until the entire tail is twisted in the opposite direction. To examine a possible connection between TPA's and tail rotation the Tsyganenko 1989 model is modified such that the near-Earth tail and the far tail are twisted in opposite directions. Mapping from the tail current sheet to the ionosphere shows a separated region of closed field lines that extends into the polar cap. This separated part may be interpreted as the mapped region of a TPA.

Introduction

Since the first global observation of transpolar arcs (TPA's) [*Frank et al.*, 1982] there have been many studies on this subject. While the source region of small-scale polar arcs remains unclear [e.g., Bonnell et al., 1999] TPA's are commonly believed to map to the tail plasma sheet or its boundary layer [e.g., *Frank and Craven*, 1988]. Different topologies of the magnetotail have been proposed for TPA events. The plasma sheet has been suggested to be bifurcated [*Frank and Craven*, 1988], to have filamentary extensions into the lobes [*Huang et al.*, 1987] or to be asymmetrically expanded [*Meng*, 1981]. Alternatively, a significant 'distortion' in the mapping along B-field lines has been suggested [*Blomberg and Marklund*, 1993].

Observations indicate that the evolution of a TPA depends strongly on the direction of the IMF. Polar arcs are predominantly a northward IMF phenomenon [e.g., *Valladares et al.*, 1994]. In the statistical study by *Valladares et al.* [1994] it is shown that the dawn-dusk motion of polar arcs is strongly dependent on the sign of IMF B_y. This result is in agreement with observations which report that TPA's move in the direction of IMF B_y [e.g., *Cumnock et al.*, 1997]. There is some evidence that TPA's occur simultaneously in the northern and southern polar cap but with opposite dawn-dusk motion [*Craven et al.*, 1991]. Different IMF initial conditions have been suggested to generate TPA's [*Chang et al.*, 1998]. In the model of *Kan and Burke* [1985] that describes TPA's which evolve from midnight to noon, a purely northward IMF is required. TPA's splitting from the dawnside or duskside of the oval have been observed to occur after a sign change of IMF B_y during northward IMF [*Cumnock et al.*, 1997] or, alternatively, a southward turning of an initially northward IMF during changing IMF B_y [*Newell and Meng*, 1995].

In this paper the IMF configuration proposed by *Cumnock et al.* [1997] is addressed. Based on their results, a different topology of the magnetotail is suggested which may help to explain the evolution of TPA's appearing after a sign change of IMF B_y.

Observations

The latest results by Cumnock [private communication] are that a sign change of IMF B_y during northward IMF often triggers the evolution of a TPA (Figure 1) which lasts for several hours. The evolution of the TPA can be described in four steps: (1) A dawnward (duskward) IMF is connected to a dawnward (duskward) expansion of the auroral oval. (2) A sign change of IMF B_y causes a TPA to separate from the side of the oval which is expanded poleward. (3) In case the IMF B_y remains constant the TPA moves poleward. (4) Often, the TPA fades away after having crossed the noon-midnight line. In the final configuration, the opposite side of the oval is expanded poleward.

It has been shown that IMF B_y partially penetrates the magnetotail and causes a twist of the entire tail [e.g., *Kaymaz et al.*, 1994]. The tail is positively twisted (counter-clockwise in the yz-plane looking from the Earth downtail) for positive IMF B_y and negatively twisted for negative IMF B_y. Positive and negative IMF B_y have qualitatively similar but anti-symmetrical effects on the magnetotail topology. Thus, the difference of type and occurrence frequency of polar arcs for dawnward and duskward IMF [*Gussenhoven*, 1982] perhaps does not have its cause in the topology of the tail. The model presented in this study produces symmetric mapping results for positive and negative IMF B_y as it shows only those ionospheric regions which map to the tail plasma sheet. For simplicity only the IMF sign change from dawnward to duskward is considered in this work but the result is also valid for the opposite case.

Paper number 1999GL010675.
0094-8276/00/1999GL010675$05.00

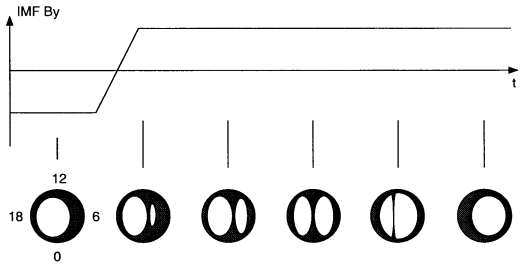

Figure 1. TPA evolution for a sign change of IMF B_y.

Assumptions

This work is based on the assumption that a sign change of IMF B_y affects the magnetotail to change its twist first in the near-Earth region and then farther down the tail (Figure 2). The process can be described in four steps: (1) For negative IMF B_y the tail is negatively twisted. (2) A sign change of IMF B_y from negative to positive influences first the near-Earth tail. The near-Earth tail rotates to a positive twist whereas the far tail remains negatively twisted. (3) With time the rotation of the tail propagates tailward. The region of the tail having a positive twist thus expands. (4) Finally the entire tail becomes positively twisted. The change of the tail topology during a sign change of IMF B_y is assumed to correspond to the evolution of a TPA in the ionosphere (above described). The TPA persists as long as the tail twist changes polarity. The tailward propagation of the twist reversal region is supposed to be connected to a dawn/dusk movement of the TPA. As the tail rotation is completed the TPA should fade away.

The model

To examine the connection between TPA's and tail rotation the *Tsyganenko* [1989] model (T89) is modified such that the near-Earth tail is twisted positively whereas the far tail is twisted negatively representing an IMF B_y sign change from negative to positive. An extension of the T89 model to include the effects of constant IMF B_y has already been done by *Kullen and Blomberg* [1996]. They demonstrated that the poleward expansion of the auroal oval is connected to a twist of the magnetotail by adding nonuniform B field components (B_x^*, B_y^*, B_z^*) to the T89 model B-field to represent the penetration B-field and the twist of the plasma sheet, respectively:

$$B_x^* = B_y^{\mathrm{IMF}}[-c_3 y - \tfrac{2c_2 b_3}{b_2^2} y e^{-(\frac{y}{b_2})^2} e^{\frac{x}{b_3}}]$$
$$B_y^* = B_y^{\mathrm{IMF}}[c_1 e^{-(\frac{z}{b_1})^2} + c_2(1 - e^{-(\frac{y}{b_2})^2})]e^{\frac{x}{b_3}}$$
$$B_z^* = 0$$

The coefficients $b_1 = 8\mathrm{R_E}$, $b_2 = 20\mathrm{R_E}$, $b_3 = 20\mathrm{R_E}$, $c1 = 1.3$, $c2 = 0.7$ and $c_3 = 0.04\mathrm{R_E^{-1}}$. were chosen to fit the tail twist and the B_y penetration field of the model to the results of a data study by *Kaymaz et al.* [1994]. For further details see *Kullen and Blomberg* [1996]. To get opposite twists of the near-Earth tail and the far tail the added B-field components have to change polarity at some point x_0 in the tail. *Akasofu and Roederer* [1983] showed that an abrupt change of IMF B_y would lead to a splitting of the polar cap into two regions. Since they modeled only a uniform B_y penetration field and not a tail twist, they needed an unrealistically strong IMF B_y. Including a tail twist in the model of this study excludes an abrupt change of the superimposed B-field. The tail would be twisted differently on both sides of the discontinuity sheet (div $\mathbf{B} \neq 0$). Thus, the added B-field components are changed smoothly from positive to negative over a given area, Δx. We represent this smooth change by a tanh function:

$$B_x' = B_x^* \tanh(\tfrac{2(x-x_0)}{\Delta x})$$
$$B_y' = B_y^* \tanh(\tfrac{2(x-x_0)}{\Delta x}) + \tfrac{2}{\Delta x}[1-\tanh^2(\tfrac{2(x-x_0)}{\Delta x})]\times$$
$$B_y^{\mathrm{IMF}}[\tfrac{c_3}{2} y^2 - c_2 b_3 e^{-(\frac{y}{b_2})^2} e^{\frac{x}{b_3}}]$$
$$B_z' = 0$$

where x_0 represents the center of the area over which the sign change takes place and Δx the width of it. Since B_x now has a second x-dependence an additional term has to be added in the yz-plane to obtain a divergence free B-field. Independent of the choice of this extra term a splitting of the oval occurs. The splitting is only significant for reasonably low IMF B_y values if the B_y component dominates. Hence, the extra term has been assumed to lie in the y-direction (last term in B_y').

Figure 3 shows plots of the ionospheric regions which are connected to the tail plasma sheet, for different model parameters. The plots are produced by mapping B-field lines from the tail current sheet (defined here as the surface where B_x changes sign) back to Earth. The poleward boundary of this region in the ionosphere represents the approximate location of the poleward boundary of the auroral oval. In order to simulate the conditions of a quiet magnetosphere with a plane neutral sheet, the K_p index and the dipole tilt are set to zero in the model. Figure 3a (right plot) shows the tail current sheet from $-10\mathrm{R_E}$ to $-60\mathrm{R_E}$ (the T89 model is not valid farther downtail) which is color coded to help identify the corresponding areas in the ionosphere. Near the current sheet

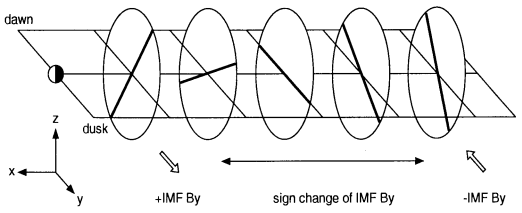

Figure 2. Tail rotation for a sign change of IMF B_y.

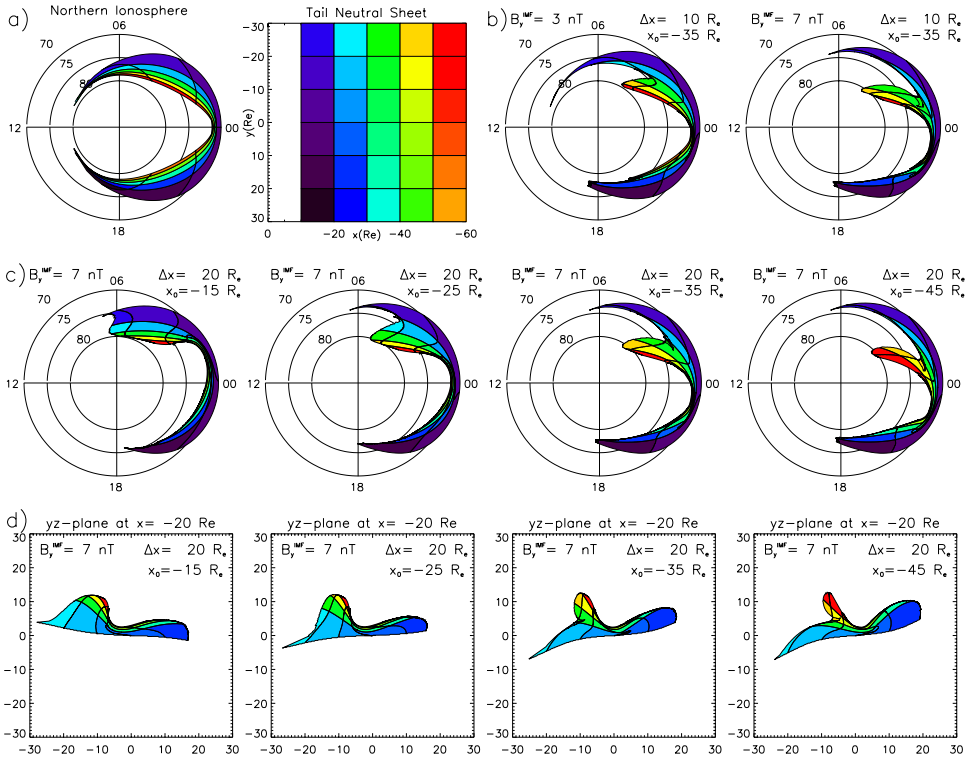

Figure 3. Field line mapping from the tail current sheet (B_x sign reversal) to the ionosphere for a) the unmodified T89 model (IMF $B_y = 0$), b) different strengths of IMF B_y for a narrow twist reversal region Δx, c) the twist reversal region being located farther downtail at each plot with a medium Δx and d) field line mapping from $x = -20\mathrm{R_E}$ and downtail to the tail cross section at $x = -20\mathrm{R_E}$ for those field lines which map to the northern ionosphere (the cross section plots correspond to the ionosphere plots of Figure 3c).

flanks, only parts of the colored areas belong to the magnetosphere and map to the ionosphere. In Figure 3a (left plot) the mapping to the ionosphere for the unmodified T89 model is shown. Since the mapping is only done from the tail at $x = -10\mathrm{R_E}$ and farther downtail, the dayside part of the oval does not appear in the mapping plots. Also, the far-tail flanks and the far-tail center map to too low latitudes in the ionosphere. The T89 model does not contain a defined magnetopause and the added extra terms in the modified version are not limited in the y or z direction. Thus the model is realistic only inside the magnetosphere.

Results

The mapping plots of Figure 3b, 3c and 3d are obtained for opposite twists of the near-Earth tail and the far tail. All ionospheric plots show a clear splitting of the polewardly expanded oval region. The flank boundaries have been moved 1.5 R_E into the tail to minimize distortions where the TPA connects to the oval. This has a neglectable effect on the location of the open-closed field line boundary. The region of closed field lines which is separated from the main oval may be interpreted as the mapped source region for a TPA, however, the TPA does not necessarily extend over the entire separated part. The topological connection to the plasma sheet is not a sufficient condition for aurora to occur. The main limitation of this model is that the TPA does not stretch over the entire polar cap. This is caused by the mapping from the current sheet for a tailward limited model. Mapping from a surface parallel but above the current sheet produces a deformed 'TPA' which stretches nearly to the dayside oval. Since it is difficult to define a plasma sheet boundary in this model, the current sheet mapping gives more reliable results.

In Figure 3b mappings for different IMF B_y values are plotted. A comparison of these plots with the third plot of Figure 3c shows the influence of the input parameters IMF B_y and Δx on the mapping results. Both a small Δx and a strong IMF B_y lead to a clearer splitting of the TPA from the oval. While strong IMF B_y is connected

to a more polewardly located TPA, the influence of Δx on the location of the TPA is negligible. Assuming that Δx is dependent on the time period over which IMF B_y changes sign, the model results indicate that the duration of a TPA event is not influenced by the magnitude of $\partial B_y^{\mathrm{IMF}}/\partial_t$.

In each plot of Figure 3c the region over which the twist reversal takes place is located farther downtail. These mapping plots demonstrate that the separation from the oval and the poleward motion of the TPA can be connected to a tail rotation propagating tailward. The TPA should disappear when the rotation of the tail is completed and the entire tail has returned to the topology typical for a uniform nonzero IMF B_y. This is implicated by the model. The TPA gets thinner and shorter when the twist reversal region is located farther downtail. The tailward propagation of the twist reversal region is assumed to be caused by the tailward progression of the IMF B_y sign change. Since TPA's can last up to several hours either the magnetotail would have to respond extremely slowly to a sign change of IMF B_y or the plasma sheet regions from even the very distant tail would contribute to the TPA.

To get a better understanding of how the splitting of the oval is connected to the tail topology, Figure 3d shows mapping plots of a tail cross section at $x = -20\mathrm{R_E}$ for different locations of x_0. The plots correspond to the ionospheric mapping plots of Figure 3c and show those field lines which map from the current sheet to the northern hemisphere. The splitting of the dawnside oval is connected to a 'bifurcation' of the region of current sheet field lines. The current sheet field lines from the far tail map to much higher latitudes than field lines from the near-Earth tail because the near-Earth and far-tail plasma sheet regions are oppositely twisted.

Some additional features can be found from studying the mapping plots of Figure 3 in more detail. The regions between the TPA and the dawnside and duskside of the auroral oval lie on open field lines. Field lines originating Earthward of x_0 map to the auroral oval whereas field lines originating tailward of x_0 map to the TPA. Since the tail is symmetric about the current sheet, TPA's occur in the model simultaneously in the northern and southern hemisphere but on opposite sides of the noon-midnight line.

Although this model gives only qualitative results it shows that opposing tail twists are likely to play an important role in the development of those TPA's which occur after a sign change of IMF B_y.

Acknowledgments. I would like to thank J. Cumnock for detailed discussions of TPA's.

References

Akasofu, S.-I., and M. Roederer, Polar cap arcs and the open regions, *Planet. Space Sci., 31*, 193, 1983.

Blomberg, L.G., and G. T. Marklund, High-latitude electrodynamics and aurorae during northward IMF, *Auroral Plasma Dynamics, Geophys. Monogr. Ser., 80*, 55, 1993.

Bonnell, J. et al., Observations of polar cap arcs on FAST, *J. Geophys. Res., 104*, 12:669, 1999.

Chang, S.-W. et al., A comparison of a model for the theta aurora with observations from Polar, Wind and SuperDARN, *J. Geophys. Res., 103*, 17:367, 1998.

Craven, J.D. et al., Simultaneous optical observations of transpolar arcs in the two polar caps, *Geophys.Res.Lett., 18*, 2297, 1991.

Cumnock, J.A. et al., Evolution of the global aurora during positive IMF Bz and varying IMF By conditions, *J. Geophys. Res., 102*, 17:489, 1997.

Frank, L.A. et al., Polar view of the Earth's aurora with dynamic explorer, *Geophys. Res. Lett., 9*, 1001, 1982.

Frank, L.A., and J.D. Craven, Imaging results from Dynamics Explorer 1, *Rev. Geophys., 26*, 249, 1988.

Gussenhoven, M.S., Extremely high latitude auroras, *J. Geophys. Res., 87*, 87, 2401, 1982.

Huang, C.Y. et al., Filamentary structures in the magnetotail lobes, *J. Geophys. Res., 92*, 2349, 1987.

Kan, J.R., and W.J.Burke, A theoretical model of polar cap auroral arcs, *J. Geophys. Res., 90*, 4171, 1985.

Kaymaz, Z. et al., Interplanetary magnetic field control of magnetotail magnetic field geometry: IMP 8 observations, *J. Geophys. Res., 99*, 11:113, 1994.

Kullen, A., and L.G. Blomberg, The influence of IMF By on the mapping between the Earth's magnetotail and its ionosphere, *Geophys. Res. Lett., 23*, 256, 1996.

Meng, C.-I., Polar cap arcs and the plasma sheet, *Geophys. Res. Lett., 8*, 273, 1981.

Newell, P.T., and C.-I. Meng, Creation of theta-auroras: The isolation of plasma sheet fragments in the polar cap, *Science, 270*, 1338, 1995.

Tsyganenko, N.A., A magnetospheric magnetic field model with a warped tail current sheet, *Planet. Space Sci., 37*, 5, 1989.

Valladares, C.E., H.C. Carlson Jr. and K. Fukui, Interplanetary magnetic field dependency of stable Sun-aligned polar cap arcs, *J. Geophys. Res., 99*, 6247, 1994.

A. Kullen, Division of Plasma Physics, Alfvén Laboratory, Royal Institute of Technology, S-100 44 Stockholm, Sweden. (e-mail: kullen@plasma.kth.se)

(Received April 6, 1999; revised August 27, 1999; accepted September 13, 1999.)

Paper 3

JOURNAL OF GEOPHYSICAL RESEARCH, VOL. 107, NO. A11, 1362, doi:10.1029/2002JA009245, 2002

Solar wind dependence of the occurrence and motion of polar auroral arcs: A statistical study

A. Kullen
Royal Institute of Technology, Alfvén Laboratory, Stockholm, Sweden

M. Brittnacher
Department of Earth and Space Sciences, University of Washington, Seattle, Washington, USA

J. A. Cumnock[1] and L. G. Blomberg
Royal Institute of Technology, Alfvén Laboratory, Stockholm, Sweden

Received 4 January 2002; revised 15 March 2002; accepted 25 March 2002; published 14 November 2002.

[1] Polar UV images from a 3-month period in winter 1998–1999 are used for a statistical study of polar arcs. The study covers all auroral arcs that are located poleward of the northern auroral oval, and which are detectable by the UV imager. The arcs are examined with respect to their spatial and temporal behavior as well as to a possible connection to solar wind parameters using ACE satellite data. It is found that the majority of polar arcs appear during northward IMF, strong IMF magnitude, and high solar wind speed. A modified Akasofu-Perreault epsilon parameter with a cosine function instead of a sine function ($vB^2 \cos^4(\theta/2)(l_0^2/\mu_0)$) combines these results. It correlates well with the occurrence frequency of polar arcs for long timescales. The location of polar arcs is strongly dependent on the sign of the IMF B_y component. Static polar arcs occur in the Northern Hemisphere on the dawn (dusk) side of the oval for negative (positive) IMF B_y, whereas poleward-moving arcs separate from the opposite side of the oval, and then move in the direction of IMF B_y. All polar arcs are sorted into five different categories according to their spatial structure and evolution: oval-aligned, bending, moving, midnight, and multiple arcs. Each polar arc type occurs for a characteristic combination of solar wind parameters. IMF clock angle changes seem to have a strong influence on what type of arc occurs. Oval-aligned arcs appear mainly during steady IMF, bending arcs after an IMF B_z sign change, and moving arcs after an IMF B_y sign change. For the rare midnight and multiple arc events, no characteristic IMF clock angle dependence has been found. The different types of clear polar arcs are discussed in the context of existing observational studies and transpolar arc models. *INDEX TERMS:* 2475 Ionosphere: Polar cap ionosphere; 2736 Magnetospheric Physics: Magnetosphere/ionosphere interactions; 2784 Magnetospheric Physics: Solar wind/magnetosphere interactions; 2776 Magnetospheric Physics: Polar cap phenomena; *KEYWORDS:* Polar arc, transpolar arc, solar wind, IMF, transpolar arc model

Citation: Kullen, A., M. Brittnacher, J. A. Cumnock, and L. G. Blomberg, Solar wind dependence of the occurrence and motion of polar auroral arcs: A statistical study, *J. Geophys. Res.*, *107*(A11), 1362, doi:10.1029/2002JA009245, 2002.

1. Introduction

1.1. Definition of Polar Arcs

[2] Polar arcs are defined as high-latitude auroral arcs located poleward of the main auroral oval. There are several types of polar arcs and differences are, for example, found in their spatial extent and in their magnetospheric source regions. Small-scale Sun-aligned arcs occur at high latitudes and have a length of only a few hundred kilometers. While several authors propose that small-scale Sun-aligned arcs occur on open field lines [e.g., *Gussenhoven and Mullen*, 1989, and references therein] others claim that their source regions remain unclear [*Bonnell et al.*, 1999].

[3] Large-scale polar arcs are several hundred kilometers wide and extend from about 1000 km to the entire diameter of the polar cap in length. A multitude of different large-scale polar arc formations have been found and various names have been used to describe these. Large-scale arcs which stretch over the entire polar cap connecting the nightside with the dayside oval are called transpolar arcs [*Frank et al.*, 1982, 1986]. They have similar particle characteristics to those along the main oval, which suggests an origin in the plasma sheet or plasma sheet boundary layer

[1]Also at Center for Space Sciences, University of Texas, Richardson, Texas, USA.

0148-0227/02/2002JA009245$09.00

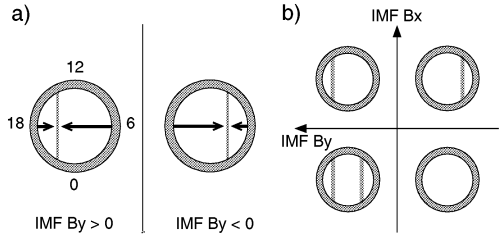

Figure 1. Statistical results of (a) IMF B_y dependent motion of small-scale Sun-aligned arcs by *Valladares et al.* [1994] and (b) IMF B_y and B_x dependent location of oval-aligned arcs by *Elphinstone et al.* [1990].

[e.g., *Meng*, 1981; *Peterson and Shelley*, 1984; *Frank et al.*, 1986; *Frank and Craven*, 1988; *Huang et al.*, 1987, 1989]. Occasionally large-scale arcs can be hook-shaped with the arc connected to the auroral oval only in the midnight sector [*Ismail and Meng*, 1982; *Murphree et al.*, 1982] or near noon [*Gusev and Troshichev*, 1986]. Static transpolar arcs near the dawnside or duskside auroral oval are sometimes referred to as oval-aligned arcs [*Murphree and Cogger*, 1981]. The so-called horse-collar aurora describes oval-aligned arcs at the dawn and dusk poleward edges of an expanded oval [*Hones et al.*, 1989]. A few cases have been reported where a transpolar arc does not separate from the dawnside or duskside oval but grows from the nightside oval. *Craven et al.* [1986] presented an example where a single arc starts at midnight and stretches toward noon. According to *McEwen and Zhang* [2000], such events are rare. *Brittnacher et al.* [1999] found a case during a major magnetic storm where multiple large-scale polar arcs fill the whole polar cap. One of the arcs develops clearly from the nightside oval. As pointed out in the review paper by *Zhu et al.* [1997] it is not yet clear whether different polar arcs represent the same auroral phenomena (but described differently depending on the means of observations) or whether these are fundamentally different types of polar arcs.

1.2. IMF Control of Polar Arcs

[4] The occurrence of polar arcs is strongly controlled by the interplanetary magnetic field (IMF). From numerous studies it is known that polar arcs are a predominantly northward IMF phenomenon, which includes small-scale Sun-aligned arcs [e.g., *Lassen and Danielsen*, 1978; *Gussenhoven*, 1982; *Ismail and Meng*, 1982] and transpolar arcs [e.g., *Frank et al.*, 1986]. The existence of transpolar arcs which appear during southward IMF has been explained by *Frank and Craven* [1988] as arcs which have formed during northward IMF conditions but persist for some time following a change to southward IMF (corresponding to the time span necessary to reconfigure the tail). In a large statistical study about small-scale Sun-aligned arcs based on images from ground-based all-sky cameras (ASIP) in the Northern Hemisphere *Valladares et al.* [1994] came to the same conclusion.

[5] Another result by *Valladares et al.* [1994] refers to the arc location in the polar cap. Small-scale Sun-aligned arcs occur preferably on the dawn side, less often on the dusk side, which confirms earlier results for both the northern [*Ismail et al.*, 1977; *Gussenhoven*, 1982] and the southern polar cap [*Rairden and Mende*, 1989]. Whether this preference is true for large-scale polar arcs remains to be shown.

[6] The IMF B_y component controls the motion of polar arcs. The statistical study of *Valladares et al.* [1994] shows the correlation between polar arc motion and IMF B_y component in the Northern Hemisphere. They found that the dawn-dusk component of the IMF causes a motion of most small-scale Sun-aligned arcs in the direction of IMF B_y. However, the arcs near the side of the auroral oval which lies in the direction of IMF B_y move slightly in the opposite direction (Figure 1a). The motion of transpolar arcs is controlled by IMF B_y in the same way as the small-scale Sun-aligned arcs. *Frank et al.* [1985] reported a dusk to dawn moving transpolar arc for dawnward IMF B_y and, conversely, *Huang et al.* [1989] reported a duskward moving transpolar arc for duskward directed IMF B_y. The observational study by *Craven et al.* [1991] of two simultaneously appearing transpolar arcs in both hemispheres indicates that the motion of transpolar arcs in the southern hemisphere is in the opposite direction. Probably, even small-scale Sun-aligned arcs of the southern polar cap move in the opposite direction, but this remains to be shown. It is expected from the results described above that oval-aligned arcs in the Northern Hemisphere are located on the side of the oval to which IMF B_y is pointing. *Elphinstone et al.* [1990] though, found a different correlation between (mainly oval-aligned) large-scale polar arcs and IMF. In their study of polar cap size and location during northward IMF based on VIKING images of the Northern Hemisphere the location of polar arcs are related to 1-hour averaged IMF B_y and B_x components. They found that duskside arcs occur for duskward IMF B_y only, independent of IMF B_x but that dawnside arcs occur for B_y and B_x having opposite signs. This means, dawnside oval-aligned arcs occur even for duskward IMF B_y (Figure 1b).

[7] The sign of the IMF B_x component may influence the occurrence probability of polar arcs. *Lassen and Danielsen* [1978] reported that small-scale Sun-aligned arcs occur more frequently during periods of negative IMF B_x in the Northern Hemisphere. In the Southern Hemisphere the opposite sign of IMF B_x seems to be favorable for the occurrence of auroral activity in the polar cap. A statistical study of field-aligned currents in the dayside polar cap of the southern hemisphere by *Iijima et al.* [1984] shows a strong correlation between the current densities and positive IMF B_x. These field-aligned currents inside the polar cap are referred to as NBZ (northward B_z) currents as they are shown to be a predominantly northward IMF phenomenon. The existence of strong NBZ currents is likely to be an indication of the appearance of polar arcs as polar arcs are always associated with field-aligned currents [e.g., *Zhu et al.*, 1997, and references therein].

[8] Several papers have reported an influence of IMF sign changes on the appearance of transpolar arcs. Both *Newell et al.* [1997] and *Chang et al.* [1998] presented observations of transpolar arcs which appear when an IMF B_z sign change takes place. In their studies, the motion of the transpolar arc is IMF B_y dependent but it is the rotation of the IMF to southward B_z that causes the transpolar arc to initially appear. In their observations, the IMF B_z southward

period lasts for at least 10 min which questions earlier results about polar arcs being a purely northward IMF phenomenon. A sign change of IMF B_y has been reported as another cause of transpolar arcs. *Cumnock et al.* [1997] and *Chang et al.* [1998] both show several events where a transpolar arc separates from one side of the oval after an IMF B_y sign change and moves poleward. In a recent paper by *Cumnock et al.* [2002] transpolar arcs are examined which appear for IMF B_y sign changes during purely northward IMF B_z. All those studies find that Northern Hemisphere transpolar arcs which are triggered by either an IMF B_y or an IMF B_z sign change separate from the side of the oval which is opposite to the IMF B_y direction.

1.3. Solar Wind–Magnetospheric Coupling and Polar Arcs

[9] As polar arcs are predominantly a northward IMF phenomenon they appear preferably during quiet geomagnetic times with low K_P and AE values [e.g., *Ismail et al.*, 1977]. The negative correlation between AE index and polar arc occurrence is confirmed in the statistical study of *Lassen and Danielsen* [1989]. They even show that for AE decreasing below 30 nT Sun-aligned polar arcs tend to increase in length, stretching across the polar cap. The coupling between AE index and solar wind parameters has been studied extensively and several coupling parameters have been proposed during the last 20 years such as the Akasofu-Perreault epsilon parameter ($vB^2 \sin^4(\theta/2)(l_0^2/\mu_0)$) [*Perreault and Akasofu*, 1978]. The good correlation between epsilon and the AE index on long timescales has been confirmed [e.g., *Akasofu*, 1980]. The current density of the region 1 current system seems to be correlated to this type of solar wind coupling parameter as well. *Iijima and Potemra* [1982] find the best correlation between region 1 current densities and solar wind parameters for a function similar to the epsilon parameter ($(B_y^2 + B_z^2)^{1/2} \sin(\frac{\theta}{2})$). The complementary parameter $((B_y^2 + B_z^2)^{1/2} \sin(\frac{\theta}{2}))$ which they denote as ϵ^* is shown to be strongly correlated to the NBZ current system on the dayside part of the polar cap [*Iijima et al.*, 1984]. ϵ^* is likely to also correlate to field-aligned currents associated with polar arcs.

1.4. Models of Transpolar Arcs

[10] If one were to trace the magnetic field lines from a transpolar arc into the magnetotail in a standard configuration of the magnetosphere with a butterfly shaped plasma sheet centered about the equatorial plane, the transpolar arc field lines would map into the lobes. This is, however, not supported by observations. As mentioned before, transpolar arcs have their origin in the plasma sheet or its boundary layer. Thus, the plasma sheet must have a different shape during the occurrence of transpolar arcs. Several different tail topologies have been proposed to explain the observations.

[11] *Frank et al.* [1982] suggested that the tail plasma sheet is bifurcated such that a north-south aligned plasma sheet bulge extends into the lobes. *Huang et al.* [1987, 1989] found observations that are consistent with filamentary extensions of the plasma sheet into the lobes rather than one large-scale bulge.

[12] Another model, first proposed by *Meng* [1981], interprets transpolar arcs occurring for nonzero IMF B_y as the poleward boundary of an expanded auroral oval. The poleward expansion of the oval corresponds to the thickening of the plasma sheet. This model requires a highly contracted polar cap and a dawn-dusk asymmetry or a twisting of the plasma sheet [*Makita et al.*, 1991]. The now well-known connection between a strong dawn-dusk IMF component and a twist of the entire magnetotail [e.g., *Kaymaz et al.*, 1994, and references therein] supports twisting of the plasma sheet, shown in Figure 2a, as a more probable alternative. The twisted tail plasma sheet causes the open/closed field line boundary in the northern ionosphere to extend poleward on the duskside (dawnside) of the oval for positive (negative) IMF B_y [*Cowley*, 1981; *Kullen and Blomberg*, 1996]. Assuming the poleward boundary of the auroral oval to roughly overlap with the boundary between open and closed field lines the northern auroral oval is expected to broaden at the duskside (dawnside) of the oval for positive (negative) IMF B_y. Polar arcs are expected to lie on the poleward boundary of the expanded side of the oval.

[13] MHD simulations show that an IMF B_y induced twisting of the tail plasma sheet is not equally strong for northward and southward IMF. Only for northward IMF large twists occur [e.g., *Walker et al.*, 1999]. A statistical study of *Owen et al.* [1995] of the structure of the distant magnetotail confirms the MHD results. If the plasma sheet twist plays a major role for the appearance of transpolar arcs, the observation of strong twists for northward IMF may explain why transpolar arcs occur predominantly during northward IMF. The simultaneous occurrence of transpolar arcs on opposite sides of the noon-midnight meridian in the Northern and Southern Hemisphere [*Gusev and Troshichev*, 1986; *Craven et al.*, 1991] is another indication of the influence of a symmetrically twisted tail around the Earth-Sun line on the location of transpolar arcs.

[14] *Kullen* [2000] developed a model which explains the occurrence and motion of transpolar arcs following an IMF B_y sign change with a rotation of the tail twist. The model is based on the assumption that an IMF B_y sign change causes the magnetotail to change the direction of its twist successively such that in an intermediate state the near-Earth tail and the distant tail are twisted in opposite directions. Such a topology leads to a bifurcation of closed field lines in the near-Earth tail which in this model is responsible for the occurrence of a transpolar arc. To demonstrate this, the T89 model [*Tsyganenko*, 1989] has been modified to model the assumed tail topology. Mapping from the model tail current sheet into the ionosphere shows a region of closed field lines stretching into the polar cap which may be interpreted as the location of a transpolar arc. Figure 2b is a schematic showing how a rotated plasma sheet twist forces the region of closed field lines to bifurcate in the near-Earth region. The bifurcated part of the closed field lines originates in the far tail from the flank of the plasma sheet which stretches to very high latitudes. Following these field lines earthward they map into the high lobes of the oppositely twisted near-Earth tail. The poleward motion of the arc is caused by the tail twist reversal propagating tailward such that the high-latitude flank from the far tail maps increasingly poleward. The model by *Kullen* [2000] differs from the "plasma sheet bifurcation" model in that the region of closed field lines is bifurcated but not the plasma sheet itself. Recent MHD

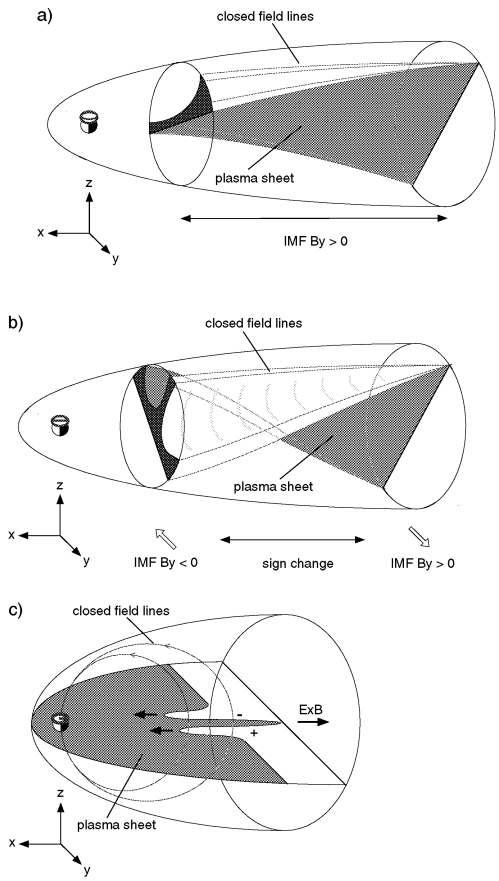

Figure 2. Schematic of different polar arc models illustrating the tail topology and closed field line region for the Northern Hemisphere. (a) Tail model for oval-aligned arcs [*Makita et al.*, 1991]: An IMF B_y induced tail twist causes the high-latitude flank to map to a stationary polar arc. (b) Tail model for moving arcs [*Kullen*, 2000]: A rotation of the tail twist caused by an IMF B_y sign change leads to a bifurcation of the closed field line region in the near-Earth tail. The bifurcated region maps to a transpolar arc which moves from one side of the oval to the other while the rotation of the tail twist propagates tailward. (c) Tail model for midnight arcs [*Rezhenov*, 1995]: An interchange instability causes a tailward moving plasma sheet tongue. This tongue maps to a polar arc which grows from midnight to noon.

simulations by *Slinker et al.* [2001] confirm the assumption that the IMF B_y sign change leads to a rotation of the tail twist. Ionospheric mapping plots show a bar of closed field lines moving over the entire polar cap.

[15] A different transpolar arc model has become established in recent years. *Newell et al.* [1997] proposed a model based on the idea of an abruptly moving dayside reconnection line after an IMF B_z flip. The sudden displacement of the merging line is assumed to lead to a new region of open field lines equatorward of the polar cap which, depending on the IMF B_y component, is located on the prenoon or postnoon side of the oval. *Chang et al.* [1998] refined this model and extended it to IMF B_y sign changes. These ideas are an extension of the theory explaining poleward moving auroral forms which split from the dayside auroral oval and move within some minutes poleward until they disappear. Poleward moving auroral forms begin to appear after the IMF turns southward and continue to occur transiently as long as a weakly southward IMF orientation is maintained. They are interpreted as the optical signature of transient reconnection pulses on the dayside magnetopause which are assumed to cause additional regions of new open flux on the front of the polar cap [*Sandholt et al.*, 1998; *Milan et al.*, 2000].

[16] *Rezhenov* [1995] proposed a model to explain large-scale polar arcs growing from the nightside toward the dayside with an interchange instability inside the magnetotail (Figure 2c). He suggests that such arcs occur during substorm recovery and strong northward IMF and/or high solar wind velocity leading to a short plasma sheet and a highly dipolarized tail magnetic field. According to his model strongly curved magnetic field lines cause a dusk to dawn current in the plasma sheet. A small distortion at the tailward plasma sheet boundary leads to a charge separation. An E × B drift causes the displacement to grow tailward, i.e., an interchange instability occurs. A tongue of plasma moves tailward which maps to a growing midnight arc.

1.5. The Goal of This Study

[17] This Polar UVI study focuses on the IMF control and possible IMF triggers of polar arcs with the goal of understanding the sometimes contradicting results that have been presented in the literature. One of the reasons for the confusion is that statistical results exist only for small-scale Sun-aligned arcs and not for large-scale polar arcs, a fact not always realized by authors when discussing polar arcs. Another reason may be that in most papers the history of the IMF before the arc occurrence is not considered. Here, a period of 3 months is examined in order to detect every polar arc which is visible on the UV images. With a limited spatial resolution and energy range, only bright large-scale arcs can be detected, and thus small-scale Sun-aligned arcs do not appear in this study. The selected events are sorted into different categories depending on their spatial and temporal behavior. Each category of polar arcs is compared to solar wind parameters to find out about a possible correlation between solar wind and arc appearance. Finally, the different polar arc models are compared with the results of this study.

2. Statistics

2.1. Method

[18] For a statistical study of polar arcs in the Northern Hemisphere UV images from the Polar spacecraft are used. The UV imager experiment on Polar provides global images

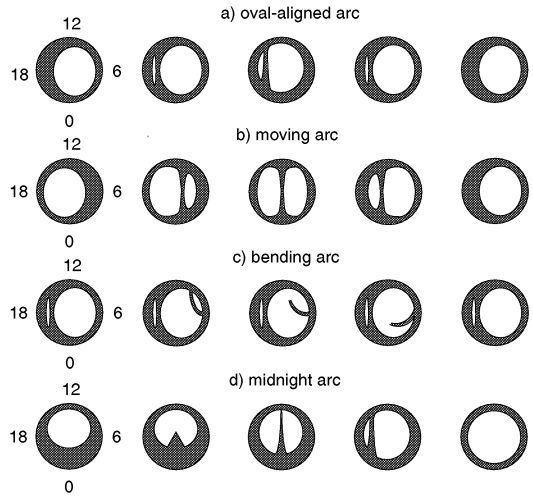

Figure 3. Schematic showing the temporal evolution of all clear polar arc types introduced in the study except multiple arcs.

of the aurora [*Torr et al.*, 1995]. It has an 8-degree field of view and can image the entire auroral oval above 60 degrees geographic latitude at spacecraft altitudes greater than 6 Re. The instrument is able to resolve 0.5 degrees in latitude at apogee; thus a single pixel projected to 100 km altitude from apogee is approximately 50 × 50 km. The study extends over a period of 3 months in winter 1998–1999 (1 December to 28 February). We choose winter months as summer UV images contain too much dayglow to detect the typically faint polar arcs. Sheets of 5 × 6 Polar UV images have been produced with a time interval between each image of at most 6 min. To be able to detect weaker arcs with emission intensities near the instrument threshold UV images are taken with a long integration period (36 s) and a fixed color scale is chosen which shows well the low energy flux range. The scale extends from 0.2 to 20 photons/cm^{2}s. The images are false color images which show the Lyman-Birge-Hopfield molecular nitrogen emissions in the 140–160 nm spectral region. For the image sheets used in this study a linear color scale (with black representing no intensity and white the highest intensity) and the magnetic apex coordinate system [*Richmond*, 1995] with corresponding magnetic local time (MLT) are used. The UVI instrument worked well during the entire 3 months having a high image quality despite two periods (21 December to 4 January and 24–28 February) where the image sensitivity was reduced by about 50% when a transparent MgF window was closed to protect the optics.

2.2. Classification of Polar Arcs

[19] The definition of an event is that an arc is visible in the polar cap or a split oval boundary is seen. Small-scale Sun-aligned arcs do not show up on the UV images because of their low luminosity and limited spatial extent. Polar arcs vary much in scale size, form, and luminosity. For this study, we classify each event as "clear polar arc" or "small split". By small splits we mean arcs which appear for less than 10 min and/or are not separated from the auroral oval clearly enough to allow a distinction from an oval associated arc. Excluded from the study are substorm formations such as extremely deformed substorm current wedges which resemble oval-aligned arcs or auroral streamers (north-south aligned structures within the oval during the recovery phase). Clear polar arcs have a variety of different forms. In the statistical study we found clear polar arcs that either separate from one side of the oval or develop from the nightside oval. Those which separate from the dawnside or duskside oval stay oval-aligned or move poleward. Of the poleward-moving arcs it is possible to distinguish between different subgroups. It also may happen that several different arc types are seen during the same event. A diversity of names exists in the literature to define different forms of polar arcs, but it remains unclear if the names refer to different arc types or only different appearances of the same auroral phenomenon. To avoid any confusion we use our own classification and subdivide the clear polar arcs on the basis of their spatial behavior into five different categories. Figure 3 shows schematically the evolution of each of the first four categories listed below.

1. "Oval-aligned arcs" usually appear near the dawnside or duskside oval but sometimes they may be quite separated from the side of the oval. They do not move considerably before they disappear (Figure 3a).

2. "Moving arcs" refer to those transpolar arcs which move across the entire polar cap unless they fade before reaching the other side of the oval. Moving arcs are not always Sun-aligned; however, both their dayside and nightside oval connection points move (Figure 3b).

3. "Bending arcs" are hook-shaped poleward-moving arcs where the sunward end of the arc separates from the main oval and moves toward the other side of the oval whereas the anti-sunward end remains fixed. An oval-aligned arc is often seen simultaneously on the other side of the oval as indicated in Figure 3c.

4. "Midnight arcs" represent those polar arc events where one single arc develops at the nightside auroral oval from a triangle-like bulge and then stretches toward noon where it may reach to the dayside auroral oval. Before disappearing the arc usually moves toward one side of the oval (Figure 3d).

5. With "multiple arcs" we describe events where many arcs fill the polar cap. There are a multitude of different evolutions, arcs appear simultaneously or one after the other, splitting from an oval side or shooting up from the nightside oval.

All polar arcs found on the UV images during the 3-month period are sorted into one of the above mentioned groups. With the division between small splits and clear polar arcs only the latter unambiguous cases are included in the different arc categories. The start and lifetime of polar arcs are defined by the time the arc is clearly separated from the auroral oval and by the time span from this separation until the arc disappears on the image or reunites with the main oval.

2.3. Comparison With Solar Wind Parameters

[20] To study the influence of solar wind parameters on the occurrence and dynamics of polar arcs we compare the

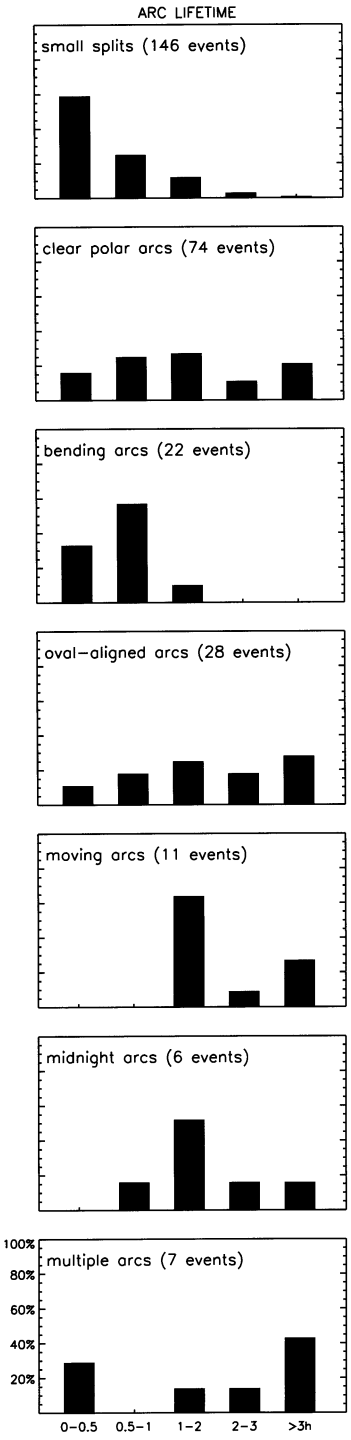

polar arc events with the IMF, solar wind speed, and ion density. For the comparison we use 5-min averaged data from the ACE satellite using GSM coordinates. ACE is located at ~220 R_E sunward of the Earth, and thus the solar wind conditions may have changed slightly when they reach the magnetopause. But since ACE has a nearly continuous coverage of the solar wind it is the most suitable satellite to use for this study. The solar wind data are shifted in time to take into account the propagation time of the solar wind to reach the dayside magnetopause (assumed to be located 10 R_E sunward of the Earth). The time delay is calculated for each day using 24-hour averaged solar wind speed and ACE to Earth magnetopause distance.

3. Results

[21] From the UVI database, 238 different polar arc events have been identified, 92 of which are clear polar arcs and 146 are small splits. For 18 of the clear polar arcs the evolution is not known, because of an insufficient field of view or because of weak emissions near the instrument threshold. These "unclassified clear polar arc events" are excluded from further analysis unless explicitly mentioned. The remaining 74 events are grouped into 28 oval-aligned arcs, 22 bending arcs, 11 moving arcs, 6 midnight arcs, and 7 multiple arc events.

3.1. Occurrence Frequency and Lifetimes of Polar Arcs

[22] Only a lower limit of the occurrence frequency of polar arcs can be obtained from the UV images. Approximately 25% of the time the UV imager does not point toward the Earth. These time periods (approximately 4 hours out of the 18-hour orbit period) are excluded from the analysis. The remaining time the imager did not always give a complete enough view of the auroral ionosphere for all polar arcs to be detected. With these limitations in mind we find that clear polar arcs are present during at least 10% of the time and small splits are present at least 6% of the time UV images are available.

[23] Figure 4 shows the lifetimes of small splits, of clear polar arcs, and of all five subtypes of clear polar arcs. The distribution of arc lifetimes as percentages of the events is shown for five time ranges. Only a lower limit of the average lifetime can be given since for 22% of the events the arc begins to develop before it is seen by the UV imager and for 30% of the events the arc disappears from the field of view before it fades. The majority of these events belongs to the category of oval-aligned arcs.

[24] The first two plots in Figure 4 show that a majority of the small splits have lifetimes less than half an hour whereas those of clear polar arcs range from several tens of minutes up to many hours. The plots of the different clear polar arc types show that there exists a characteristic range of lifetimes for most arc types. Bending arcs are nearly as short-lived as small splits whereas moving arcs may last several hours. Oval-aligned arcs seem to have no typical lifetime. Some events last only 30 to 60 min, others may last

Figure 4. (opposite) The distribution of the arc lifetimes as percentages of events for all small splits, clear polar arcs, and each of the clear polar arc types.

several hours. The subsets of midnight and multiple arcs are too small to be treated in a statistical way. For completeness, the study is, however, extended to include even these cases although the results should be treated with care. It can be seen that both midnight and multiple arcs have a large range of lifetimes comparable to those of oval-aligned arcs.

3.2. Spatial Evolution of the Different Polar Arc Types

[25] Figure 5 contains UV images of five clear polar arc events. The UV images in the figure are produced in the same way as the image sheets on which the statistics is based, using an integration period of 36 s and a color scale extending from 0.2 to 20 photons/cm^2 s. Each row in Figure 5 gives an example of the temporal evolution of each arc type. From top to bottom are shown an oval-aligned, a moving, a bending, a midnight, and a multiple arc event. The IMF data corresponding to the examples of different polar arc types shown in Figure 5 is presented in a later section (as Figure 10) where the IMF dependence of polar arcs is evaluated in detail.

[26] It is difficult to define an exact start time for most oval-aligned arcs (see the oval-aligned arc example in Figure 5). They often develop smoothly within an hour from an extension of the dawn or dusk sector oval to a clearly separated arc. In these cases the oval sector is often broad and/or contains multiple parallel bands of discrete arcs within it. More than half of the oval-aligned arcs occur during conditions of very low auroral luminosity of the entire oval. In seven cases it is hard to determine the evolution of the arc as the extremely faint nonmoving arc is visible only for 1 to 2 hours near the polar cap center until it becomes too faint to be detectable. The remaining oval-aligned arcs are clearly visible and all occur at the end of a substorm recovery phase. At least four oval-aligned arcs develop from a double-oval like structure which is a typical feature seen during a substorm recovery phase. Unfortunately, for a majority of the oval-aligned arc events the auroral luminosity is too weak or the imager coverage of the oval insufficient to see both sides of the auroral oval. Still, during at least six events, a secondary, often small or faint arc appears for a short time on the other side of the oval. For those two-thirds of the cases where the fading of an oval-aligned arc is seen by UVI, the arc moves back slightly toward the side of the oval before it disappears. In one-third of the cases a substorm begins while the arc remains visible for up to 1 or 2 hours.

[27] There are five moving arc events where an arc moves across the entire polar cap from one side of the oval to the other (see Figure 5, row 2), in one of the cases the arc moves back to the noon-midnight meridian where it disappears out of the field of view of the imager. In two cases the arcs fade in the center of the polar cap but one of them is such a faint event that it cannot be excluded that this arc reaches the other side of the oval as well. For the remaining cases the start or stop times are uncertain as the arc leaves the field of view before (2 cases) or after (2 cases) the arc reaches the central polar cap. Most of the moving arcs do not consist of only one clear Sun-aligned arc. In four cases the main arc splits into branches. Also, for most events the entire arc is not continuously visible and sometimes a part of the arc disappears. One-third of the moving arc events include a secondary, small arc on the opposite side of the oval. This secondary arc usually appears after the first arc has moved considerably poleward (see the moving arc example in Figure 5). Most of the moving arc events occur during nonsubstorm times. Three moving arcs fade several tens of minutes after a substorm onset.

[28] Bending arcs separate from the oval within 5 to 10 min and start almost immediately to bend into the polar cap where they disappear soon after. Unlike the event presented in Figure 5, row 3 the majority of the bending arcs are very faint and hard to detect on the UV images. Half of the bending arcs are accompanied by an oval-aligned arc on the other side of the auroral oval. In most cases this secondary arc appears before and lasts longer than the very short-lived bending arc. Nearly half of the bending arcs appear during substorm activity.

[29] All but one of the midnight arcs found in this study have a similar evolution. One typical example is shown in Figure 5, row 4. They all occur at the very end of a long substorm recovery phase or possibly at the end of a steady magnetospheric convection period. During the late recovery phase, bulges may appear one after the other at the very active poleward boundary of the nightside oval. In very few cases one of the bulges stretches to extremely high latitudes changing into a triangle-like shape. Out of this triangle a midnight arc shoots toward noon either immediately or up to 40 min later. The arc reaches the noon part of the auroral oval after only 10–20 min. During this process, the extremely broad and contracted main oval returns to normal thickness and size. Afterward, the often irregular midnight arc remains as an oval-aligned like arc for several hours before it fades. Only one of the midnight arcs develops at midnight, the others occur near one side of the oval but with a clear development from a bulge at the nightside auroral oval.

[30] For the multiple arcs, the events differ much from each other. For all events the evolution is very complex and at least one, often faint arc occurs in the middle of the polar cap (like in the example in Figure 5, row 5). In most cases the whole polar cap is filled by many branches. All but one event consist of three or more arcs.

[31] Although for most of the clear polar arcs the division into the five groups described above is obvious, 25% of the 74 clear polar arc events might have been put into a different category. As already mentioned, in seven of the oval-aligned arc cases the evolution is unclear as an arc is only visible for about an hour in the middle of the polar cap. There are 4 hybrid cases between oval-aligned and moving arcs. They are sorted into the group of moving arcs as a slow arc motion toward the central polar cap can be detected. Of the bending arcs, five cases have a nontypical evolution, four of which are very bright and appear at the beginning of a substorm recovery phase, the last consists of a bending arc which later transforms into an oval-aligned arc type. Of the midnight arcs only one event deviates from the typical evolution. It could have been sorted into the group of oval-aligned arcs since no bulge formation is seen before its appearance. For a few oval-aligned arcs and for most of the moving arcs crossing the entire polar cap it cannot be decided whether the arc develops from an existing bulge near one side of the oval similar to a midnight arc or whether the arc separates smoothly from the side of the oval.

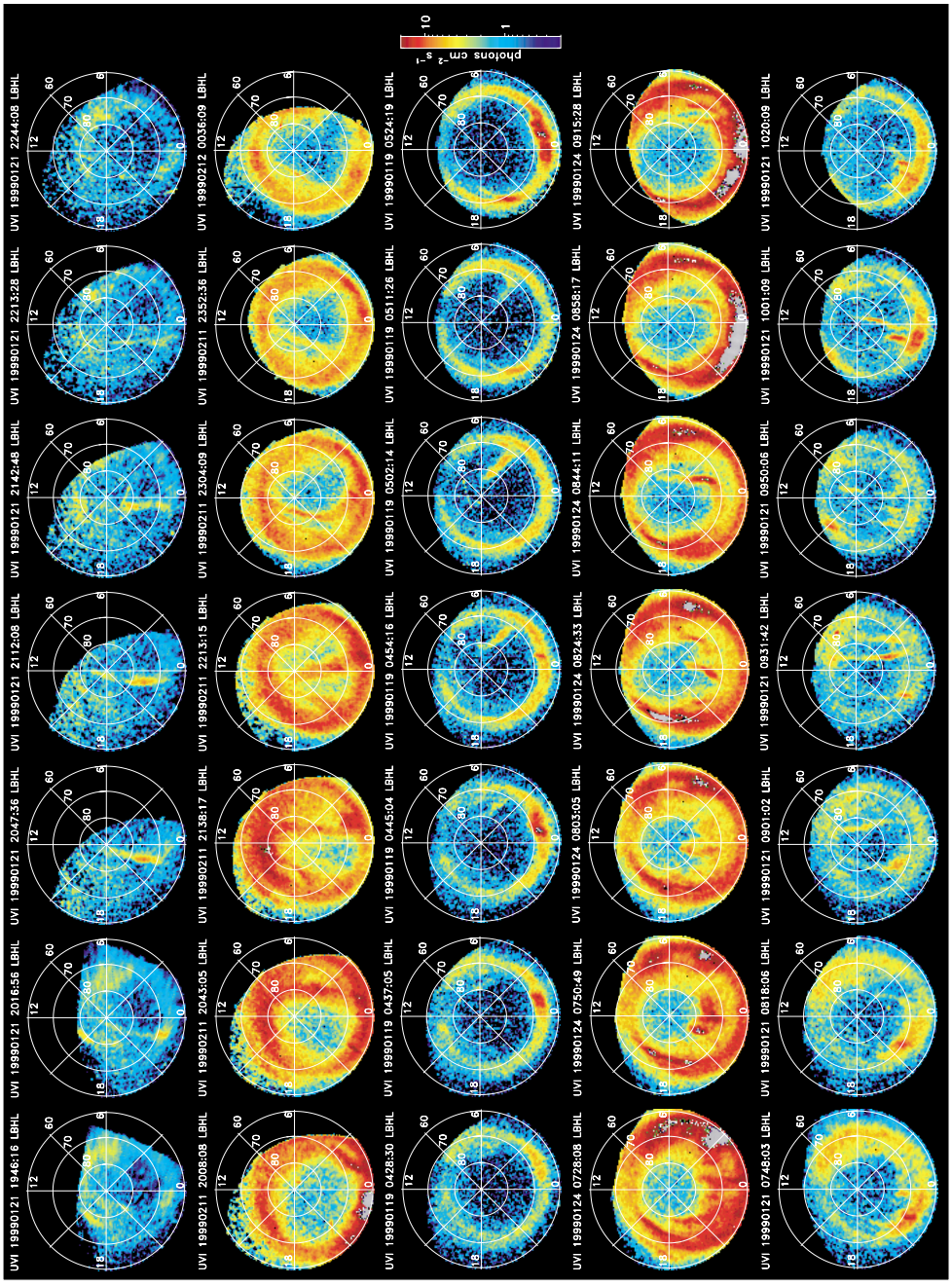
photons cm^{-2} s^{-1}
10
1
UVI 19990121 1946:16 LBHL
UVI 19990121 2016:56 LBHL
UVI 19990121 2047:36 LBHL
UVI 19990121 2112:08 LBHL
UVI 19990121 2142:48 LBHL
UVI 19990121 2213:28 LBHL
UVI 19990121 2244:08 LBHL
UVI 19990211 2008:08 LBHL
UVI 19990211 2043:05 LBHL
UVI 19990211 2138:17 LBHL
UVI 19990211 2213:15 LBHL
UVI 19990211 2304:09 LBHL
UVI 19990211 2352:36 LBHL
UVI 19990212 0036:09 LBHL
UVI 19990119 0428:30 LBHL
UVI 19990119 0437:05 LBHL
UVI 19990119 0445:04 LBHL
UVI 19990119 0454:16 LBHL
UVI 19990119 0502:14 LBHL
UVI 19990119 0511:28 LBHL
UVI 19990119 0524:19 LBHL
UVI 19990124 0728:08 LBHL
UVI 19990124 0750:49 LBHL
UVI 19990124 0803:05 LBHL
UVI 19990124 0824:33 LBHL
UVI 19990124 0844:11 LBHL
UVI 19990124 0858:17 LBHL
UVI 19990124 0915:28 LBHL
UVI 19990121 0818:06 LBHL
UVI 19990121 0901:02 LBHL
UVI 19990121 0931:42 LBHL
UVI 19990121 0950:06 LBHL
UVI 19990121 1001:09 LBHL
UVI 19990121 1020:09 LBHL
UVI 19990121 0748:03 LBHL

[32] Since the small split category contains all ambiguous cases it includes a multitude of different types. For completeness we mention them briefly: There exist oval-aligned arc-like splits which may be part of the main oval (35 events) and splits which occur at the end of a double oval event where the poleward oval boundary connects to the nightside such that an oval-aligned arc-like structure appears (13 events). Many other splits resemble bending arcs but with a very short length and lifetime. They appear near noon (24 events) or near the nightside oval (9 events). Another group consists of arcs which are clearly separated from the oval but with such low luminosity that one cannot decide if it is a polar arc or not (18 events). Midnight arc type splits are extremely large triangles which extend from the nightside to very high latitudes but do not develop into an arc which stretches further than the dawn-dusk meridian (32 events). Splits related to substorms are often arcs which may be part of an extremely expanded auroral bulge (15 events).

3.3. Comparison With Solar Wind Data

[33] In Figure 6 an overview time-sequence plot of all 3 months is shown with all polar arc events overlaid on solar wind data (light grey for small splits, dark grey for clear polar arcs including unclassified clear polar arc events). The first four rows show the total magnitude of the IMF, the IMF B_z component, the solar wind density, and the solar wind velocity measured by the ACE satellite. The IMF B_z component overlaid with polar arc events demonstrates the well-known fact that polar arcs preferably occur for northward IMF and disappear completely during long periods of southward IMF B_z (e.g., 10–11 December, 27 January, or 19 February). Large-scale fluctuations of the solar wind velocity and density seem not to be connected to the occurrence probability of polar arcs but the IMF magnitude is usually higher during periods with a high frequency of polar arcs. However, during periods of a very high occurrence frequency of polar arcs, such as 1–3 December or 20–22 January, the solar wind speed is higher than average. By combining the IMF magnitude with solar wind speed and the cosine function of the IMF clock angle θ (giving high values for northward IMF as $\theta = \arctan(|B_y|/B_z)$ for $B_z>0$ and $\theta = \pi \arctan(|B_y|/B_z)$ for $B_z<0$ in the following form $vB^2 \cos^4(\theta/2)(l_0^2/\mu_0)$ a parameter is obtained which correlates better with the occurrence probability of polar arcs than any of the solar wind parameters on their own. This parameter, which we refer to as the *anti-epsilon* parameter has the same form as the Akasofu-Perreault epsilon parameter [*Perreault and Akasofu*, 1978] but with a cosine function replacing the sine function. The factor l_0^2/μ_0 (with $l_0 = 7R_E$) is included in the anti-epsilon parameter to make the form similar to the epsilon parameter. By definition the anti-epsilon parameter has values near zero for strong southward IMF. During periods where the IMF is mainly northward but no polar arcs occur (e.g., 1–2 and 6–8 February) the parameter decreases to very low values as well. The peak values of the parameter overlap with long-lived arcs and/or a high polar arc density. However, there are certain days (e.g., 27 December or 26 February) with a lack of polar arc events despite quite a high magnitude of the anti-epsilon parameter. These days belong to the periods where the transparent MgF window was closed. Because of the low image resolution faint polar arc events have probably been missed. The anti-epsilon parameter and its correlation with polar arc occurrence will be discussed below in more detail.

[34] To be able to study the connection between arc occurrence and solar wind data in more detail the hourly averaged solar wind values before, during, and after the polar arc events are examined. The results are presented in Figures 7, 8, 11, and 12. These figures show the distribution of the IMF, the solar wind speed, density, dynamic pressure, energy flux, and the anti-epsilon parameter for all detected polar arcs. The plots are all done in a similar way. The values of each solar wind parameter are divided into four intervals. The range of each interval is chosen such that the solar wind parameter has values within one interval during 25% of the time. The time covered by the statistics includes the entire 3-month period except for the time intervals for which the UV imager did not point toward the auroral oval. Each of the plots show 12 different distributions given as percentages of polar arc events, the hourly averaged distribution up to 5 hours before and after the events (grey bars to the left and the right of the black bars) the distribution at the event start (left black bar) and the distribution of the average value during the event (right black bar). With these plots it is possible to get information not only on the typical distribution of the solar wind parameters for each type of polar arc event but also of the development of the solar wind values before, during, and after the events. Binning the solar wind data into four equal intervals makes any deviation from the average solar wind distribution more readily visible.

3.4. Connection Between Polar Arcs and Hourly Averaged IMF Components

[35] In Figure 7 the distribution between positive and negative signs of each IMF component are shown for each polar arc type. Here the above described grey and black bars are ordered from top to bottom, beginning with the average distribution for the 5th hour before the event at the top and ending with the 5th hour after the event at the bottom. The left and right dotted lines of each panel show the percentage of time (covered by the statistics) the IMF B_x, B_y, and B_z components have negative and positive values, respectively. Figures 8a–8c consist of distribution plots as described above for each of the IMF components IMF B_x, B_y, and B_z.

[36] The dotted lines in Figure 7 show that during the time period of the statistics, negative IMF B_x and positive B_y are dominant while B_z is equally distributed between both signs. This corresponds to the most common solar wind distribution. Comparing the distribution of the IMF components for small splits with those of the clear polar arcs (first two rows in Figures 7 and 8), it seems that the IMF B_x and

Figure 5. (opposite) Examples of clear polar arcs seen on the Polar UV imager. Each row shows the temporal evolution (from left to right) of one clear polar arc event (from top to bottom): Oval-aligned arc, moving arc, bending arc, midnight arc, and multiple arc event.

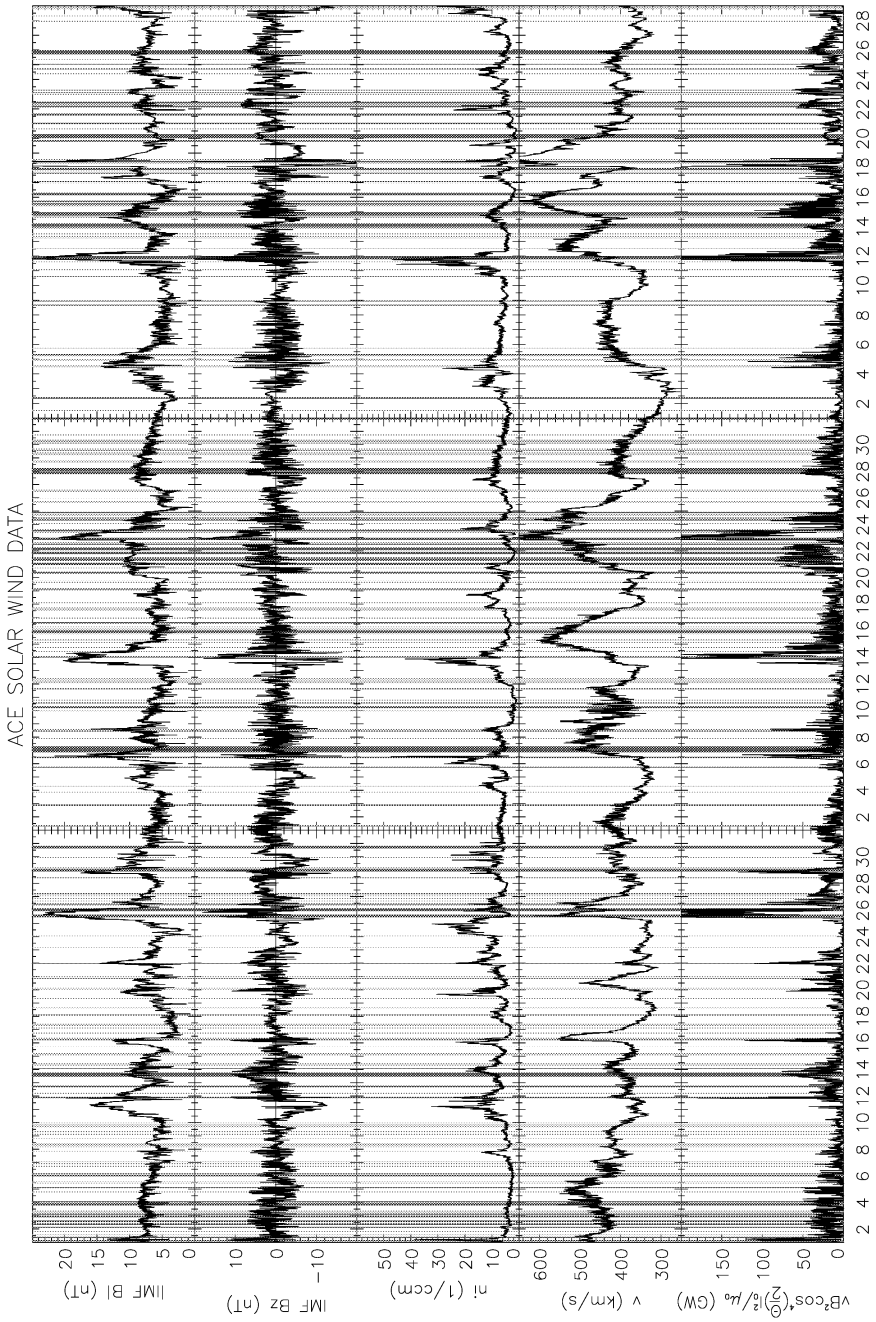

Figure 6. Overview plot of the entire statistical period with all polar arc events found in the Polar UV images overlaid on ACE solar wind data. From top to bottom, the total IMF magnitude, the IMF B_z component, the solar wind density, the solar wind velocity, and the anti-epsilon parameter are shown. The light grey and dark grey bars correspond to small splits and clear polar arc events, respectively.

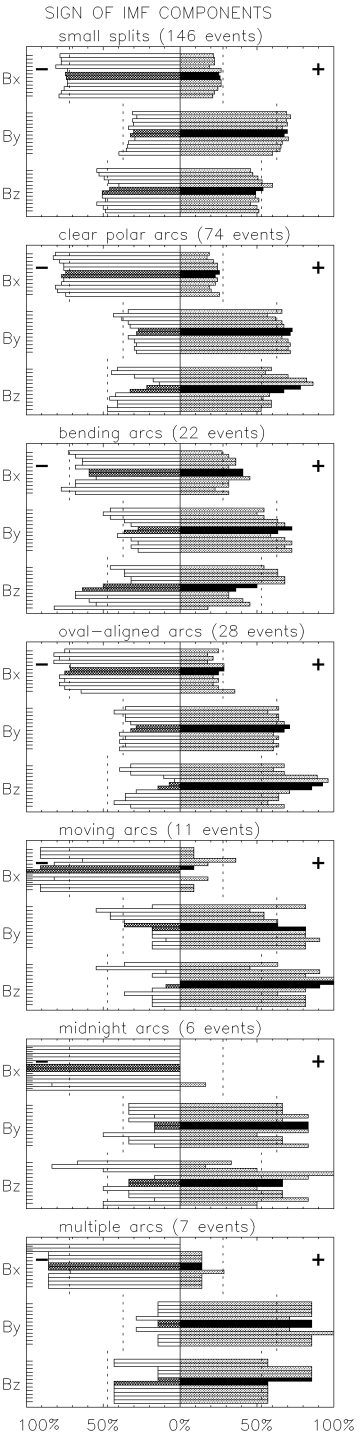

Figure 7. (opposite) The distribution of the sign of each IMF component as percentages of events for all small splits, clear polar arcs, and each of the clear polar arc types. The dotted lines give the distribution between positive and negative signs of each IMF component during the statistical time period. The grey bars above (below) the black bars show the hourly averaged IMF component signs up to 5 hours before (after) the polar arc event. The first and second black bars show the IMF component sign at the event start and the average IMF component sign during the event.

B_y distributions are similar to the average IMF distribution during the statistical time period and they do not change much during the 10 hours around the event. For the IMF B_z component, though, a clear difference between small splits and clear polar arcs is found. Small splits occur for weak IMF B_z with as many southward IMF as northward IMF cases. Clear polar arcs show a strong preference for northward IMF conditions. The highest percentage of northward IMF is found 1 to 2 hours before the event start. During the event the IMF is still northward for the majority of cases but already the hour after the event an average IMF B_z distribution is found.

[37] Looking at the different clear arc types (last five rows in Figures 7 and 8), major differences in the IMF distributions are found between bending, oval-aligned, and moving arcs. Midnight and multiple arcs have IMF characteristics similar to those of the moving arcs. The IMF B_x distribution shown in Figure 7 for bending and oval-aligned arcs is similar to the IMF B_x distribution itself. Bending arcs occur slightly more often for positive, oval-aligned arcs slightly more often for negative IMF B_x, compared to the average IMF B_x distribution during the statistical time period. In contrast to this, the last three arc types have a clear preference for negative IMF B_x. From Figure 8a it can be seen that for these arc types IMF B_x is not only negative but strongly negative. Most of the events occur for IMF B_x less than -5.4 nT, nearly none of them has positive IMF B_x values greater than 0.5 nT. The distribution of the IMF B_y component is less clear (Figures 7 and 8b). Bending and oval-aligned arcs occur for an average IMF B_y distribution, moving arcs mainly for weak IMF B_y, most often negative before and positive after the events, most midnight and multiple arcs occur during positive IMF B_y. The most significant difference between the clear polar arc types is found for the IMF B_z distribution (Figure 7). While bending arcs start to develop as often for B_z positive as negative, oval-aligned and moving arcs occur almost exclusively during northward IMF. Most midnight and multiple arcs develop during northward IMF. The change of the IMF B_z sign distribution in time is, however, similar for all clear polar arc events. The highest (lowest) number of northward IMF cases is found 1 to 2 hours before (after) the events. Looking at the strength of IMF B_z in Figure 8c, it is interesting that some bending arcs occur for IMF B_z values less than -2.3 nT while all other arc types appear during positive or only weakly negative IMF B_z values.

[38] As could be expected from earlier studies, a strong dependence is found of the polar arc location on the sign of IMF B_y. These results are presented in Table 1, listing the number of arcs which at their start time appear on the


a) IMF Bx
b) IMF By
c) IMF Bz
small splits (146 events)
small splits
small splits
clear polar arcs (74 events)
clear polar arcs
clear polar arcs
bending arcs (22 events)
bending arcs
bending arcs
oval−aligned arcs (28 events)
oval−aligned arcs
oval−aligned arcs
moving arcs (11 events)
moving arcs
moving arcs
midnight arcs (6 events)
midnight arcs
midnight arcs
multiple arcs (7 events)
multiple arcs
multiple arcs
100%
80%
60%
40%
20%
<−5.4 −5.4− −3.2 −3.2−0.5 >0.5 (nT)
<−2.3 −2.3−1.8 1.8−4.3 >4.3 (nT)
<−2.3 −2.3−0.2 0.2−2.3 >2.3 (nT)

Table 1. Polar Arc Locations at Their Start Time Versus Average IMF B_y Values During the Events

	Duskside Arc		Middle Arc		Dawnside Arc	
Arc Type	$B_y > 0$	$B_y < 0$	$B_y > 0$	$B_y < 0$	$B_y > 0$	$B_y < 0$
small splits	43	17	27	6	32	21
clear polar arcs	24	8	6	0	23	13
bending arcs	1	5	0	0	13	3
oval-aligned arcs	14	1	3	0	2	8
moving arcs	2	2	1	0	6	0
midnight arcs	3	0	1	0	1	1
multiple arcs	4	0	1	0	1	1

dawnside, in the middle, or on the duskside of the oval sorted by the average sign of IMF B_y during each event.

[39] Interestingly, there is only a marginal difference between the number of dawnside and duskside polar arcs. The majority of small splits and clear polar arcs appear during positive IMF B_y. This is probably due to the fact that IMF B_y is positive during two-thirds of the statistical time period. From Table 1 it is clear that most bending and moving arcs start to develop at the side of the oval which is opposite to the direction of the IMF B_y component. Both arc types move poleward, which means that most of these arcs move in the direction of IMF B_y. The nonmoving arc types, midnight and oval-aligned arcs, are on average located at the side of the oval toward which the IMF B_y component points. Also, multiple arc events start with an arc which appears at the side of the oval in direction of IMF B_y. Looking at the sign of IMF B_y at the event start time instead of the average during the event shows the same tendency, slightly better for bending arcs but less clear for oval-aligned and moving arcs.

[40] Each arc type contains 10–20% of cases which deviate from this scheme. Several of them are hybrid or faint events. Other clear polar arcs develop during IMF conditions which only slightly deviate from the expected IMF behavior. This includes cases such as an oval-aligned arc which occurs for IMF B_y having the "wrong" sign but values close to zero or a moving arc which appears after a clear IMF B_y drop from positive to zero instead of a sign change. Only the location of one midnight arc deviates clearly from the expected pattern. Not included in Table 1 are the secondary arcs which develop during one-third of all clear polar arc events. They are often very small or faint such that most of them could be categorized as small splits. Nearly all secondary arcs occur for the same IMF B_y sign (taking the average IMF B_y during the lifetime of the second arc) as the main arc itself.

3.5. Connection Between Polar Arcs and IMF Sign Changes

[41] Very interesting results are found from looking at the clock angle distributions for the different polar arc types in Figure 9. In this figure, the IMF clock angles between IMF B_z and the absolute value of IMF B_y are shown. The clock angles ranging from 0 (pure northward IMF) to 180 degrees (pure southward IMF) are divided into five equally large intervals. Each row shows for each polar arc type the average clock angle distribution (from left to right) 2 hours before, 1 hour before, at the event start, and during the event. The average IMF distribution during the entire statistical period is shown as the grey shaded areas in the first plot of the top row.

[42] On average, the IMF is distributed equally between positive and negative B_z with $|B_y|$ dominating $|B_z|$ most of the time. Small splits occur preferably for dominating $|B_y|$ and small, positive B_z. As expected already from Figures 8b and 8c the IMF clock angle does not change considerably for small splits. For bending arcs the average IMF clock angle distribution changes from around 70 degrees 1 hour before the event to around 100 degrees at the event start and back to around 80 degrees during the event. This corresponds to an IMF B_z sign change from northward to slightly southward and back again. Oval-aligned arcs occur on average for a constant IMF clock angle distributions around 45 degrees. The average IMF distribution changes toward this IMF clock angle distribution around 1 hour before the event start. Moving arcs occur on average approximately 1 hour after a change from 45 degrees toward strictly northward IMF and back again. As discussed below, this IMF clock angle change is due to an IMF B_y sign change. An IMF B_y sign change cannot be seen in this kind of plot since the absolute value of IMF B_y is used. For midnight and multiple arcs the IMF clock angle changes are less clear, but both occur for varying IMF clock angles during predominantly northward IMF. The IMF clock angle distribution plots of Figure 9 give only the percentage of events with an IMF clock angle within a certain interval. Thus, one cannot conclude with certainty from these plots that an IMF B_z (IMF B_y) sign change takes place for each single bending (moving) arc event or that all oval-aligned arcs occur during constant IMF.

[43] Table 2 gives the percentage of cases which contain IMF B_x, B_y, or B_z sign changes during the last 10 min (left column) and during the last 60 min (right column) before the polar arc starts to appear. In both cases sign changes up to 10 min after the event start have been included because of a possible uncertainty in the arc start time (it is often

Figure 8. (opposite) The distribution of (a) IMF B_x, (b) IMF B_y, and (c) IMF B_z as percentages of events for all small splits, clear polar arcs, and each of the clear polar arc types. The different magnitude ranges are chosen such that the IMF component is equally distributed between the four intervals during the statistical time period (dotted line at 25%). The grey bars to the left (right) of the black bars show the distribution of the hourly averaged IMF component up to 5 hours before (after) the polar arc event. The black bars show the IMF magnitude distribution at the event start (left black bar) and the average IMF magnitude distribution during the event (right black bar).

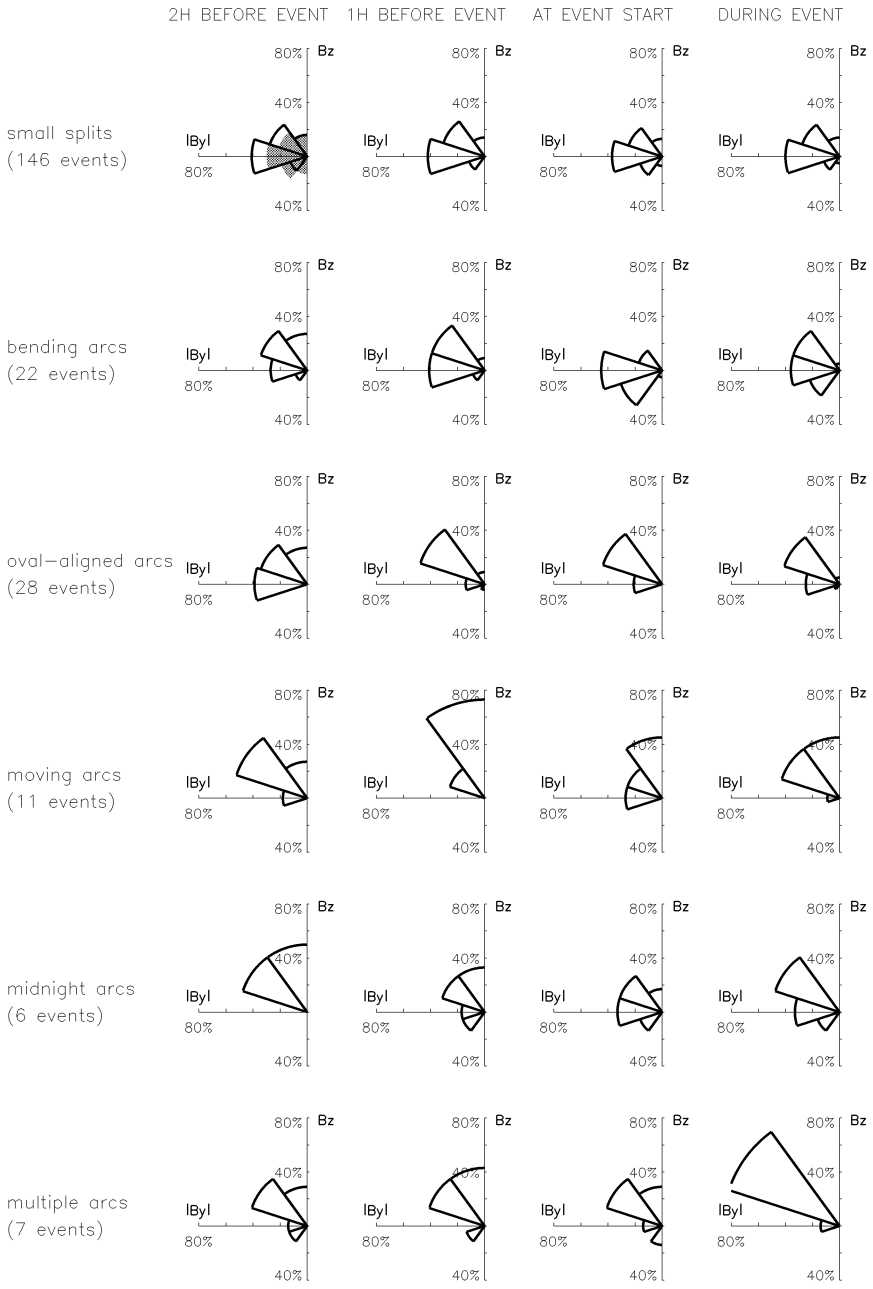

Figure 9. The distribution of the IMF clock angle between IMF B_z and the absolute value of IMF B_y for each polar arc type. The distributions of the hourly averaged clock angles for the second and the first hour before the events, at the event start, and the average value during the events are shown. The grey shaded areas in the first plot of the top row show the average IMF clock-angle distribution during the statistical time period.

Table 2. Percentages of Polar Arc Events With IMF Sign Changes Occurring Within Two Different Time Intervals Around the Arc Start Times

	B_x Sign Change		B_y Sign Change		B_z Sign Change	
Arc Type	−10/+10 min	−60/+10 min	−10/+10 min	−60/+10 min	−10/+10 min	−60/+10 min
small splits	12%	27%	16%	34%	42%	69%
clear polar arcs	8%	31%	14%	39%	34%	57%
bending arcs	5%	32%	9%	23%	50%	82%
oval-aligned arcs	18%	29%	14%	29%	18%	39%
moving arcs	0%	36%	18%	82%	27%	45%
midnight arcs	0%	17%	17%	67%	67%	67%
multiple arcs	0%	43%	14%	43%	29%	57%

difficult to define an exact start time from the UV images and the IMF data used for comparison is 5-min averaged data).

[44] Table 2 shows the same tendency as the IMF clock angle distribution plots. Nearly all of the bending (moving) arcs occur after an IMF B_z (IMF B_y) sign change. For half of the bending arcs an IMF B_z sign change takes place within 10 min of the start time but only one quarter of the moving arcs occur directly before or after an IMF B_y sign change. Most moving arcs start to develop 10 to 60 min after an IMF B_y sign change. Nearly half of the moving arcs involve an IMF B_z sign change as well. Interestingly, many small splits occur in connection with an IMF B_z sign change. Only oval-aligned arcs have a low rate of IMF sign changes. The majority of midnight and moving arcs involve both IMF B_y and IMF B_z sign changes. Except for multiple arcs only a minority of polar arcs appear after an IMF B_x sign change.

[45] Studying IMF time series for each of the clear polar arc events confirms the tendency shown in Table 2. Eight of 11 moving arcs appear after an IMF B_y sign change which took place up to 1 hour before the event start. Of the three other events, two events are hybrid cases which may be classified as oval-aligned arcs, one of them contains an IMF B_y drop from strongly positive to around zero. Only one unclear case exists (it may in fact be a midnight arc) where the arc moves nearly over the entire polar cap, without an IMF B_y sign change taking place within hours. Most bending arcs occur for small values of IMF B_z, changing several times between positive and negative values. All but one bending arc appear after an IMF B_z sign change. This event may be a multiple arc event since a secondary arc appears from midnight. Unfortunately, the field of view does not allow the entire event to be observed. From the comparison between event start and IMF data (which may contain uncertainties up to 10 min) we find that one-third of the bending arcs appear at an IMF B_z southward turn, one-third appear during a southward IMF period approximately 20–30 min after the last or before the next B_z sign change and one-third occur at the B_z sign change back to northward. The negative IMF B_z period is between 20 and 40 min long for half of the cases, for the other half it lasts 1 to 2 hours. Only in one case there is a strong B_z southward period of several hours. The only clear polar arcs which occur after many hours of nearly constant IMF are oval-aligned arcs. Not all oval-aligned arcs appear during these conditions. One-third of the oval-aligned arcs occur after an IMF B_y or B_z sign change, another third involves an IMF B_z or IMF B_y sign change during the event. For midnight and multiple arcs the IMF contains several sign changes. As the data look very different from case to case no clear tendency is found.

[46] Figure 10 shows the IMF data for the five arc-type examples of Figure 5. The plots demonstrate the clock angle dependence of the different arc types discussed in this section. The data is shifted in time to take into account the average distance of ACE to Earth magnetopause and average solar wind velocity during the 6 hours shown in the plots. The grey regions mark the arc lifetime, the dotted (and dashed) lines mark the start and stop times of a secondary arc (and tertiary arc in case of appearance). For the midnight arc event the dotted line indicates the time a triangle-shaped bulge develops. The oval-aligned arc occurs for nearly constant IMF B_y and B_z. The moving arc starts to develop during a major IMF B_y sign change, and a secondary arc appears at an IMF B_z drop to zero. The bending arc appears 15 min after a small IMF B_z southward turn. A midnight arc occurs during changing IMF B_z 35 min after the development of a bulge. The IMF was predominantly northward during the 2 hours preceding the bulge development. The three arcs of the multiple arc event appear during slightly changing IMF B_y and B_z.

3.6. Connection Between Polar Arcs and IMF Magnitude, Solar Wind Velocity, and Density

[47] Figure 11 shows the distribution of the IMF magnitude (Figure 11a), solar wind velocity (Figure 11b), and solar wind density (Figure 11c) for all polar arc events. The plots are done in the same way as the plots for the IMF B_x, B_y, B_z components in Figure 8.

[48] Studying the IMF magnitude distribution in Figure 11a, it is easily seen that small splits have a distribution which is nearly identical with the IMF distribution itself while most clear polar arcs appear for larger IMF values. The values of the IMF magnitude before, during, and after the event are approximately the same. Looking at the different clear polar arc types, bending arcs have a similar distribution as small splits, all other arc types occur on average for higher IMF magnitude. Moving arcs contain the highest percentage of cases which occur during strong IMF.

[49] The distribution plots of the solar wind speed (Figure 11b) show that not only most of the clear polar arcs but also most small splits appear during times of higher solar wind velocities than average. Bending arcs have again a distribution similar to small splits. Only oval-aligned arcs have a nearly average velocity distribution. Most moving, midnight, and multiple arcs occur during times of very high solar wind velocities.

[50] Interestingly, the solar wind density is neither correlated to small splits nor to clear polar arcs (Figure 11c). The density distributions for each clear polar arc type shows no clear tendency. Bending, oval-aligned, and multiple arcs

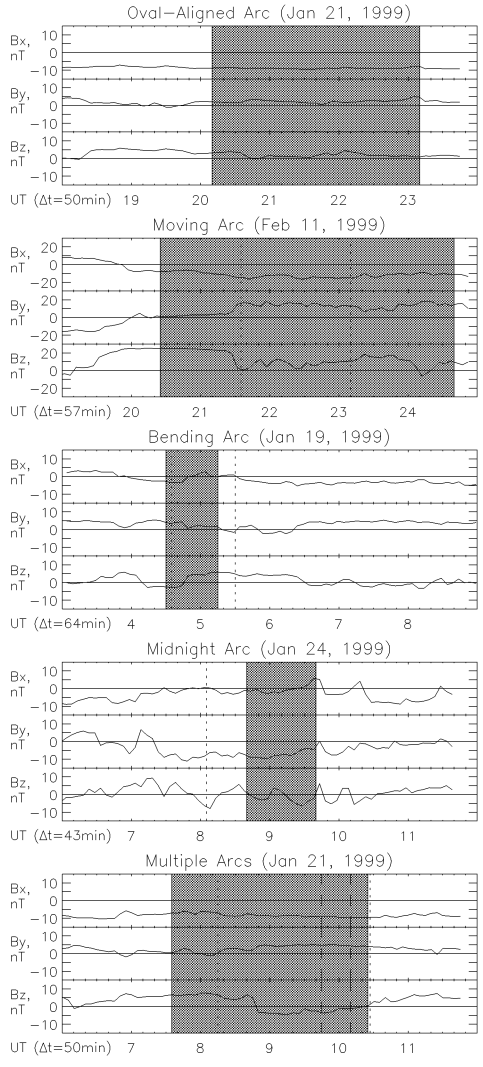

Figure 10. IMF components from ACE data for each of the clear polar arc type examples shown in Figure 5. The propagation time Δt (calculated from a 6-hour average of velocity and distance of ACE to Earth) is added to the time. The grey region shows the time period of the arc occurrence and the dotted lines show (in case of existence) start and stop times of the secondary and tertiary arcs except in the second to last plot, where the dotted line indicates the appearance of a bulge.

correlate with the average density distribution during the statistical time period whereas midnight arcs lack cases with highest density values and moving arcs occur either for very low or very high solar wind densities.

3.7. Connection Between Polar Arcs and Solar Wind Dynamic Pressure, Energy Flux, and the Anti-Epsilon Parameter

[51] In Figure 12, three derived quantities from the basic solar wind parameters are shown, the solar wind dynamic pressure $\rho_i v^2$ (Figure 12a), the solar wind energy flux $(1/\mu_0)vB^2$ (Figure 12b), and the anti-epsilon parameter $(l_0^2/\mu_0)vB^2 \cos^4(\theta/2)$ (Figure 12c) introduced above.

[52] One might expect that the solar wind dynamic pressure plays a role in the occurrence of polar arcs. This is not so obvious as demonstrated in Figure 12a which presents the solar wind dynamic pressure for all polar arcs. Neither small splits nor clear polar arcs deviate much from the average dynamic pressure distribution. Looking at each arc type in detail, one finds that both bending and oval-aligned arcs have average dynamic pressure distributions. For moving arcs the result is unclear, they do not appear within 1.2–2.4 nPa dynamic pressure range. Due to the very high solar wind velocities, midnight and multiple arcs have many cases with high solar wind dynamic pressure. This is most pronounced for midnight arcs with more than half of the events in the highest range of solar wind dynamic pressure.

[53] Looking at the solar wind energy flux $(1/\mu_0)vB^2$ in Figure 12b, one finds, as expected from the IMF magnitude and solar wind velocity distribution plots in Figures 11a and 11b, that the distribution of the energy flux for small splits corresponds to the average distribution during the statistical time period while clear polar arcs often occur for high energy flux values. Again, bending arcs have a nearly average energy flux distribution, oval-aligned arcs dominate only slightly for higher energy flux while the last three arc types occur during solar wind conditions with extremely high energy flux.

[54] The anti-epsilon parameter which combines the effect of strong solar wind velocity, IMF magnitude, and small IMF clock angle results in even more pronounced distributions within the range of high values (Figure 12c). Also small splits appear more frequently for higher anti-epsilon values. Of the clear polar arc events nearly 60% appear for the highest anti-epsilon values. For most clear polar arcs the anti-epsilon value is clearly higher than average during at least 5 hours before and after the events due to the IMF magnitude and the solar wind velocity distributions (comparing Figure 12c with Figures 11a and 11b). As expected from Figures 7, 8b, 8c, 11a, and 11b the distribution of the anti-epsilon parameter is nearly the same before and after the events for small splits whereas for clear polar arcs the anti-epsilon distribution changes considerably. The number of clear polar arc cases with highest anti-epsilon values increases to a maximum 2 hours before the start time and decreases to lower values during the event. The main cause for this is the change of the IMF B_z distribution with time (Figure 8c). The anti-epsilon distribution plots for each type of clear polar arcs reveal that all except bending arcs occur mostly for highest anti-epsilon values and have similar time-histories of the anti-epsilon

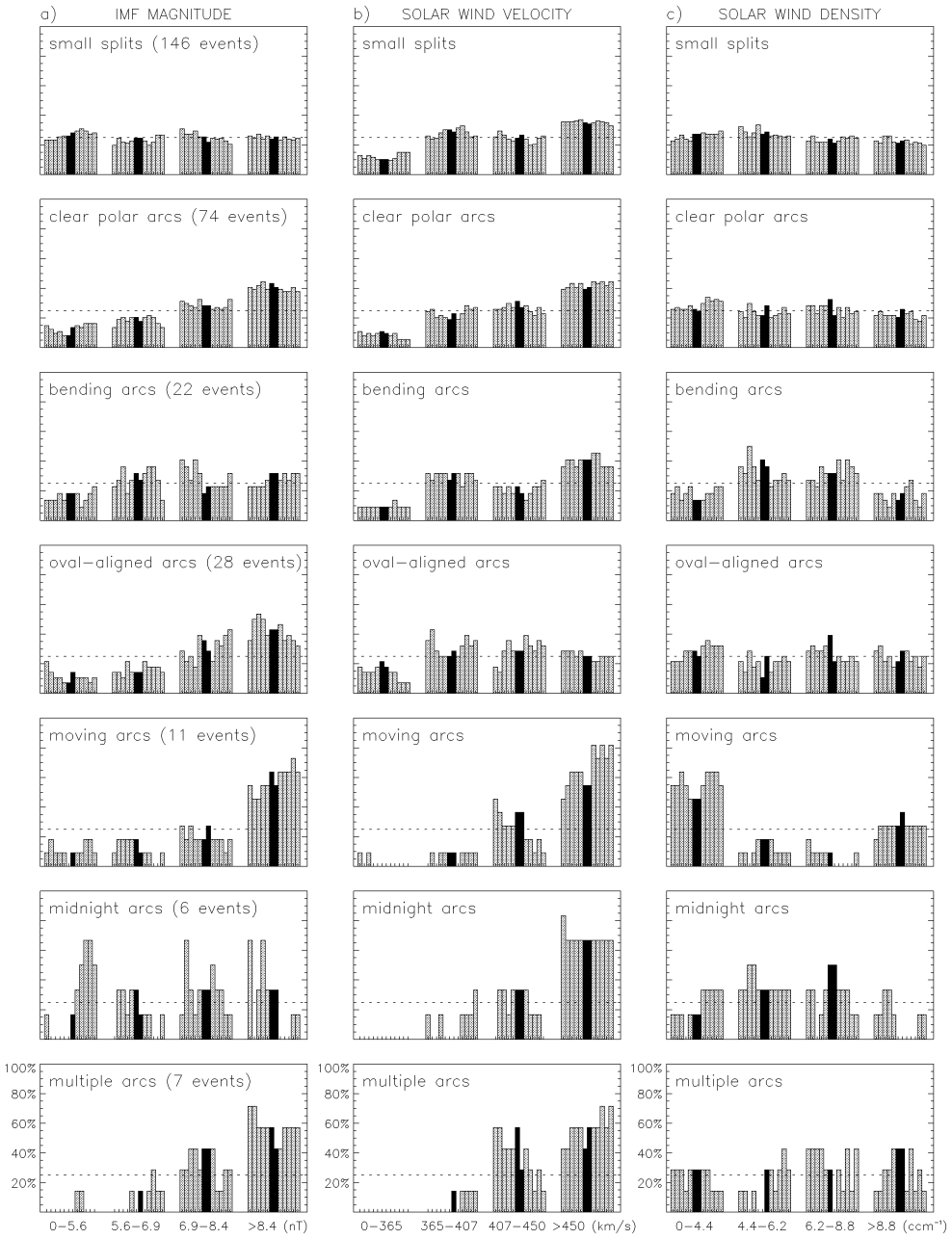

Figure 11. The distribution of (a) IMF magnitude, (b) solar wind velocity, and (c) solar wind density as percentages of polar arc events. The figures are done in the same way as Figure 8.

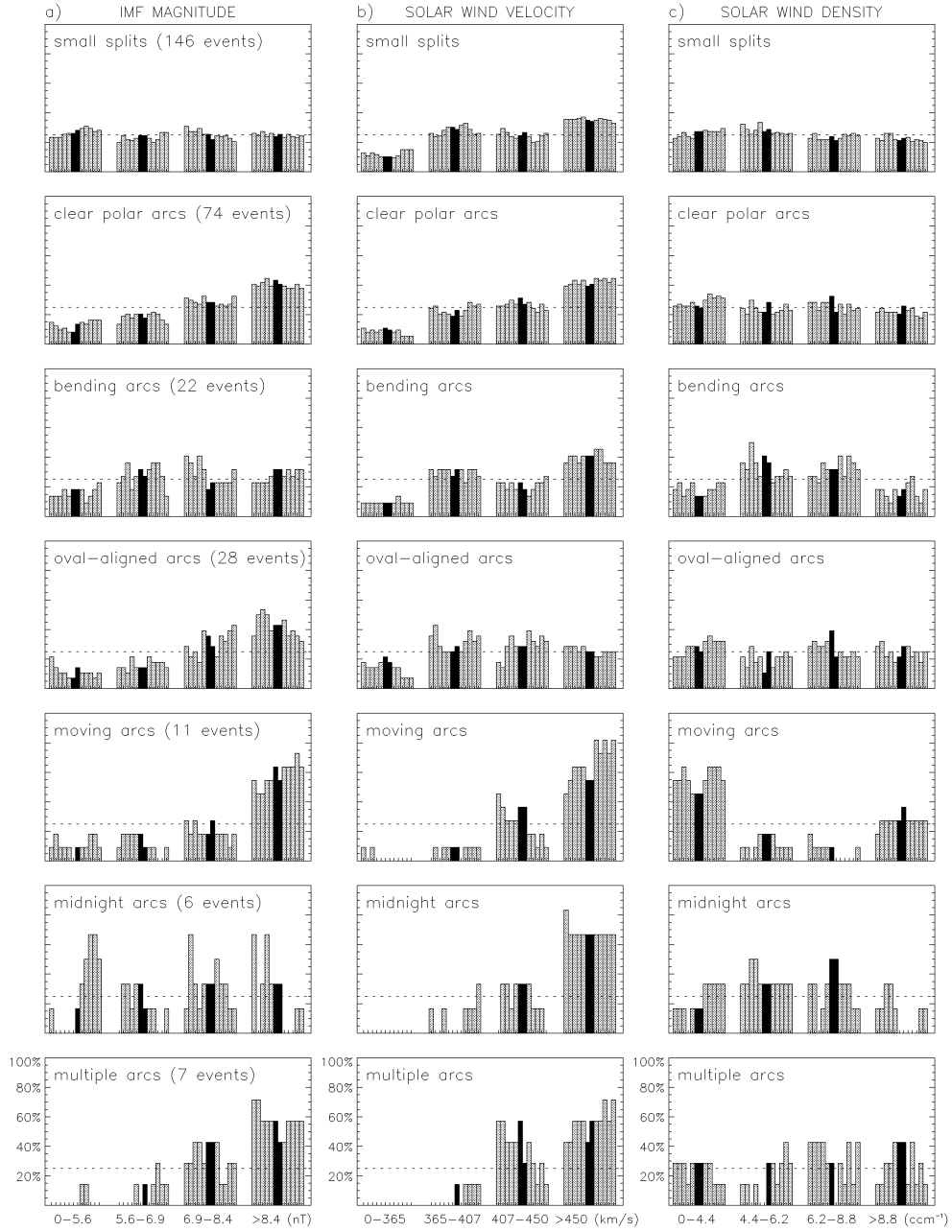
a) IMF MAGNITUDE
b) SOLAR WIND VELOCITY
c) SOLAR WIND DENSITY
small splits (146 events)
small splits
small splits
clear polar arcs (74 events)
clear polar arcs
clear polar arcs
bending arcs (22 events)
bending arcs
bending arcs
oval−aligned arcs (28 events)
oval−aligned arcs
oval−aligned arcs
moving arcs (11 events)
moving arcs
moving arcs
midnight arcs (6 events)
midnight arcs
midnight arcs
multiple arcs (7 events)
multiple arcs
multiple arcs
100%
80%
60%
40%
20%
0−5.6
5.6−6.9
6.9−8.4
>8.4 (nT)
0−365
365−407
407−450
>450 (km/s)
0−4.4
4.4−6.2
6.2−8.8
>8.8 (ccm⁻¹)

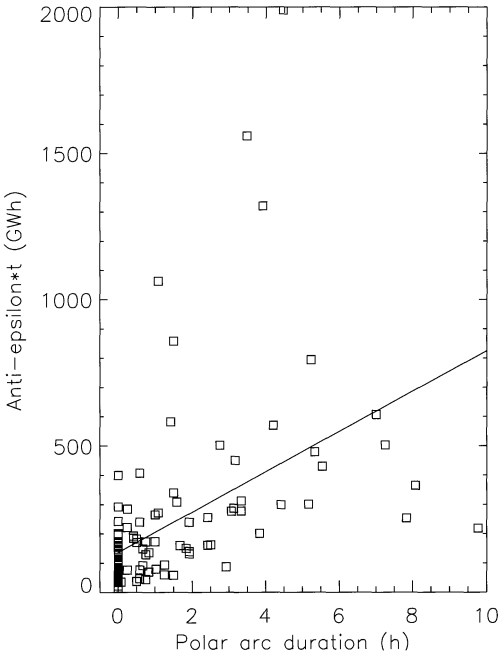

Figure 13. Each mark shows the time which is occupied by all clear arcs within one time period for which UV images are available (13 hours 45 min) versus the time integrated anti-epsilon parameter during that interval.

distribution. Looking at each clear polar arc event in detail, most cases show a temporal evolution of the anti-epsilon parameter which is similar to the change of the anti-epsilon distribution in Figure 12c. The anti-epsilon value increases to a maximum value up to hours before the event start and decreases during the event.

[55] The anti-epsilon parameter curve overlaid with all polar arc events from Figure 6 indicates already that this parameter may be used as a measure of the polar arc occurrence probability. For a better analysis it is necessary to analyze the parameter values during times where polar arcs are absent. A nearly average distribution of the solar wind parameters is found when taking the distribution of the anti-epsilon values for all time periods where no polar arc is visible on the UV imager. This is due to the fact that in most cases the anti-epsilon value is high also hours before and after the event. In Figure 13 the time integrated anti-epsilon parameter for each interval of continuous coverage by the UV imager (13 hours 45 min) is plotted versus the time during which clear polar arcs (including unclassified clear polar arc events) occur within this interval. With a correlation coefficient of 0.47 there is only a weak linear correlation between arc time and integrated anti-epsilon values. Still, Figure 13 contains other valuable information. The plot shows that of a total of 117 intervals during the entire 3 months there exist 56 intervals which do not contain any clear polar arcs at all. Nearly all of these non-arc periods (marks at $t = 0$) have integrated anti-epsilon values which do not exceed 190 GWh. Five of the seven non-arc intervals which have higher values than 190 GWh occur during the time period when the UV images have an extremely low resolution (due to the closure of the transparent MgF window at the UV imager). All intervals with integrated anti-epsilon values above 400 GWh contain at least one clear polar arc event. Excluding the seven non-arc intervals with the highest values, the maximum value for non-arc periods is 190 GWh. Around 60% of the intervals containing clear arcs have values above this limit. The distribution of different clear arc types in Figure 13 is complicated since one interval often contains several arc types, but, in general, intervals with highest anti-epsilon values contain moving or oval-aligned arcs. Multiple arcs occupy the longest interval time but have medium parameter values only. The more short-lived midnight arcs occur for even lower values and bending arcs occur during very low values, as is expected from Figure 12c.

4. Discussion

4.1. IMF B_y and B_x Dependence of Polar Arcs

[56] The study finds a clear IMF B_y control of the location and motion of clear polar arcs in the Northern Hemisphere. Nearly all clear polar arcs, separating from the side of the oval which is opposite to the direction of the IMF B_y component, move poleward in the direction of IMF B_y (bending arcs, moving arcs). The majority of the clear polar arcs occurring on the side of the oval in the direction of IMF B_y do not move considerably, they remain oval-aligned (midnight arcs, oval-aligned arcs). This confirms on a statistical basis what has been shown previously for single events: the results of *Valladares et al.* [1994] about the IMF B_y control of small-scale Sun-aligned arcs (Figure 1a) are valid also for large-scale polar arcs. As mentioned in the introduction, *Elphinstone et al.* [1990] found a slightly different IMF B_y dependence for Northern Hemisphere oval-aligned arcs (Figure 1b). While dusk arcs appear for positive IMF B_y only, dawnside arcs might appear for both signs of IMF B_y but only when IMF B_x has a sign opposite to IMF B_y. Whether or not these results are confirmed in this study is unclear, the results vary for different subsets of the clear polar arcs. Looking at oval-aligned arcs only the *Valladares et al.* [1994] results are confirmed. Including all secondary oval-aligned arcs the IMF distribution is similar to *Elphinstone et al.*'s [1990] results. Deviating from their results is the total lack of oval-aligned and secondary oval-aligned arcs for IMF B_x and B_y both being positive, although this may not be statistically significant as B_x and B_y are both positive only in 6% of the statistical time period (which is unusually rare). Our results indicate that

Figure 12. (opposite) The distribution of (a) the solar wind dynamic pressure ($\rho_i v^2$), (b) the solar wind energy flux ($((1/\mu_0)vB^2$), and (c) the anti-epsilon parameter ($vB^2 \cos^4(\theta/2)(l_0^2/\mu_0)$) as percentages of polar arc events. The figures are done in the same way as Figure 8.

only the location of the main arc is controlled by the IMF B_y sign, not the small secondary arcs which may be interpreted as part of a structured oval.

[57] The observations by *Valladares et al.* [1994] and others of small-scale Sun-aligned arcs appearing preferably on the dawn side is a feature that does not apply to larger polar arcs. In our study both small splits and clear polar arcs occur as often on the dusk as on the dawn side of the auroral oval.

[58] The more spectacular arc types, moving, midnight, and multiple arcs occur nearly exclusively for strong negative IMF B_x. This agrees with the statistical results by *Lassen and Danielsen* [1978] that small-scale Sun-aligned polar arcs occur more frequently in the Northern Hemisphere during periods of negative IMF B_x. As mentioned above, *Iijima et al.* [1984] show that the density of NBZ currents in the southern hemisphere increases linearly with positive IMF B_x. The more anti-parallel direction between the solar wind and the magnetospheric magnetic fields in the northern (southern) nightside hemisphere for negative (positive) B_x and northward B_z might have a strengthening effect on lobe reconnection in the northern (southern) hemisphere. This implies a stronger energy coupling between the solar wind and the magnetosphere on the tail lobe field lines, possibly showing up as a strengthening of the NBZ current system and in the occurrence of intense polar arcs.

4.2. A Comparison Between the Statistical Results and Different Polar Arc Models

[59] As mentioned in the introduction, the magnetotail is strongly twisted for nonzero IMF B_y if IMF B_z is positive. The degree of twisting increases downtail and toward the flanks. Since a time span of 30 to 60 min is required for the entire magnetotail to respond to an IMF direction change [*Frank and Craven*, 1988], a maximal twist should occur after an extended period of steady IMF. It is possible that the twisting increases with higher IMF magnitude (P. Janhunen, private communication, 2002). The solar wind conditions found for oval-aligned arcs support a very large and constant twisting of the entire tail. Nearly all oval-aligned arcs occur for positive IMF B_z and the IMF has been northward for at least 1 to 2 hours before the event start. The IMF is typically not varying much, often IMF B_y and B_z are equally strong, and in many cases the IMF magnitude is high. Oval-aligned arcs occur mostly on the side of the oval which maps to the plasma sheet flank reaching far into the lobes. The theory of a twisted plasma sheet with the high-latitude flank mapping to a polar arc [*Makita et al.*, 1991] fits very well to this type of clear polar arcs (Figure 2a).

[60] Moving arcs occur for similar IMF conditions as oval-aligned arcs with one major difference, they are probably triggered by an IMF B_y sign change up to an hour before the arc appears. An IMF B_y sign change from negative to positive causes in the Northern Hemisphere an arc to move from dawn to dusk and vice versa. The long time delay between the IMF B_y sign change and the arc appearance makes it probable that the development of a moving arc is connected to a large-scale tail reconfiguration caused by the IMF sign change. The statistical results support the theory proposed by *Kullen* [2000] of a rotation of the entire magnetotail which is induced by an IMF B_y sign change and makes it possible for a moving arc to appear in the ionosphere (Figure 2b). Again, northward IMF is necessary for a large tail twist to occur. The IMF B_y sign change causes the tail to change its twist first in the near-Earth tail and later in the far tail such that as an intermediate state the far tail plasma sheet maps into the high lobes of the near-Earth tail resulting in a poleward-moving arc in the ionosphere. According to this model the lifetime of a moving arc would be related to the time the magnetotail needs for a complete reconfiguration of its topology plus a possible internal magnetospheric delay. Assuming a solar wind speed of 500 km/s and a tail length of 150 R_E it takes approximately 40 min before the new IMF direction reaches the far tail. To penetrate from the flanks into the tail center takes another 45 to 60 min according to MHD simulation results [*Walker et al.*, 1999]. If we consider a further unknown time delay for field-aligned currents to reconfigure in response to the IMF change a moving arc should last for 1.5 hours or more. The lifetimes of moving arcs found in this study are extremely long, most of them last for about 2 hours, some even longer. For none of the moving arc cases was the IMF constant before and after the IMF B_y sign change. The IMF B_y component stays fairly constant but in many cases southward IMF turns occur either at the start time or during the event. An IMF B_z sign change at the arc start time probably influences the arc evolution, maybe in a similar way as for bending arcs. Interestingly, in all four cases where a secondary arc occurs during a moving arc event, a short-lived IMF B_z drop to zero takes place just before the appearance of this secondary arc. More detailed investigations are necessary to clarify the influence of an IMF B_z sign change on the motion and lifetime of moving arcs.

[61] Both the tail twist model [*Makita et al.*, 1991] and the twist rotation model [*Kullen*, 2000] propose a magnetotail topology which causes the closed field lines to map partly poleward of the main oval such that a region of closed field lines appears inside the polar cap. This field line configuration makes it possible for an auroral arc to appear poleward of the main oval boundary. The models do not explain explicitly how the field-aligned currents are generated in the tail, but both models assume that the field-aligned currents which cause the polar arc are generated in the same way as the region 1 currents of the main auroral oval, i.e., the currents are produced at the boundary between the plasma sheet and the lobes. In these models the polar arc currents have their source region in the boundary of the far tail plasma sheet near the flank which is twisted to high latitudes.

[62] Bending arcs occur for quite different solar wind conditions from the other clear polar arc types. Most bending arcs develop during IMF B_z values near zero and are connected to an IMF B_z sign change. Small splits appear during similar solar wind conditions as bending arcs. Also, nearly half of the small splits occur close to an IMF B_z sign change. Although small splits and bending arcs have an average solar wind distribution and a quite short lifetime in common, only one-third of the small splits resemble bending arcs. Even poleward moving auroral forms start to appear after an IMF B_z sign change (southward turn) [*Sandholt et al.*, 1998]. Whether or not all three arc types or subgroups of them are triggered by the same mechanism remains unclear. The theory developed by *Newell et al.* [1997] and *Chang et al.* [1998] where an IMF B_z flip causes

a jump of the dayside merging line, leading to a new region of open field lines in the high latitude ionosphere may explain the development of bending arcs. It predicts a short lifetime of the arc and its immediate appearance after an IMF B_z sign change. Some bending arcs reach far into the polar cap and last for more than 1 hour and thus they are likely to be associated with large-scale magnetotail deformations as well as the other polar arc types, which is not explicitly addressed in *Newell et al.*'s [1997] model. To extend this model to include IMF B_y sign changes as proposed by *Chang et al.* [1998] is questionable. Certainly a jump of the dayside merging line needs to be taken into account for any IMF sign change but the long time delay between the sign change and the arc occurrence and the long lifetime of the arcs indicate other mechanisms (such as magnetotail rotation).

[63] Midnight arcs develop in a completely different way from all other arc types. The arc forms from a large triangle-like bulge toward noon, within an extremely short time span, suggesting that some type of instability is involved in this process. The midnight arc model by *Rezhenov* [1995] assumes an interchange instability in the magnetotail to be responsible for the formation of an arc within the nightside oval (Figure 2c). The probability for an interchange instability increases with increasing curvature of the magnetic field lines. *Rezhenov* [1995] predicts that strong northward IMF B_z and/or strong solar wind speed during a substorm recovery is necessary for the tail magnetic field to become dipolarized and the plasma sheet to have a very short extension. These conditions agree very well with the observations of midnight arcs. All but one midnight arc occur clearly at the end of a long substorm recovery phase, during most cases the solar wind speed is very high and IMF B_z has been predominantly northward for at least 1 hour before the triangle-like bulge occurs. Midnight arcs are the only arcs occurring for clearly higher than average solar wind dynamic pressure which causes the plasma sheet to thicken such that the region of closed field lines maps to higher latitudes, resulting in a broad and contracted oval. According to *Rezhenov* [1995] the oval needs to be contracted so that the poleward oval boundary appears at very high latitudes. The UV images indicate that, just before the triangle-like bulge appears, the poleward boundary of the main oval is located on even higher latitudes than predicted by *Rezhenov* [1995]. His simulations of the motion of the poleward auroral boundary show that the oval on both sides of the arc moves considerably equatorward during the formation of the arc, which is not explicitly discussed in his paper. This phenomenon occurs in our observations as well. The whole oval widens during the formation of the midnight arc. The widening and thinning of the main oval probably reflects the recovery from a substorm to a normal state in the auroral ionosphere. The majority of the midnight arcs also involve IMF B_y and B_z sign changes. How this influences the arc formation is unclear. However, the dependence of the arc location on the sign of IMF B_y can be explained (as for oval-aligned arcs) by a twisted magnetotail.

[64] For multiple arcs the trigger mechanism is unclear. The solar wind conditions are similar to those for midnight and moving arcs. The solar wind speed and IMF magnitude are high and IMF B_z is in most cases positive. Maybe several plasma sheet filaments stretch into the tail lobes and map to different arcs, as suggested by *Huang et al.* [1987]. The changing IMF B_y and B_z components may cause the varying formations.

[65] By considering the dominant features of each clear polar arc event and examining whether common solar wind characteristics exist for arcs with a similar evolution, our statistical results indicated that primarily IMF clock angle changes are responsible for the evolution of different polar arc types. This does not exclude additional mechanisms, not revealed in this study, that may influence the polar arc evolution as well. Furthermore, it is likely that many events are the product of several mechanisms acting simultaneously on the magnetosphere-ionosphere system.

4.3. Interpretation of the Anti-Epsilon Parameter

[66] The statistical results show that a majority of the clear polar arcs occur for high solar wind speed and high IMF magnitude. One hour or more of predominantly northward IMF before event start seems to be a requirement for the arcs to occur. This holds for all clear polar arcs except for the bending arcs which more resemble the small splits. Although the overview plot in Figure 6 indicates a correlation on long timescales between high IMF values and solar wind velocities, the correlation between IMF magnitude and solar wind speed for 5 min as well as 1-hour averaged data is very low ($r \sim 0.29$) during the statistical time period. A correlation between IMF clock angle and IMF magnitude does not exist ($r = 0.09$). The correlation coefficients between IMF magnitude and solar wind velocities for polar arcs are comparable to those of the solar wind. ($r = 0.23$ for small splits and 0.41 for clear polar arcs). In a conclusion, not all arcs for which the IMF values are high occur during high solar wind velocities and vice versa.

[67] Most arcs visible in the UV images appear for a high value of the solar wind energy flux $(1/\mu_0)vB^2$. Whether a high solar wind energy flux is necessary to trigger a polar arc or whether it provides the energy for a high luminosity of polar arcs cannot be determined from this study. It is, however, likely that the magnitude of the solar wind energy flux is responsible for the rate of occurrence of intense polar arcs. A support for this assumption is that most bending arcs, which, on the average are very faint and hard to detect, do not occur for high solar wind energy flux values.

[68] In obtaining a parameter which combines the effect of high solar wind magnitude and/or solar wind speed with a northward IMF direction several combinations are possible. In this paper the anti-epsilon parameter is introduced, consisting of the well-established Akasofu-Perreault parameter with a cosine function instead of a sine function. Our statistical results show that during a time period with a high anti-epsilon parameter many and/or long-lived clear polar arcs occur. The choice for this parameter is somewhat arbitrary. The anti-epsilon parameter has only marginally higher values during polar arc events, for periods of high arc frequencies and correlation to arc lifetime (Figures 6, 12c, and 13) than other combinations of v, $|B|$ and IMF B_z northward. For example, the ϵ^*-parameter by *Iijima et al.* [1984] gives fairly good correlations with arc frequencies and lifetimes as well. As mentioned above, this parameter is strongly correlated to the peak current density of NBZ currents in the

dayside polar cap. The connection between the anti-epsilon parameter and the polar arc current densities is not investigated here. But the similarity to the ϵ*-parameter suggests that the anti-epsilon parameter has a strong correlation with the current density of clear polar arcs as well.

[69] Another way to interpret the anti-epsilon parameter can be found from its connection to substorms. A negative correlation between AE index and polar arc occurrence has been shown previously [*Ismail et al.*, 1977; *Lassen and Danielsen*, 1989]. The connection between the Akasofu-Perreault epsilon parameter and the AE index is well-known. This means that for a high anti-epsilon value the AE index is low. It is commonly believed that during southward IMF solar wind energy is stored inside the magnetotail which is released periodically via substorm processes. Our suggestion is that for high anti-epsilon values (low AE but high solar wind energy flux) the energy coupling process is different, the energy is not stored inside the magnetotail but large tail deformations take place which create the closed field line topology necessary for polar arcs to occur.

5. Summary

[70] We present a statistical study of over 200 polar arcs identified utilizing the Polar UV imager. Solar wind data from the ACE satellite are examined in order to determine a possible solar wind control of these arcs. A strong IMF control of clear polar arcs is found, while small splits seem to appear nearly independent of solar wind conditions. The majority of clear polar arcs occur for northward IMF with high IMF magnitude and/or high solar wind speed.

[71] In this paper we have introduced the anti-epsilon parameter $vB^2 \cos^4(\theta/2)(l_0^2/\mu_0)$ which combines the effect of northward IMF with a high IMF magnitude and solar wind speed. A high anti-epsilon parameter means high solar wind energy flux during northward IMF conditions. Northward IMF seems to be necessary for most polar arcs to occur, with high IMF magnitude and large solar wind velocity providing the energy for a high luminosity of polar arcs. Similar to the original epsilon parameter for substorms, this parameter gives on long timescales (days) the occurrence probability for clear polar arcs. Most of the clear polar arcs occur for high values of the anti-epsilon parameter, with the highest anti-epsilon values occurring 1 to 2 hours before an event start.

[72] The clear polar arc cases are subdivided into five categories according to their spatial behavior: bending arcs, oval-aligned arcs, moving arcs, midnight arcs, and multiple arcs. The arc location for all arc types is controlled by the IMF B_y component. In the Northern Hemisphere, bending and moving arcs move toward the side of the oval pointed at by IMF B_y whereas the nonmoving arcs are located at that side of the oval from the very beginning. A clear IMF B_x dependence is found for moving, midnight, and multiple arcs. They all occur preferably during strong, negative IMF B_x. IMF clock angle changes are responsible for the formation of at least two different arc types. For each of the arc types there exist a set of favorable solar wind conditions which are listed below:

1. Bending arcs have similar characteristics to those of small splits. Bending arcs occur during average IMF conditions with IMF B_z fluctuating around zero and for slightly higher solar wind velocities than average. They are probably initiated by an IMF B_z sign change. They appear quite often but are short-lived and faint.

2. Oval-aligned arcs are a common northward IMF phenomenon occurring for high IMF magnitude, often for steady IMF with IMF B_z and B_y components having similar magnitudes. They persist from tens of minutes up to hours.

3. Moving arcs occur during IMF conditions with a strong northward component and generally large solar wind speed and IMF magnitude. They usually develop up to an hour after a large-scale IMF B_y sign change and last for several hours.

4. Midnight arcs occur for high solar wind speed and solar wind dynamic pressure with varying IMF B_y and B_z and at least 1 hour of predominantly northward IMF before a large triangle-like bulge appears out of which a midnight arc develops. All midnight arcs develop at the end of a substorm recovery phase and last up to some hours.

5. Multiple arcs occur during high solar wind speed and magnitude with positive IMF B_z and varying IMF B_y and B_z. What triggers the appearance of each arc in a multiple arc event remains unclear.

[73] The results presented in this statistical study show clearly that the occurrence and evolution of polar arcs is determined to a large extent by the solar wind energy and IMF orientation. Especially the latter seems to play a major role in reorganization of the magnetosphere which is reflected in the change of the high latitude auroral precipitation pattern.

[74] **Acknowledgments.** The work at University of Washington was supported in part by the research grant NAG 5-3170 of the National Aeronautics and Space Administration. The work at the University of Texas at Dallas was supported by NSF grant ATM9814144. We also want to thank N. Ness at Bartol Research Institute, D.J. McComas at Los Alamos National Laboratory, and the CDAWeb for providing ACE solar wind data.

References

Akasofu, S.-I., The solar wind-magnetosphere energy coupling and magnetospheric disturbances, *Planet. Space Sci.*, *28*, 495, 1980.

Bonnell, J., R. C. Elphic, S. Palfery, R. J. Strangeway, W. K. Peterson, D. Klumapar, C. W. Carlson, R. E. Ergun, and J. P. McFadden, Observations of polar cap arcs on FAST, *J. Geophys. Res.*, *104*, 12,669, 1999.

Brittnacher, M., M. Fillingim, G. Parks, G. Germany, and J. Spann, Polar cap area and boundary motion during substorms, *J. Geophys. Res.*, *104*, 12,251, 1999.

Chang, S.-W., et al., A comparison of a model for the theta aurora with observations from Polar Wind and SuperDARN, *J. Geophys. Res.*, *103*, 17,367, 1998.

Cowley, S. W. H., Magnetospheric asymmetries associated with the y-component of the IMF, *Planet. Space Sci.*, *29*, 79, 1981.

Craven, J. D., L. A. Frank, C. T. Russell, E. J. Smith, and R. P. Lepping, Global auroral responses to magnetospheric compressions by shocks in the solar wind: Two case studies, in *Solar Wind–Magnetosphere Coupling*, edited by Y. Kamide and J. A. Slavin, p. 367, Terra Sci., Tokoyo, 1986.

Craven, J. D., L. A. Frank, J. S. Murphree, L. A. Frank, and L. L. Cogger, Simultaneous optical observations of transpolar arcs in the two polar caps, *Geophys. Res. Lett.*, *18*, 2297, 1991.

Cumnock, J. A., et al., Evolution of the global aurora during positive IMF B_z and varying IMF B_y conditions, *J. Geophys. Res.*, *102*, 17,489, 1997.

Cumnock, J. A., J. R. Sharber, R. A. Heelis, L. G. Blomberg, G. A. Germany, J. F. Spann, and W. R. Coley, Interplanetary magnetic field control of theta aurora development, *J. Geophys. Res.*, doi:10.1029/2001JA009126, in press, 2002.

Elphinstone, R. D., K. Jankowska, J. S. Murphree, and L. L. Cogger, The configuration of the auroral distribution for interplanetary magnetic field B_z northward, 1, IMF B_x and B_y dependencies as observed by the Viking satellite, *J. Geophys. Res.*, *95*, 5791, 1990.

Frank, L. A., and J. D. Craven, Imaging results from Dynamics Explorer 1, *Rev. Geophys.*, *26*, 249, 1988.
Frank, L. A., J. D. Craven, J. L. Burch, and J. D. Winningham, Polar view of the Earth's aurora with dynamic explorer, *Geophys. Res. Lett.*, *9*, 1001, 1982.
Frank, L. A., J. D. Craven, and R. L. Rairden, Images of the Earth's aurora and geocorona from the Dynamics Explorer mission, *Adv. Space Res.*, *5*(4), 53, 1985.
Frank, L. A., et al., The theta aurora, *J. Geophys. Res.*, *91*, 3177, 1986.
Gusev, M. G., and O. A. Troshichev, Hook-shaped arcs in dayside polar cap and their relationship to the IMF, *Planet. Space Sci.*, *34*, 489, 1986.
Gussenhoven, M. S., Extremely high-latitude auroras, *J. Geophys. Res.*, *87*, 2401, 1982.
Gussenhoven, M. S., and E. G. Mullen, Simultaneous relativistic electron and auroral particle access to the polar caps during interplanetary magnetic field B_z northward: A scenario for an open field line source of auroral particles, *J. Geophys. Res.*, *94*, 17,121, 1989.
Hones, E. W., Jr., J. D. Craven, L. A. Frank, D. S. Evans, and P. T. Newell, The horse-collar aurora: A frequent pattern of the aurora in quiet times, *Geophys. Res. Lett.*, *16*, 37, 1989.
Huang, C. Y., L. A. Frank, W. K. Peterson, D. J. Williams, W. Lennartson, D. G. Michell, R. C. Elphic, and C. T. Russell, Filamentary structures in the magnetotail lobes, *J. Geophys. Res.*, *92*, 2349, 1987.
Huang, C. Y., J. D. Craven, and L. A. Frank, Simultaneous observations of a theta aurora and associated magnetotail plasmas, *J. Geophys. Res.*, *94*, 10,137, 1989.
Iijima, T., and T. A. Potemra, The relationship between interplanetary quantities and Birkeland current densities, *Geophys. Res. Lett.*, *4*, 442, 1982.
Iijima, T., T. A. Potemra, L. J. Zanetti, and P. F. Bythrow, Large-scale Birkeland currents in the dayside polar region during strongly northward IMF: A new Birkeland current system, *J. Geophys. Res.*, *89*, 7441, 1984.
Ismail, S., and C.-I. Meng, A classification of polar cap auroral arcs, *Planet. Space Sci.*, *30*, 319, 1982.
Ismail, S., D. D. Wallis, and L. L. Cogger, Characteristics of polar cap sun-aligned arcs, *J. Geophys. Res.*, *82*, 4741, 1977.
Kaymaz, Z., G. L. Siscoe, J. G. Luhmann, R. P. Lepping, and C. T. Russell, Interplanetary magnetic field control of magnetotail magnetic field geometry: IMP 8 observations, *J. Geophys. Res.*, *99*, 11,113, 1994.
Kullen, A., The connection between transpolar arcs and magnetotail rotation, *Geophys. Res. Lett.*, *27*, 73, 2000.
Kullen, A., and L. G. Blomberg, The influence of IMF B_y on the mapping between the Earth's magnetotail and its ionosphere, *Geophys. Res. Lett.*, *23*, 256, 1996.
Lassen, K., and C. Danielsen, Quiet time pattern of auroral arcs for different directions of the interplanetary magnetic field in the yz-plane, *J. Geophys. Res.*, *83*, 5277, 1978.
Lassen, K., and C. Danielsen, Distribution of auroral arcs during quiet geomagnetic conditions, *J. Geophys. Res.*, *94*, 2587, 1989.
Makita, K., C. I. Meng, and S. I. Akasofu, Transpolar auroras, their particle precipitation, and IMF B_y component, *J. Geophys. Res.*, *96*, 14,085, 1991.
McEwen, D. J., and Y. Zhang, A continuous view of the dawn-dusk polar cap, *Geophys. Res. Lett.*, *27*, 477, 2000.
Meng, C.-I., Polar cap arcs and the plasma sheet, *Geophys. Res. Lett.*, *8*, 273, 1981.
Milan, S. E., M. Lester, S. W. H. Cowley, and M. Brittnatcher, Convection and auroral signatures of transient magnetic flux transfer at the magnetopause, *J. Geophys. Res.*, *105*, 15,741, 2000.
Murphree, J. S., and L. L. Cogger, Observed connections between apparent polar cap features and the instantaneous diffuse auroral oval, *Planet. Space Sci.*, *29*, 1143, 1981.
Murphree, J. S., C. D. Anger, and L. L. Cogger, The instantaneous relationship between polar cap and oval auroras at times of northward interplanetary magnetic field, *Can. J. Phys.*, *60*, 349, 1982.
Newell, P. T., D. Xu, C.-I. Meng, and M. G. Kivelson, Dynamical polar cap: A unifying approach, *J. Geophys. Res.*, *102*, 127, 1997.
Owen, C. J., J. A. Slavin, I. G. Richardson, N. Murphy, and R. J. Hynds, Average motion, structure and orientation of the distant magnetotail determined from remote sensing of the edge of the plasma sheet boundary layer with $E > 35$ keV ions, *J. Geophys. Res.*, *100*, 185, 1995.
Perreault, P., and S. I. Akasofu, Study of geomagnetic storms, *Geophys. J. R. Astron. Soc.*, *54*, 547, 1978.
Peterson, W. K., and E. G. Shelley, Origin of the plasma in a cross-polar cap auroral feature (theta aurora), *J. Geophys. Res.*, *89*, 6729, 1984.
Rairden, R. L., and S. B. Mende, Properties of 6300-A auroral emission at south pole, *J. Geophys. Res.*, *94*, 1402, 1989.
Richmond, A. D., Ionospheric electrodynamics using magnetic apex coordinates, *J. Geophys. Res.*, *47*, 191, 1995.
Rezhenov, B. V., A possible mechanism for theta aurora formation, *Ann. Geophys.*, *13*, 698, 1995.
Sandholt, P. E., C. J. Farrugia, J. Moen, O. Noraberg, B. Lybekk, T. Sten, and T. Hansen, A classification of dayside auroral forms and activities as a function of interplanetary magnetic field orientation, *J. Geophys. Res.*, *103*, 23,325, 1998.
Slinker, S. P., J. A. Fedder, D. J. McEwen, Y. Zhang, and J. G. Lyon, Polar cap study during northward interplanetary magnetic field on 19 January 1998, *Phys. Plasmas*, *8*, 1119, 2001.
Torr, M. R., et al., A far ultraviolet imager for the international solar-terrestrial physics mission, *Space Sci. Rev.*, *71*, 329, 1995.
Tsyganenko, N. A., A magnetospheric magnetic field model with a warped tail current sheet, *Planet. Space Sci.*, *37*, 5, 1989.
Valladares, C. E., H. C. Carlson, Jr., and K. Fukui, Interplanetary magnetic field dependency of stable sun-aligned polar cap arcs, *J. Geophys. Res.*, *99*, 6247, 1994.
Walker, R. J., R. L. Richard, T. Ogino, and M. Ashour-Abdalla, The response of the magnetotail to changes in the IMF orientation: The magnetotail's long memory, *Phys. Chem. Earth, Part C*, *24*, 221, 1999.
Zhu, L., R. W. Schunk, and J. J. Sojka, Polar cap arcs: A review, *J. Atmos. Sol.-Terr. Phys.*, *59*, 1087, 1997.

L. G. Blomberg and A. Kullen, Royal Institute of Technology, Alfvén Laboratory, 10044 Stockholm, Sweden. (Lars.Blomberg@alfvenlab.kth.se; kullen@plasma.kth.se)
M. Brittnacher, Department of Earth and Space Sciences, University of Washington, Box 351650, Seattle, WA 98195, USA. (britt@geophys.washington.edu)
J. A. Cumnock, Center for Space Sciences, University of Texas at Dallas, Richardson, TX 75080, USA. (cumnock@utdallas.edu)

Paper 4

Relation of polar auroral arcs to magnetotail twisting and IMF rotations: a systematic MHD simulation study

A. Kullen[1] and P. Janhunen[2]

[1]Alfvén Laboratory, Royal Institute of Technology, Stockholm
[2]Geophysical Research, Finnish Meteorological Institute, Helsinki

Abstract

We investigate with the help of a magnetohydrodynamic (MHD) model how the large-scale topology of the magnetosphere develops for a constant interplanetary magnetic field (IMF) with different IMF clock angles and for an IMF B_y sign change during northward IMF. A detailed examination of the topological changes in the tail and the ionosphere for different IMF conditions shows a good agreement with observational results.

The MHD simulations for different constant IMF clock angle cases show the expected field-line bending and tail twisting for nonzero IMF B_y. The tail becomes longer and at its tailward end stronger twisted for IMF $B_z > |B_y|$ than for IMF $B_z < |B_y|$. The field lines originating in the high-latitude flank of the far-tail plasma sheet map into the near-Earth tail lobes and to a strongly poleward displaced polar cap boundary. A comparison with observations suggests that an oval-aligned arc may occur on the high-latitude part of the polar cap boundary.

An IMF B_y sign change causes large deformations of the tail. After the IMF B_y flip the near-Earth and far-tail plasma sheet regions are oppositely twisted which causes in the near-Earth tail a bifurcation of the closed field line region that moves from one flank to the other. The bifurcated part of the closed field line region maps to a bridge of closed field lines moving over the entire polar cap. This moving bridge may be interpreted as the mapped region of a moving transpolar arc. Based on earlier observations, such a type of polar arcs are expected to occur after an IMF B_y sign change.

1 Introduction

The structure of the magnetosphere is strongly controlled by the direction of the interplanetary magnetic field (IMF). Especially the north-south component of the IMF but also the dawn-dusk component of the IMF influence the auroral precipitation pattern in the ionosphere and the large-scale topology of the magnetotail.

1.1 IMF B_y and B_z effects on the auroral precipitation pattern

It is well known that the polar cap expands during southward IMF conditions and contracts during northward IMF. Makita et al. (1988) showed that the thickness of the auroral oval increases and the size of the polar cap decreases with the strength of northward IMF. Polar auroral arcs (auroral arcs occurring poleward of the auroral oval) are a common phenomenon occurring during northward IMF (Valladares et al., 1994, and references therein). A recent statistical study by Kullen et al. (2002) about the dependence of large-scale polar arcs on the IMF direction distinguishes between five types of polar arcs which are shown to each be related to a characteristic combination of solar wind parameters.

The results show that those polar arcs occurring after 1-2 hours of nearly constant IMF with a positive IMF B_z and a nonzero IMF B_y component are always static polar arcs near one oval side (*oval-aligned arcs*). Oval-aligned arcs occur for a broad range of time spans. In average, they last for 2 hours. Polar arcs moving from one oval side to the other (*moving arcs*) can in most cases be related to a large-scale sign change of IMF B_y which takes place up to one hour before the arc's appearance. Moving arcs are usually *transpolar arcs*, connecting the nightside auroral oval with the dayside one. IMF B_z is predominantly positive one to two hours before and during a moving arc event. Moving arcs last between one and four hours, unless a large substorm occurs or the IMF changes to a persistently southward orientation. Such conditions lead to the disappearance of all types of polar auroral arcs. There exist other polar arc formations that have hardly been reported in literature: Immediately after an IMF B_z sign change often a short-lived polar arc occurs which bends into the polar cap with the anti-sunward end fixed to the oval boundary (*bending arc*). In rare cases, one single arc rises from the nightside oval boundary towards noon (*midnight arc*). This type of arc always appears at the very end of a substorm recovery phase. Other polar arc events are more complicated and involve three or more arcs separating from the oval-sides or the nightside oval boundary (*multiple arc events*).

The location of polar arcs is strongly dependent on the sign of IMF B_y. A statistical study about polar cap size and location during northward IMF by Elphinstone et al. (1990) shows that the location of polar arcs is strongly correlated to the IMF B_y component while the main oval keeps its circular shape. Most dawnside oval-aligned arcs occur for negative IMF B_y and all duskside arcs occur for positive IMF B_y. Moving polar arcs have been found to separate from the

dawn (dusk) side of the oval after an IMF B_y sign change from negative to positive (positive to negative) (Cumnock et al., 1997; Chang et al., 1998). The statistics of Kullen et al. (2002) confirms these results: In the northern hemisphere, all arc types including a poleward motion (moving and bending arcs) move toward the side of the oval pointed at by IMF B_y, whereas the non-moving arcs (oval-aligned and midnight arcs) are located at that side of the oval from the very beginning.

1.2 Polar arc models

As large-scale polar auroral arcs are commonly believed to have their source region in the tail plasma sheet (Frank and Craven, 1988), they probably lie on closed field lines. The occurrence of closed field lines poleward of the main auroral oval has to be addressed by any model explaining large-scale polar arcs.

A model, first proposed by Meng (1981), interprets polar arcs occurring during nonzero IMF B_y as the poleward boundary of an expanded auroral oval. A highly contracted polar cap occurs typically during strongly northward IMF. A further poleward displacement of the polar cap boundary on one oval side is caused by a twisting of the tail plasma sheet (Cowley, 1981; Kullen and Blomberg, 1996). A twist of the magnetotail is well-known to be connected to the IMF B_y component (Kaymaz et al., 1994, and references therein). The hypothesis of a polar arc being the poleward part of the auroral oval suits best as an explanation for oval-aligned arcs as these are static arcs that are often not much displaced from the oval boundary.

Moving polar arcs are during part of their life time located in the middle of the polar cap near the noon-midnight meridian. It has been suggested by several authors (e.g., Kan and Burke, 1985; Frank et al., 1986; Chang et al., 1998) that during such an event the magnetotail plasma sheet is bifurcated, i.e., a part of the plasma sheet extends to very high-latitudes, separating the lobes into a dawn and a duskward part. Huang et al. (1989) suggested that filamentary extensions of the plasma sheet may reach into the lobes.

Kullen (2000) proposed a model that does not include a plasma sheet bifurcation. Instead, it is suggested that the evolution of a moving arc may be related to a rotation of the magnetotail twist which is initiated by an IMF B_y sign change. To test this idea, the T89 (Tsyganenko, 1989) model has been modified in such a way that the near-Earth and the far-tail regions are oppositely twisted and for each time step the twist rotation is located further tailward. Mapping from the tail current sheet to the ionosphere results in a bar of closed field lines separating from the main oval and moving poleward for a tailward propagation of the tail twist rotation. This bar of closed field lines is interpreted as the mapped region of a moving polar arc. The model polar arc disappears when the rotation of the tail is completed and the entire tail has returned to a topology typical for uniform nonzero IMF B_y. Varying the input parameters in the model indicates that the duration of a polar arc event is dependent on the magnitude of IMF B_y but not on the spatial extent of the IMF B_y sign reversal region. A broad dawn-duskward extension of the model polar arc appears for

a high IMF B_y magnitude and/or a long sign reversal period. An important result is the finding that although the plasma sheet (as identified from the B^2 isocontour lines) is ad hoc forced to keep a butterfly shape, the region of closed field lines is bifurcated in the near-Earth tail. The reason for the bifurcation is that closed field lines which have their turning point near the high-latitude flank of the far-tail plasma sheet, map high up into the lobes of the oppositely twisted near-Earth tail (for a 3D-schematic of the resulting tail topology, see Fig. 2b in Kullen et al. (2002)). The Kullen (2000) polar arc model is entirely based on the assumption that an IMF B_y sign change causes first the near-Earth tail and later the far tail to respond such that in an intermediate state the near-Earth and the far-tail regions are oppositely twisted. Data and/or magnetohydrodynamic (MHD) studies are necessary to investigate the correctness of this assumption.

A polar arc model that became widely accepted in the recent years has been developed by Newell et al. (1997) and Chang et al. (1998). It explains the creation of a new region of open field lines dawnward (or duskward) of the main polar cap near noon with an abrupt jump of the dayside merging line. It is proposed that this jump is caused by an IMF B_z or IMF B_y sign change. The closed field line bridge in the ionosphere between the old and the new region of open field lines is supposed to be the location where a polar arc occurs. Chang et al. (1998) predicted that several sign changes would be necessary for a polar arc to resist for a longer time. However, observations show that long-lasting moving polar arcs exist where no further IMF sign changes occurs after a large-scale IMF B_y sign reversal (Cumnock et al., 2002). As the model includes the immediate occurrence of a polar arc after an IMF sign change and a short lifetime of the arc in case no further IMF variations occur, we believe that this model fits better as an explanation for bending arcs than for the long-lasting moving arcs.

Many models from the 1980's assume that transpolar arcs typically grow from the nightside oval towards noon (e.g., Kan and Burke, 1985; Frank et al., 1986). However, a large number of observational papers show that most arcs separate from the dawn- or duskside of the oval (e.g., Chang et al., 1998). Single midnight arcs are extremely rare events and occur only after a period of predominantly strong northward IMF at the end of a substorm recovery phase (Kullen et al., 2002). They all develop from a strongly contracted poleward boundary of the nightside auroral oval. In the midnight arc model by Rezhenov (1995) precisely these characteristics are suggested as preconditions for midnight arcs to occur. He suggests that an interchange instability may occur at the tailward end of a short plasma sheet that causes a tongue of plasma to move tailward. The tailward moving plasma sheet tongue is supposed to map to a closed field line bar that grows from midnight to noon in the polar cap.

1.3 IMF B_y and B_z effects on the magnetotail: Observations

The effect of the IMF B_y component on the magnetotail consists mainly in a dawn-duskward bending of the magnetic field lines and a twist of the entire tail. The field-line bending is connected to

an extra B_y field that extends over the entire tail. As this extra B_y term has the same direction and is proportional to the IMF B_y component, it has been often referred to as 'IMF B_y penetration field', which indicates a physical process that has not been proven to take place in the magnetosphere (in an ideal MHD fluid, often assumed in solar and magnetospheric plasmas, a mixing of field lines cannot occur). For simplicity, we use this term as well, but only as a description of the rate of the extra B_y term occurring in the tail.

From numerous observations it is known that the IMF B_y penetration field is nonuniform. The average B_y penetration in the tail lies around 10 to 14 percent of the total IMF B_y magnitude (e.g., Fairfield et al., 1979; Cowley, 1981; Kaymaz et al., 1994). A statistical study of the mid-tail region by Kaymaz et al. (1994) confirms earlier findings that the IMF B_y penetration is much stronger in the plasma sheet than in the lobes. They found in average 9 and 26 percent penetration in the lobes and in the plasma sheet, respectively. A maximum penetration of 35 percent was discovered near the plasma sheet flanks. The strongest IMF B_y penetration into the tail seems to occur at the neutral sheet (defined as the location of the magnetic field line reversal from tailward to earthward, i.e., where B_x changes sign). Lui (1986) and Sergeev (1987) reported penetration rates of 50 and 60 percent of the total IMF B_y field, Borovsky et al. (1998) found an even higher penetration rate (76%) for cases with 30 minutes or more constant IMF B_y before the neutral sheet crossing of the satellite. All results so far mentioned refer to a tail region of about 20 to 30 R_E downtail from the Earth.

In numerous data studies, a twisting of the current sheet by 6 to 18 degrees for nonzero IMF B_y was found (e.g., Sibeck et al., 1986; Tsyganenko, 1998; Kaymaz et al., 1994). Kaymaz et al. (1994) showed that in average the current sheet is more twisted near the flanks than in the central tail, Tsyganenko (1998) found the tail twist to increase with the distance from the Earth. MacWan (1992) reported twists over 90 degrees in the distant magnetotail ($x = 115-220 R_E$). In a statistical magnetotail study by Owen et al. (1995) much lower twists are found on average but according to the authors large twists of about 50-60 degrees are possible in individual cases. One major result of the study by Owen et al. (1995) is a correlation between the degree of plasma sheet twisting and the sign of IMF B_z. For northward IMF, plasma sheet twists are on average twice (6^0 for $B_y < 0$ and 12^0 for $B_y > 0$) those for southward IMF (13^0 for $B_y < 0$ and 24^0 for $B_y > 0$). The observation of a high degree of twisting for low geomagnetic activity is probably due to the connection between quiet conditions and northward IMF.

It seems hard to define the length of the closed field line region from observations. MacWan (1992) reported that only for dynamic topology changes the region of closed field lines reaches as far downtail as the region of his measurements. In the static cases the last closed field lines are earthward of $115 - 220 R_E$.

1.4 IMF B_y and B_z effects on the magnetosphere: MHD model results

Many MHD simulations have been performed to study the magnetospheric topology during purely northward IMF. In many MHD models the tail becomes completely closed for persistently northward IMF (e.g., Fedder and Lyon, 1995; Song et al., 1999). In this case, the tail length has been found to be inversely proportional to the strength of positive IMF B_z (e.g., Song et al., 1999, and references therein). When the tail is not closed, it contains open field lines connected with the IMF and it has no defined length. Instead, the tailward extension of the closed field line region is studied. Gombosi et al. (1998) using the same MHD model as Song et al. (1999) found that the closed field line region extends to 120-140 R_E during the first hour after an IMF B_z northward turning and then shrinks to a constant length of about 60 R_E. They concluded that a very long closed field line region for northward IMF seems only to appear as a transient phenomenon. Raeder et al. (1995) reported for purely northward IMF a much shorter closed field line region of about $20 - 40 R_E$ near the x-axis but stretching further tailward near the flanks. The plasma population remains apparently the same earthward and tailward of the last closed field line (Song et al., 1999). The dawn-dusk diameter of the far-tail lobes depends on IMF B_z, being more narrow during northward IMF than during southward IMF (Raeder et al., 1995).

The IMF B_y effects on the magnetotail as found from observations appear in many MHD simulations. The first simulation results focusing on IMF B_y effects were published by Brecht et al. (1981). A run with constant south-dawnward IMF input was presented which shows a twist of the entire tail and an IMF B_y penetration into the neutral sheet. Kaymaz et al. (1995) used the Fedder-Lyon MHD model (Fedder and Lyon, 1995) to compare their statistical results (Kaymaz et al., 1994) with MHD simulations. Both the IMF B_y penetration and the twisting of the current sheet in the simulation are in good agreement with the observations. Simulations for constant IMF input presented by Ogino (1986) show clearly (although not discussed in further detail by the authors) that the degree of plasma sheet twisting during nonzero IMF B_y is dependent on the sign of IMF B_z.

There exist several papers presenting MHD simulation results for a changing IMF clock angle θ ($\theta = 0^o$ for northward, $\theta = 90^o$ for dawnward or duskward, $\theta = 180^o$ for southward IMF). Berchem et al. (1998) using the code described by Raeder et al. (1995) compared satellite data from the tail during a period of changing IMF with simulation results. In their simulations the closed field line region is long and the plasma sheet is highly twisted for small IMF clock angles only, as expected from the statistical study by Owen et al. (1995). The northern and southern open field line regions are for IMF $|B_y| > B_z$ well separated from each other in the far-tail yz-plane but for IMF $|B_y| < B_z$ more close to each other. A detailed study about a changing IMF clock angle is presented by Walker et al. (1999) using the MHD code developed by Ogino et al. (1992). They found, like Berchem et al. (1998), the tail twisting to be stronger for northward than for southward IMF. Moreover, they showed that the far tail is more strongly twisted than the near-Earth tail, in

agreement with Tsyganenko's (1998) statistical results. In the simulations by Walker et al. (1999) the near-Earth tail responds first on an IMF change. The tail changes its twist first at the flanks, then in the central tail. A magnetopause reconfiguration in response to an IMF change takes up to 15 minutes, the plasma sheet twist occurs 45-60 minutes after an IMF change reaches the dayside magnetopause. The near-Earth neutral line (NENL) at x=20 R_E disappears within 45 minutes after a northward turning of the IMF and the region of closed field lines increases in length for a decreasing IMF clock angle. (Slinker et al., 2001) compared polar cap observations by the Eureka dawn-dusk meridian scanning photometer (MSP) with simulation results of the Fedder-Lyon MHD model for an IMF B_y sign change during mainly northward IMF. Their results basically confirm the model suggested by Kullen (2000). In the simulations a region of closed field lines moves over the entire polar cap while the tail is changing its twist from one direction to the other. The closed field line bridge in the model polar cap corresponds to a dawn-duskward moving strip of auroral emissions seen in the MSP which is most likely the signature of a large-scale moving polar arc.

1.5 IMF B_y and B_z effects on the magnetosphere: Theories

Russell (1972) was first to predict a twisting of the magnetotail caused by the asymmetry of the reconnection between solar wind and magnetosphere during non-zero IMF B_y. He even predicted a stronger twisting during northward IMF due to possible lobe reconnection.

Cowley (1981) argued in the same way. He proposed that the asymmetric addition of magnetic flux to the tail lobes from dayside reconnection during non-zero IMF B_y conditions may result in a penetration of the IMF B_y into the tail. With a simple model he showed how an assumed B_y penetration field that decreases towards lower latitudes leads to a twisting of the tail lobe field around the x-axis. Neither the occurrence of the IMF B_y penetration field in the region of closed field lines nor the plasma sheet twisting are explained in this paper, although Cowley mentioned both effects to be probable to occur.

Owen et al. (1995) proposed, the stronger tail twist during northward than during southward IMF is associated with lobe reconnection. Open field lines, reconnected poleward of the northern cusp with the IMF map to the solar wind field lines south of the equatorial plane where they are frozen into the solar wind flow. Hence, these open field lines exert a much stronger torque on the tail than in the southward case. During southward IMF the field lines reconnect at the dayside magnetopause and are bent into the direction of IMF B_y, but remain in the same hemisphere. The field-line topology for a 45 degree IMF clock angle has been confirmed in MHD simulations by Tanaka (1999).

From these models, it remains unclear how the twisting of the open field line regions causes a twisting of the tail plasma sheet, and how the IMF B_y penetration field occurs in the region of closed field lines, being even stronger than in the lobes.

The non-uniformity of the B_y penetration field has been addressed by Voigt and Hilmer (1987).

They showed with a 2D-MHD simulation that assuming a constant background B_y penetration field inside the tail (which is not further explained), an increase of the IMF penetration in the plasma sheet appears to balance the high thermal plasma pressure in this region.

1.6 The goal of this study

The main focus of this study lies on the IMF B_y and B_z dependent large scale topological structure of the magnetotail and its connection to the shape of the polar cap boundary as well as on the possible occurrence of polar arcs. Motivated by observations that constant northward IMF with a nonzero IMF B_y component leads to a strong twisting of the tail plasma sheet and is a favorable condition for oval-aligned arcs to occur, we investigate, with the help of the GUMICS-4 MHD code by Janhunen (1996), how the tail and polar cap boundary respond to different IMF clock angles. The response of the model magnetosphere on an IMF B_y sign change is studied to find out about the possible appearance of a moving polar arc (as expected from observations) and the possible rotation of the tail twist (as assumed in the Kullen (2000) polar arc model).

2 Results

2.1 The MHD simulations

The GUMICS-4 code used in this study needs as input parameters the solar wind speed, solar wind pressure, IMF B_y, IMF B_z and the Earth dipolar tilt. All runs start with a dipole in a uniform low-density plasma. The solar wind enters the dayside front of the simulation box at the first minute of the run. The simulation box is 32 R_E long on the dayside and stretches to 224 R_E on the tailward side. In dawn-duskward and north-southward direction the box is 128 R_E wide. In the code all physical quantities are calculated with time steps of less than a second for a mesh containing about 130000 grid cells. An adapted grid mesh size is used which depends on the gradients of the physical quantities. Further details of the MHD code can be found in Janhunen (1996), a critical discussion of its advantages and limitations are described by Janhunen and Palmroth (2001). In all runs discussed in this study a solar wind speed of 400 km/s and a solar wind dynamic pressure of 2 nPa have been chosen. The Earth dipole tilt is set to zero to avoid wrapping of the tail plasma sheet. As for this study only large-scale features are of interest, the physical quantities are examined in time intervals of 5 minutes and spatial distances of 1 R_E only. The results presented here are accurate only within these limits.

To examine the steady state magnetosphere during constant IMF with nonzero IMF B_y MHD runs have been performed for two hours constant 10, 45, 80, and 100 degree IMF clock angles with negative IMF B_y and a total IMF magnitude of 5.1 nT. The IMF clock angle θ is defined here as the angle between the IMF vector in the yz-plane and the positive z-axis ranging from 0° for pure northward to 180° for pure southward IMF. For a constant solar wind input with the above given

IMF clock angles the model magnetosphere reaches an equilibrium state after approximately one hour. The runs are continued for one additional hour to rule out any influence of a transitional change on the magnetospheric topology. Runs with clock angles higher than 100 degrees are not performed, as substorms may occur which is not the subject of our study. As the highest IMF clock angle input in our simulations is $\theta = 100°$, the expressions 'large clock angle' and 'small clock angle' are further on used to describe IMF directions with $|B_y| > B_z$ and $|B_y| < B_z$, respectively. For the IMF B_y sign-change study two runs have been performed with constant positive IMF B_z ($B_z = 5$ nT) during the entire time and IMF B_y negative ($B_y = -5$ nT) before and positive ($B_y = 5$ nT) after an IMF B_y sign change which starts after two hours constant IMF at the dayside boundary of the simulation box. In each case, the IMF is kept constant for an additional two hours following the sign change. The difference between the two runs is the speed of the IMF B_y sign change. In the first case, IMF B_y changes sign within two minutes, in the second case a slow, linear change within one hour is enforced.

2.2 MHD results for constant IMF

Figure 1 presents the state of the ionosphere and magnetotail after two hours constant solar wind input. The columns (from left to right) show the simulation results for constant IMF clock angles of 100, 80, 45 and 10 degrees. In the first row the northern ionosphere is shown with the open/closed field line boundary (light blue dotted lines) overlaid on a plot showing the upward (blue) and downward (red) field-aligned current regions. The second to last rows consist of plasma pressure isocontour plots (in arbitrary units) for tail cross sections at $x = -10, x = -30, x = -60$ and $x = -120\mathrm{R_E}$. The color scale reaches from blue to red representing lowest to highest pressure. Overlaid on these plots are the regions of open field lines (blue dots) and closed field lines (pink dots). Figure 2 shows the same type of plots for the fast IMF B_y sign change with a sign reversal within 2 minutes from negative to positive IMF B_y during constant, positive IMF B_z. The columns (from left to right) represent the state of the magnetosphere 6 minutes before, 7 minutes after, 22 minutes after and 37 minutes after the center of the IMF B_y sign-change region ($B_y = 0$) reached the dayside magnetopause at $x = 10\mathrm{R_E}$. In deviation from Fig. 1 the last row of Fig. 2 shows tail cross sections at $x = -90\mathrm{R_E}$. The main results of this figure are described in the next subsection. Here, the first column of Fig. 2 is compared to column 3 of Fig. 1 to find out about a possible difference between strong (7.1 nT) and average IMF (5.1 nT) for the same IMF clock angle of 45°.

While the field-aligned current (FAC) pattern is for all MHD runs nearly unchanged, the polar cap boundary (here defined as the boundary between open and closed field lines) differs much for the different IMF clock angle runs. The polar cap is more contracted for small IMF clock angles and the dawnside polar cap boundary is for all clock angles displaced poleward as expected in the northern hemisphere during negative IMF B_y. The polar cap boundary of the southern hemisphere (not shown here) is anti-symmetrically shaped with respect to the noon-midnight meridian, the

poleward displacement occurs there on the dusk side of the polar cap.

As expected from the highly contracted polar cap for small clock angles, the closed field line region extends in the magnetotail to much higher latitudes for small IMF clock angles than for large clock angles. The tailward extension of the closed field line region depends on the IMF clock angle as well. Table 1 gives the tailward length of the closed field line region (CFR length) for each IMF clock angle. Only for small IMF clock angles does the closed field line region extend to the far tail. Comparing the 45° clock angle cases with weak and strong IMF magnitude, the closed field line region is slightly shorter in the latter case. The open/closed field line boundary overlaps approximately with the plasma sheet boundary for all but the 10° IMF clock angle case. In the latter case the region of closed field lines extends high into the tail lobes.

The region of open field lines outside the magnetotail is directed along the IMF clock angle axis but with a slight clockwise displacement from it (looking tailward). Inside the near-Earth tail the open field line region surrounds the closed field line region. Far downtail the closed field lines have disappeared and for large IMF clock angles the northern and southern wings of the open field line regions are much displaced from in each other in dawn-dusk direction such that they hardly overlap with the lobes.

As expected for negative IMF B_y the plasma sheet (high pressure region inside the tail) is twisted in a clockwise direction around the x-axis (looking tailward) for each of the constant IMF runs. Only for small IMF clock angles and/or high IMF magnitude the plasma sheet twist is strong and extends over the entire tail cross section. For large IMF clock angles the plasma sheet twists only near the flanks. The twisting increases clearly with the distance from the Earth for the 45 and 10 degrees clock angle cases. For 80 and 100 degrees the plasma sheet is in the center of the far tail twisted in the opposite direction. For all but very small IMF clock angles a typical tail pressure morphology with lobes and plasma sheet occurs even in regions tailward of the last closed field line. The plasma sheet thickness and the dawn-duskward extension of the lobes are dependent on the IMF clock angle as well. In the near-Earth tail the plasma sheet is thick only for small IMF clock angles. In the far tail the dawn-duskward width of the lobes decreases with decreasing IMF clock angles.

Figure 3 shows the IMF B_y penetration field inside and around the magnetotail at $x = -10\mathrm{R_E}$ (left column) and $x = -60\mathrm{R_E}$ (right column) for the simulation runs with an IMF clock angle of 100° (upper row) and 10° degrees (lower row). To extract the tail magnetic field, the along the xz-plane mirrored $B_y B_z$ vectors have been subtracted from the original $B_y B_z$ vector field and then been divided by two. Assuming the tail magnetic field for zero IMF B_y is completely symmetric with respect to the xz-plane, this gives the pure IMF penetration field. For both IMF clock angle cases the IMF is slightly draped around the magnetopause. A large part of the field penetrates the magnetosphere. In the near-Earth tail the penetration field is strong near the equatorial plane and weak at high latitudes (80% penetration for $\theta = 100°$ and 110% for $\theta = 100°$ at $z = 0\mathrm{R_E}$).

This structure is preserved to around $x = -45\mathrm{R_E}$. Further downtail, the penetration field weakens and is more uniformly distributed. At the tailward end of the simulation box (not shown here) the penetration field is weaker than IMF B_y for all IMF clock angle runs.

Figure 4 gives an equatorial view on the magnetosphere. In the left column of Fig. 4 the $B_x B_y$ vector components are plotted down to a distance of 4 $\mathrm{R_E}$ from the Earth. In case IMF $B_y = 0$, the B-field in the equatorial plane of the magnetosphere is expected to have only a z-component. Hence, the $B_x B_y$ plots of Fig. 4 show the IMF B_y penetration into the equatorial plane of the tail. The first and second plot correspond to the IMF clock angle cases of 100° and 10°, respectively. Figure 5 contains the same type of plots for the sudden IMF B_y sign change. It shows the $B_x B_y$ vector component plots 6 minutes before (top), 7 minutes after (middle) and 22 minutes after (bottom) the IMF B_y sign reversal reached the dayside magnetopause. The main results for the IMF B_y sign-change case are described in the next subsection. Here, only the first plot is addressed, corresponding to a constant 45° IMF run for 7.1 nT. In the format shown here, its deviation to the 45° case with 5.1 nT is negligible such that it illustrates even the results of the weak 45° case fairly well.

The $B_x B_y$ vector plots for the different IMF clock angles have several features in common. The IMF B_y field is strongly compressed near the dayside magnetopause and drapes around the magnetosphere. In the region closest to the Earth which is dominated by the Earth dipole field ($|x| < 8\mathrm{R_E}$) a nearly uniform B_y penetration field is found having approximately the same magnitude as the IMF itself. Tailward of this region, the $B_x B_y$ vector components have a sunward draping pattern centered around the x-axis. The draping pattern reduces tailward such that in the very far tail the $B_x B_y$ component lines are directed in the dusk-dawn direction. The draping inside the tail reflects the twisting of the plasma sheet seen in Fig. 1, first and last column, and Fig. 2, first column. A positive (negative) component of B_x in the equatorial plane causes a southward (northward) displacement of the current sheet (surface containing the turning points of the closed field lines) from the equatorial plane. The stronger draping for the small IMF clock angle is connected to a stronger and more uniform twist around the x-axis, the tailward draping downtail of 25 $\mathrm{R_E}$ near the x-axis for the 100° IMF clock angle case corresponds to the oppositely twisted plasma sheet (Fig. 1, column 1, row 4).

2.3 MHD results for an IMF B_y sign change

As mentioned above, Fig. 2 illustrates the change of the polar cap and the tail for the fast IMF B_y sign change. The plots show the state of the magnetosphere when the IMF B_y sign reversal starts at the dayside boundary of the simulation box, and 5, 20 and 35 minutes, respectively, after the first significant change of the polar cap boundary is seen. The ionosphere plots in the first row of Fig. 2 show that the polar cap boundary changes drastically after an IMF B_y sign change. A bridge of closed field lines starts to develop at the dawn/noon edge of the polar cap boundary and

moves within 50 minutes from dawn to dusk over the entire polar cap of the northern hemisphere. In the southern hemisphere (not shown here) an identical bridge starts to appear on the duskside and moves then in the opposite direction until the dawnside polar cap boundary is reached. The bridge of closed field lines inside the northern (southern) polar cap is connected to a finger of closed field lines in the tail bifurcating the northern (southern) tail lobe. The fingers of closed field lines in the tail move into the same direction as the bridge of closed field lines in the polar cap of the corresponding hemisphere.

Figure 6 shows the tailward extension of the closed field line region and the location of the IMF B_y sign reversal regions versus time for the slow (thin line and dark grey region) and the fast (thick line and light grey region) sign-change runs. The time axis is given in minutes after the center of the IMF B_y sign reversal has passed the dayside magnetopause. The time intervals during which a bifurcation of the polar cap occurs are marked with dotted lines. As can be seen from Fig. 6 the length of the closed field line region varies much during the tailward propagation of an IMF B_y sign reversal. As long as the center of the IMF B_y sign-change region has not passed the tailward end of the closed field line region the closed field line region grows rapidly beyond $x = -100\mathrm{R_E}$ in both sign-change cases. The closed field line region remains extremely stretched for another 25 minutes until it suddenly returns to its original length. The polar cap bifurcation starts in both sign-change cases some minutes after the center of the IMF B_y sign reversal has passed the dayside magnetopause and ends when the far tail part of the closed field line region disappears and the tail returns to its original length.

The process that leads to the return into a ground state for constant duskward IMF B_y with a short closed field line region is rather complicated. This is illustrated in Figure 7 and Figure 8. In Fig. 7 the open (grey) and closed field line regions (black) are shown in the xy-plane at $z = 0\mathrm{R_E}$ (left column) and $z = 15\mathrm{R_E}$ (right column) for different points of time after the IMF B_y sign-change region center has passed the dayside magnetopause. The first four time points correspond to the time points shown in Fig. 1 and 2. The last two time points are chosen just before and just after the polar cap bridge disappears. Fig. 8 shows the magnetic field line topology in 3D for the fast IMF B_y sign change run for the same run and same time points as in Fig. 7.

The left column of Fig. 7 shows that, when the tail has reached its maximum length (at 22 min), the tailward part of the closed field line region becomes separated from the earthward part in the equatorial plane. The far tail is connected to the northern (southern) ionosphere only by a thin, tail-aligned bridge of closed field lines moving from dawn to dusk (dusk to dawn) in the northern (southern) high latitude lobe (Fig. 7, right column). This bridge of far tail closed field lines maps to the model polar arcs (not shown here). The tailward closed field line part reduces in length and width until it disappears together with the closed field line bifurcation in the ionosphere and the tail. The disappearance is not enforced by the limited length of the simulation box. The IMF B_y sign reversal is at that time point still located earthward of the nightside simulation box boundary

(see Fig. 6, fast sign-change case).

It is difficult to define reconnection in an MHD simulation. However, studying the field line topology in detail, the location of the separation region between open, closed and solar wind field lines can be found. Before the sign change has reached the magnetosphere (Fig. 8, first plot), the separation region is located at the high-latitude lobes, poleward of the cusps, displaced toward dawn (dusk) in the northern (southern) hemisphere, as expected for dawnward IMF with a northward B_z component. Immediately after the IMF B_y sign change took place, the reconnection region moves from the dawn to the dusk lobe in the northern hemisphere and in opposite direction in the southern hemisphere lobes. New regions of open field lines appear on the dusk (dawn) flanks of the northern (southern) tail. While the closed field line region extends further and further tailward, the new regions of open field lines increase and the old, tailward regions of open field lines decrease (Fig 7., left column). Interestingly, both, the new and the old open field lines reconnect with the solar wind field on the northern dawn (southern dusk) high-latitude lobes. When the closed field line region has reached its maximum length, the field line topology in the mid-tail becomes extremely complicated (Fig. 8, right column). Solar wind field lines occur now in the mid-tail near the x-axis, separated from the near-Earth and far tail closed field line regions by open field lines. The open field lines earthward and tailward of the solar wind field lines in the mid-tail as well as the old open field lines tailward of the last closed field line are all associated with the same high-latitude lobe reconnection region. The region of solar wind field lines in the mid-tail increases at the expense of the decreasing tailward closed field line region. After the last closed field line has disappeared, the tail returns to a steady state case for duskward IMF B_y. The last plot of Figure 8 shows the field line distribution just after the last closed field line has disappeared in the far tail, where the tailward solar wind field lines are still strongly deformed.

In Fig. 9 B_yB_z-difference vector plots are shown for the fast IMF B_y sign-change case in tail cross sections at $x = -10, -30, -60$ and $-120\mathrm{R_E}$ 22 minutes after the IMF B_y sign-change region has passed the dayside magnetopause. The difference vector plots are done in the same way as those of Fig. 3 showing the B_y penetration field inside the tail. As can be seen from Fig. 5 and Fig. 9 the location of the sign-change center ($B_y = 0$) is situated like a sunward pointing cone around the x-axis. Outside the cone, the magnetic field points toward dusk, in direction of positive IMF B_y. Inside the cone, the B_y penetration field is still negative and has a distribution similar to the B_y penetration field of the constant IMF $B_y < 0$ cases (see Fig. 3). The penetration field is stronger near the plasma sheet than in the lobes. The non-uniformity of the penetration field inside the tail decreases with the distance from the Earth.

The B_xB_y-vector component plots in Fig. 5 illustrate the propagation of the IMF B_y sign reversal in the equatorial plane. The cone of zero B_y moves tailward with time and becomes more and more narrow the further downtail it propagates. This indicates that outside the tail the sign reversal moves tailward with solar wind speed, toward the tail center it is more and more delayed.

Comparing the last two $B_x B_y$-vector plots with the first plot, it can be seen that the location of the sign-change region center ($B_y = 0$) in the equatorial plane is quite similar to the draping pattern of the $B_x B_y$-vector component lines in the constant IMF B_y case.

Important results are found from comparing the shape of the plasma sheet with the shape of the closed field line region inside the model tail. In contrary to the closed field line region the plasma sheet does not bifurcate the lobes during the tailward propagation of the IMF B_y sign change reversal. It changes its IMF B_y induced twist first in the near Earth and then in the far tail such that in an intermediate state the near-Earth and far-tail regions are oppositely twisted. The plasma sheet resembles during times a horizontal 'S' as the twist reversal in one tail cross section starts at the flanks and then propagates to the tail center. In one tail cross section it takes (dependent on the distance from the Earth) 15 to 45 minutes until the twist rotation is completed. The bifurcation of the closed field line region disappears as soon as the entire tail plasma sheet has changed its twist.

In Fig. 10 a few plots of the slow (one hour) IMF B_y sign change are shown. The first row shows the northern polar cap boundary and the second row the tail cross sections at $x = -30\mathrm{R_E}$, 13 minutes (left column), 28 minutes (middle column) and 43 minutes (right column) after the center of the IMF B_y sign reversal ($B_y = 0$) reached the dayside magnetopause. The time points are chosen such that the first (second, third) column gives the state of the magnetosphere five minutes (20 min, 35 min) after the start time of the polar cap bifurcation. This makes the plots comparable to those of Fig. 2.

The main difference between the fast and slow IMF B_y sign-change runs are the width of the closed field line bridge in the polar cap and the width of the closed field line fingers bifurcating the tail. The location of the bifurcation, the lifetime of the dawn-duskward moving bridge and the topological change of the tail plasma sheet are qualitatively the same for the slow and for the fast IMF B_y sign-change runs. Even in the slow IMF B_y sign-change case the plasma sheet starts to change its twist in the near-Earth tail and at the flanks, it does not bifurcate such that the plasma sheet boundary does not overlap with the bifurcated closed field line region in the tail. The tailward increase and decrease of the closed field line region develops qualitatively in the same way as in the fast IMF B_y sign change case. Even in the slow sign-change case the near-Earth tail is separated from the far-tail region in the equatorial plane during the last 15 minutes a bifurcation of the closed field line region in tail and ionosphere is seen. However, as shown in Fig. 6 the tail grows faster and stretches further tailward than in the fast IMF B_y sign change run.

3 Discussion

3.1 The constant IMF clock angle cases: comparison with earlier results

The general topological changes inside the model magnetosphere induced by constant IMF B_y are confirmed by observations. This includes the partial IMF B_y penetration into the tail with a maximum penetration rate along the neutral sheet (Lui, 1986; Borovsky et al., 1998) the twisting of the tail plasma sheet with the strongest twist near the flanks (Kaymaz et al., 1994), the tailward increase of the twisting (Tsyganenko, 1998) and the dawn-dusk displacement of the open/closed field line boundary in the ionosphere (Cowley, 1981). These IMF B_y effects have been reported from MHD studies as well (Kaymaz and Siscoe, 1998; Brecht, 1981). The preservation of the magnetospheric plasma structure tailward of the last closed field line has been seen in the simulations by Song et al. (1999). Some of the IMF clock angle dependent changes in the magnetospheric topology that are found in our simulations, have been indicated in data studies. The increase of the tail twisting and the decrease of the polar cap for small clock angles have been described in the statistical studies by Owen et al. (1995) and Makita et al. (1988), respectively. Owen et al. (1995) statistical results of a concave form of the plasma sheet in the far tail may be an indication for the oppositely twisted far-tail center occurring for IMF clock angles around 90° in our simulations as usually solar wind conditions are such that $|IMFB_y| > |IMFB_z|$. Other IMF clock angle effects are difficult to observe, they are so far only seen in MHD simulations such as a long closed field line region for small IMF clock angles (Walker et al., 1999) or small IMF magnitude (Song et al., 1999), the orientation of the open field lines in IMF direction (Fedder and Lyon, 1995), the IMF clock angle dependent dawn-duskward width of the far-tail lobes (Raeder et al., 1995) and the north-southward distance between the regions of open field lines in the far tail (Berchem et al., 1998).

The qualitative agreement between our simulation and earlier results is good. A quantitative comparison is more difficult. Both data studies and MHD studies report a variety of different values for, e.g., the length of the closed field line region, the degree of plasma sheet twisting and the IMF B_y penetration rate. Analyzing magnetotail data, it is difficult to determine in which region the measurements are taken as it takes a long time for a satellite to cross the magnetotail and IMF conditions may change rapidly. The Kaymaz et al. (1994) results of the average tail structure in the xy-plane of the mid-tail may be the most interesting ones as they are extracted from a large set of IMP-8 data which gives a nearly complete coverage of the tail and surrounding solar wind regions between $15\mathrm{R_E}$ and $45\mathrm{R_E}$. MHD models often have unrealistically short tail dimensions (e.g., the Fedder-Lyon MHD model). This may be the case for this code as well. Figure 11 shows the B_yB_z vector components of the total magnetic field in tail cross sections at $x = -10, -15$ and $-30\mathrm{R_E}$ after two hours run with a constant pure IMF B_y field of 5 nT. Comparing the model tail shown in Fig. 11 with the average observed tail structure around $33\mathrm{R_E}$ for comparable IMF

conditions (Kaymaz et al., 1994, Fig. 3c), the model tail resembles the mid-tail observations best for $x = -10\mathrm{R_E}$. Further downtail, the IMF dominates the tail structure much more than found by observations, indicating a too short model tail also in the present model.

The good agreement between observations, earlier MHD results and this study makes us confident about the significance of the new findings of this study: the relation between the closed field line region in the tail and the shape of the plasma sheet.

3.2 The IMF B_y sign-change cases: comparison with earlier results

The comparison between MHD simulation results with observations by Slinker et al. (2001) shows that moving polar arcs lie indeed on closed field lines, as expected from the finding that particles causing polar arcs origin in the tail plasma sheet (Frank et al., 1986). We therefore assume that in our simulations the bridge of closed field lines inside the polar cap can be regarded as the location where a polar arc may occur. For simplicity, the closed field line bridge is further on referred to as 'model polar arc'. The dawn to dusk motion of the model polar arc in the northern polar cap following an IMF B_y sign change from negative to positive during northward IMF is expected from observations Cumnock et al. (2002). Also the simultaneous occurrence of a polar arc in the southern hemisphere but with opposite motion is indicated in data results (Craven et al., 1991). Shape and life time of our model polar arcs are quite similar to the model arc shown by Slinker et al. (2001) although their run was done for a stronger and more varying IMF than our runs. Although a more sun-aligned and more homogeneous arc width than seen in the simulations may be expected (Frank et al., 1986), the arc shape is difficult to compare with observations as there exists a multitude of different moving polar arc shapes (Kullen et al., 2002). A large discrepancy between observations and MHD results is found for the life time of moving polar arcs. This is indicated already by Slinker et al. (2001). There, the MSP data shows an arc life time of at least two hours while the model arc persists only during 40 minutes. The statistical results by Kullen et al. (2002) show that moving polar arcs which cross the entire polar cap exist on average for two hours instead of the 50 minutes found in our model study. In single cases, polar arcs can even have life times of three to four hours (see the moving polar arc examples presented by Cumnock et al. (2002) and Kullen et al. (2002)).

The simulation results show a good agreement with the semi-analytical results by Kullen (2000). It confirms the assumption of an IMF B_y sign change causing first the near-Earth tail and then the far tail to change its twist such that in an intermediate state the near-Earth and the far tail are oppositely twisted. The main results of the Kullen model are in agreement with the MHD results. The poleward motion of the polar arc, the bifurcation of the closed field line region in the tail, its mapping to the polar arc in the ionosphere, and the non-bifurcation of the plasma sheet exist in both models. The Kullen model indicates that the width of the sign change region effects the nightside width of the polar arc but not its location. This is confirmed by the MHD simulations

as well. However, several IMF B_y sign change effects on the magnetosphere appear in the MHD simulations only. The variation of the closed field line region length does not show up in the Kullen (2000) model, as the used T89 model has an open tail without boundary. In the Kullen (2000) model the tail twist is a priori forced to change linearly between near-Earth and far tail. However, the MHD results show that the twist change starts at the flanks and moves within several tens of minutes into the center of the tail (Fig. 5). The polar arc of the MHD simulation stretching from the nightside to the dayside auroral oval and moving over the entire polar cap has a more realistic shape and location than the one presented in the Kullen (2000) model.

Chang et al.'s (1998), suggestion that an IMF B_y sign change may cause a new polar cap region at pre-noon (post-noon) for a sign change of IMF B_y from negative to positive (positive to negative) is confirmed by the simulation results. The dawn and duskward displacement of the lobe reconnection in the northern and southern hemisphere, respectively, changes soon after the IMF B_y sign change took place towards the other side of the noon-midnight meridian and is connected to a new polar cap region near noon. However, the dawn to dusk motion of the closed field line bridge in the ionosphere cannot be explained by the dayside reconnection site jump but occurs due to the rotation of the plasma sheet twist, as described by Kullen (2000).

Neither polar arc models, nor the Slinker et al. (2001) MHD results predict the occurrence of solar wind field lines in the mid-tail while parts of the closed field line region extend increasingly tailward. In the GUMICS-4 simulations the region of solar wind field lines inside the tail grows at the expense of the tailward closed field line region until it disappears. Further investigations would be necessary to find out, whether this is a common phenomenon associated with similar IMF configurations. It has to be pointed out, that this process appears at the end of the polar arc life time when the arc has already reached the other side of the polar cap and does neither influence the creation nor the dawn-duskward motion of the arc.

3.3 The possible occurrence of polar arcs on high-latitude closed field lines

The suggested appearance of oval-aligned arcs on the strongly polewardly displaced dawnside polar cap boundary in the 10° constant IMF case (with dawnward IMF B_y) is motivated by observations. Kullen et al. (2002) reported that only the oval-aligned arc type occurs on the dawn (dusk) oval side after one to two hours constant IMF with dominating northward IMF and dawnward (duskward) IMF. Often, oval-aligned arcs are clearly separated from the main oval during only some part of their life time, sometimes they seem to be a part of an extended oval side (e.g., Kullen et al., 2002). Our results are in agreement with the scenario of a strong tail twist being responsible for the poleward displacement of the polar cap (Kullen and Blomberg, 1996) and an oval-aligned arc occurring on its poleward boundary (Meng, 1981). As expected from observations (Cumnock et al., 2002), the bridge of closed field lines moving from dawn to dusk after a sign change from dawnward to duskward IMF B_y during northward IMF B_z indicates a moving polar arc. The model polar

arc is on both sides clearly separated from the main oval by regions of open field lines, as expected from observations by Huang et al. (1989) and others.

One major concern about the simulation results is that there are no field-aligned currents, that are associated with the poleward displaced closed field line region (bridge) where an oval-aligned (moving) arc is expected to occur. In fact, the FAC current pattern remains nearly unchanged for all runs, while the polar cap boundary changes drastically. The MHD simulations reproduce the large-scale field-aligned current pattern connected to the main auroral oval region fairly well, but small-scale current structures do apparently not appear. This is probably due to limitations of the model, maybe because of the low grid-resolution in the far tail (4-8 R_E). On the other hand, it cannot be ruled out that polar arcs are connected to upward currents having the return current near the same place such that no net current appears. Even in other MHD models there is a lack of FAC where a bridge of closed field lines appears inside the polar cap (e.g., in the simulation runs for observed polar arcs of Slinker et al. (2001), private communication). Interestingly, in a comparison between auroral images and ionospheric plasma convection by Chang et al. (1998) the plasma convection associated with a polar arc could not be resolved in SuperDARN measurements, which the authors claim may be due to the small width of the polar arc.

3.4 The topological connection between polar arcs and the magnetotail

The MHD simulations show that a small IMF clock angle causes a long tailward extension of the closed field line region and a strong twisting of the far-tail plasma sheet, independent on whether the small clock angle appears for a long time (constant IMF cases) or in a transitional state (IMF B_y sign-change cases). A long closed field line region and strongly twisted tail causes field lines originating in the far tail to map to high latitudes in the near-Earth region and in the ionosphere. The plasma sheet in the near-Earth tail is only weakly twisted such that the boundary of the closed field line region does not overlap with the plasma sheet boundary but is located in the near-Earth tail lobes.

While the reason for the lack of FAC at the location of a polar arc remains unclear to us, we believe that the MHD results are correct in the sense that the boundary of the large-scale FAC system does not overlap with the polar cap boundary in all cases. This idea is strengthened by the observational result by Elphinstone et al. (1990) where the main auroral oval (connected to upward FAC) is shown to keep its circular shape even for non-zero IMF B_y and positive IMF B_z, where a strong poleward displacement of the polar cap boundary is expected. We conclude (from mapping FAC to the tail) that the main auroral oval has its source region in the near-Earth region. A polewardly displaced polar cap boundary maps to the highly twisted distant tail and is a possible location for polar arcs to occur.

There are some discrepancies between simulation results and observations. For the constant IMF cases, the most favorable conditions for oval-aligned arcs have been found by observations to

occur around 45 degrees while the simulations suggest a clock angle around 10 degrees. Kullen et al. (2002) showed that during the time period of the statistical study, small clock angles are only slightly less common than clock angles around 45 degrees such that it is not due to the rare occurrence of small clock angles that oval-aligned arcs appear mostly for 45 degrees. In the IMF sign-change case the largest difference to real cases is the life time of the polar arc. Both deviations from observations may be connected to the unrealistically short tail of the MHD run. A longer region of closed field lines leads to the B_y sign reversal taking more time to move tailward, thus the polar arc exists longer, a longer region of closed field lines might lead to that in the 45° case even far-tail regions with a high twist map to the Earth leading to the same effect of the closed field line region extending to the lobes as in the 10° case.

4 Summary and Conclusions

Several MHD runs have been performed to examine the influence of constant and changing IMF B_y on the large-scale topology of the magnetosphere and the polar ionosphere. The constant IMF runs are done for IMF clock angles of 10°, 45°, 80° and 100°. The runs for changing IMF B_y consist of a fast and a slow IMF B_y sign change during northward IMF.

A dawn-duskward bending of the field lines and a twisting of the tail plasma sheet occur in all constant IMF runs, as expected for nonzero IMF B_y. Comparing the constant IMF runs for different IMF clock angles reveals that the closed field line region extends the farthest for small clock angles. In that case the downtail increasing twisting of the plasma sheet becomes very high at its tailward end. Field lines originating in the high-latitude part of the far tail map into the lobes of the near Earth tail. In the ionosphere the polar cap boundary shows a strong poleward displacement on the corresponding oval side. It is suggested that oval-aligned arcs may occur on the strongly poleward displaced boundary of the polar cap. This is in agreement with observations showing that these arcs often appear after hours of nearly constant IMF with a positive B_z and a nonzero B_y component. The simulation results indicate that oval-aligned arcs map into the highly twisted far-tail plasma sheet while the main oval maps to the near-Earth and mid-tail regions.

The simulation of an IMF B_y sign change during positive IMF B_z shows that such a sign reversal does not affect the entire tail at once but starts at the near-Earth tail flanks and then propagates both tailward and toward the tail center. A tailward moving cone of zero B_y penetration develops. Inside the cone, the penetration field and the tail twist are in opposite direction than outside the cone. During the tailward propagation of the sign-change region, the region of closed field lines increases far downtail until it returns to its original length. In an intermediate state the closed field line region is extremely long with the far-tail plasma sheet and the near-Earth plasma sheet being oppositely twisted. A complicated field line topology emerges. Closed field lines originating in the highly twisted far-tail plasma sheet bifurcate the near-Earth tail lobes and the polar cap. A bridge

of closed field lines in the polar cap moves within 50 minutes from one oval side to the other. This dawn-duskward moving bridge may be interpreted as the location where a moving polar arc may occur. Such a polar arc type appears typically after an IMF B_y sign change during predominately northward IMF. A comparison between a fast and a slow IMF B_y sign change shows that neither the magnetotail topology nor the polar arc life time and location are significantly different. Only the dawn-dusk width of the closed field line bridge and the length of the closed field line region are influenced by the speed of an IMF B_y sign change.

In summary, moving polar arcs and oval-aligned arcs have it in common that the IMF clock angle is small, either transitionally (moving polar arcs) or constantly (oval-aligned arcs), and the closed field line region extends far downtail and the plasma sheet is highly twisted at its tailward end. This tail topology causes field lines originating in the high latitude far-tail region to map high into the near-Earth tail lobes and poleward of the average polar cap boundary. The poleward displaced closed field line region is a probable location for polar arcs to occur.

Acknowledgements. We want to thank Minna Palmroth for executing the MHD runs.

References

Berchem, J., J. Raeder, M. Ashour-Abdalla, L. A. Frank, W. R. Peterson, K. L. Ackerson, S. Kokubun, T. Yamamoto, and R. P. Lepping, The distant tail at 200 Re: Comparison between Geotail observations and the results from a global magnetohydrodynamic simulation, *J. Geophys. Res.*, *103*, 9121, 1998.

Borovsky, J. E., M. F. Thomsen, and R. C. Elphic, The driving of the plasma sheet by the solar wind, *J. Geophys. Res.*, *103*, 17:617, 1998.

Brecht, S. H., J. Lyon, J. A. Fedder, and K. Hain, MHD model of IMF By influence on tail, *J. Geophys. Res.*, *103*, 17:617, 1981.

Chang, S.-W. et al., A comparison of a model for the theta aurora with observations from Polar, Wind and SuperDARN, *J. Geophys. Res., 103*, 17:367, 1998.

Cowley, S. W. H., Magnetospheric asymmetries associated with the y-component of the IMF, *Planet. Space Sci.*, *29*, 79, 1981.

Craven, J. D., J. S. Murphree, L. A. Frank, and L. L. Cogger, Simultaneous optical observations of transpolar arcs in the two polar caps, *Geophys. Res. Lett.*, *18,* 2297, 1991.

Cumnock, J. A., J. R. Sharber, R. A. Heelis, M. R. Hairston, and J. D. Craven, Evolution of the global aurora during positive IMF B_z and varying IMF B_y conditions, *J. Geophys. Res.*, *102*, 17:489, 1997.

Cumnock, J. A., J. R. Sharber, R. A. Heelis, L. G. Blomberg, G. A. Germany, J. F. Spann, and W. R. Coley, Interplanetary magnetic field control of theta aurora development, *J. Geophys. Res.*, *107*, 10:1029, 2002.

Elphinstone, R. D., K. Jankowska, J. S. Murphree, and L. L. Cogger, The configuration of the auroral distribution for interplanetary magnetic field Bz northward, 1, IMF Bx and By dependencies as observed by the Viking satellite, *J. Geophys. Res.*, *95*, 5791, 1990.

Fairfield, D. H., On the average configuration of the geomagnetic tail, *J. Geophys. Res.*, *84*, 1950, 1979.

Fedder, J. A., and J. G. Lyon, The Earth's magnetosphere is 165 Re long: Self-consistent currents, convection, magnetospheric structure, and processes for northward interplanetary magnetic field, *J. Geophys. Res.*, *100*, 3623, 1995.

Frank, L. A., et al., The theta aurora, *J. Geophys. Res.*, *91*, 3177, 1986.

Frank, L. A., and J. D. Craven, Imaging results from Dynamics Explorer 1, *Rev. Geophys. , 26*, 249, 1988.

Gombosi, T. I., D. L. DeZeeuw, R. M. Hberli, K. G. Powell, and P. Song, The length of the magnetotail for northward IMF: Results of 3D MHD simulations, in *Physics of Space Plasmas,*, ed. T.Chang and J.R. Jasperse, vol. 15, p. 121, MIT Press, Cambridge, 1998.

Huang, C. Y., J. D. Craven, and L. A.Frank, Simultaneous observations of a theta aurora and associated magnetotail plasmas, *J. Geophys. Res.*, *94*, 10137, 1989.

Janhunen, P., GUMICS-3 - A global ionosphere-magnetosphere coupling simulation with high ionopheric resolution, *ESA Sympos. Proc., SP-392*, 233, 1996.

Janhunen, P., and Palmroth, M., Some observational phenomena are well reproduced by our global MHD while others are not: Remarks on what, why and how, *Adv. Space Res.*, *28*, 1685, 2001.

Kan, J. R., and W. J.Burke, A theoretical model of polar cap auroral arcs, *J. Geophys. Res., 90*, 4171, 1985.

Kaymaz, Z., and G. L. Siscoe, Open geometry of the magnetotail cross section, *J. Geophys. Res.*, *99*,

14:829, 1998.

Kaymaz, Z., G. L. Siscoe, J. G. Luhmann, R. P. Lepping, and Ch. T. Russell, Interplanetary magnetic field control of magnetotail magnetic field geometry: IMP 8 observations, *J. Geophys. Res.*, *99*, 11:113, 1994.

Kaymaz, Z., G. L. Siscoe, J. G. Luhmann, J. A. Fedder, and J. G. Lyon, Interplanetary magnetic field control of magnetotail field - IMP-8 data and MHD model compared, *J. Geophys. Res.*, *100*, 17:163, 1995.

Kullen, A., The connection between transpolar arcs and magnetotail rotation, *Geophys. Res. Lett.*, *27*, 73, 2000.

Kullen, A., and L. G. Blomberg, The influence of IMF By on the mapping between the Earth's magnetotail and its ionosphere, *Geophys. Res. Lett.*, *23*, 256, 1996.

Kullen, A., M. Brittnacher, J. A. Cumnock, and L. G. Blomberg, Solar Wind Dependence of the Occurrence and Motion of Polar Auroral Arcs: A Statistical Study, *J. Geophys. Res., 107*, 1362, 2002.

Lui, A. T. Y., Polar wind influence on magnetotail configuration and dynamics, *Solar wind magnetosphere coupling*, Ed. Y.Kamide and J.A. Slavin, 671, 1986.

MacWan, S. E., A determination of twisting of the Earth's magnetotail at distances $115 - 220 R_e$: ISEE 3, *J. Geophys. Res.*, *97*, 19.239, 1992.

Makita, K., C. I. Meng, and S. I. Akasofu, Latitudinal electron precipitation patterns during large and small IMF magnitudes for northward IMF conditions, *J. Geophys. Res.*, *93*, 97, 1988.

Meng, C.-I., Polar cap arcs and the plasma sheet, *J. Geophys. Res.*, *8*, 273, 1981.

Newell, P. T., D. Xu, C.-I. Meng, and M. G. Kivelson, Dynamical polar cap: A unifying approach, *J. Geophys. Res., 102*, 127, 1997.

Ogino, T., A three dimensional MHD simulation of the interaction of the solar wind with the Earth's magnetosphere: The generation of field aligned currents, *J. Geophys. Res.*, *91*, 6791, 1986.

Ogino, T., R. J. Walker, and M. Ashour-Abdalla, A global magnetohydrodynamic simulation of the magnetosheath and magnetosphere when the interplanetary magnetic field is northward, *IEEE Trans. Plasma Sci.*, *20*, 6, 817,1992.

Owen, C. J., J. A. Slavin, I. G. Richardson, N. Murphy, and R. J. Hynds, Average motion, structure and orientation of the distant magnetotail determined from remote sensing of the edge of the plasma sheet boundary layer with $E > 35$ keV ions, *J. Geophys. Res.*, *100*, 185, 1995.

Raeder, J., R. J. Walker, and M. Ashour-Abdalla, The structure of the distant geomagnetic tail during long periods of northward IMF, *Geophys. Res. Lett.*, *22*, 349, 1995.

Rezhenov, B. V., A possible mechanism for theta aurora formation, *Ann. Geophys., 13*, 698, 1995.

Russell, C. T., The configuration of the magnetosphere, in *Critical Problems of Magnetospheric Physics,* ed. E. R. Dyer, National Academy of Sciences, Washington DC, 1, 1972.

Sergeev, V. A., Penetration of the By-component of the interplanetary magnetic field (IMF) into the tail of the magnetosphere, *Geomagn. Aeronom.*, *27*, 4,1987.

Sibeck, D. G., J. A. Slavin, E. J. Smith, and B. T. Tsurutani, Twisting of the geomagnetic tail, *Solar Wind-Magnetosphere Coupling*, Ed. Y. Kamide and L. A. Slavin, 731, 1986.

Slinker, S. P., J. A. Fedder, D. J. McEwen, Y. Zhang, and J. G. Lyon, Polar cap study during northward

interplanetary magnetic field on 19 January 1998, *Physics of Plasmas*, *8*, 1119, 2001.

Song, P, D. L. DeZeeuw, T. I. Gombosi, C. P. T. Groth, and K. G. Powell, A numerical study of solar wind-magnetosphere interaction for northward interplanetary magnetic field, *J. Geophys. Res.*, *104*, 28:361, 1999.

Tanaka, T., Configuration of the magnetophere-ionosphere convection system under northward IMF conditions with nonzero IMF B_y, *J. Geophys. Res.*, *104*, 14:683, 1999.

Tsyganenko, N. A., A magnetospheric magnetic field model with a warped tail current sheet, *Planet. Space Sci.*, *37*, 5, 1989.

Tsyganenko, N. A., Global configuration of the magnetotail current sheet as derived from Geotail, Wind, IMP 8 and ISEE 1/2 data, *J. Geophys. Res.*, *103*, 6827, 1998.

Valladares, C. E., H. C. Carlson Jr., and K. Fukui, Interplanetary magnetic field dependency of stable Sun-aligned polar cap arcs, *J. Geophys. Res.*, *99*, 6247, 1994.

Voigt, G.-H., and R. V. Hilmer, The influence of the IMF By component on the Earth's magneto-hydrostatic magnetotail, *Magnetotail physics*, Ed. A.T.Y. Lui, Laurel Maryland, 1987.

Walker R. J., R. L. Richard, T. Ogino, and M. Ashour-Abdalla, The response of the magnetotail to changes in the IMF orientation: The magnetotail's long memory, *Phys. Chem. Earth. Pt. C*, *24*, 221, 1999.

Tables

Table 1. The length of the closed field line region for constant IMF clock angles.

clock angle	[1]100°	[1]80°	[2]45°	[1]45°	[1]10°
CFR length	20 R_E	20 R_E	28 R_E	34 R_E	85 R_E

[1]|IMF| = 5.1 nT [2]|IMF| = 7.1 nT

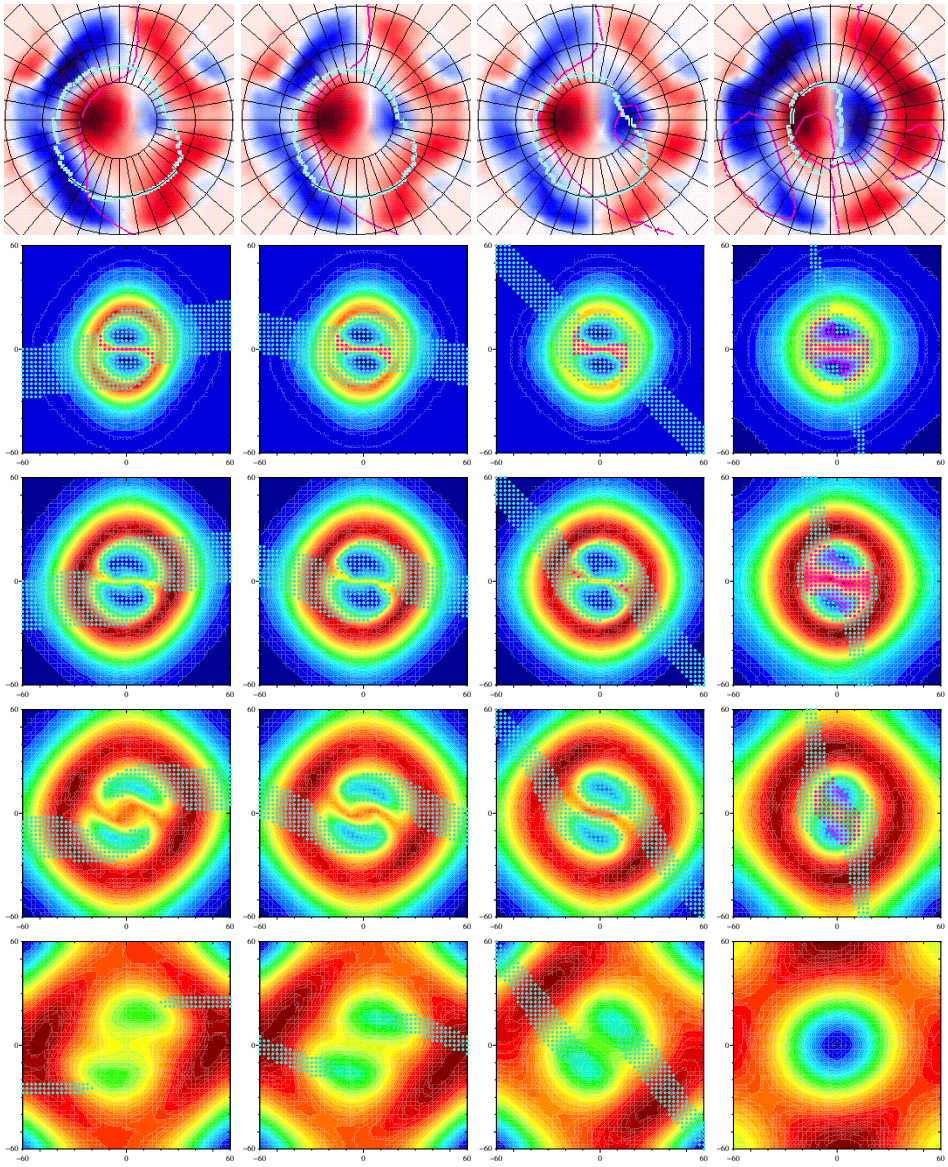

Fig. 1. Simulation results after two hours of steady-state IMF. The columns (from left to right) show the magnetosphere for IMF clock angles of 100°, 80°, 45° and 10° and an IMF magnitude of 5.1 nT. The first row contains plots of the northern ionosphere with the open/closed field line boundary (light blue line) overlaid on the upward (blue) and downward (red) field-aligned currents. The plots give a 2D view on the polar cap in geomagnetic coordinates with noon pointing to the top. The second to last row show tail cross sections at $x = -10, x = -30, x = -60$ and $x = -120\mathrm{R_E}$ (looking downtail in GSM coordinates). In the tail plots the regions of closed (pink dots) and open field lines (light blue dots) are overlaid on plasma pressure isocontour lines (in arbitrary units).

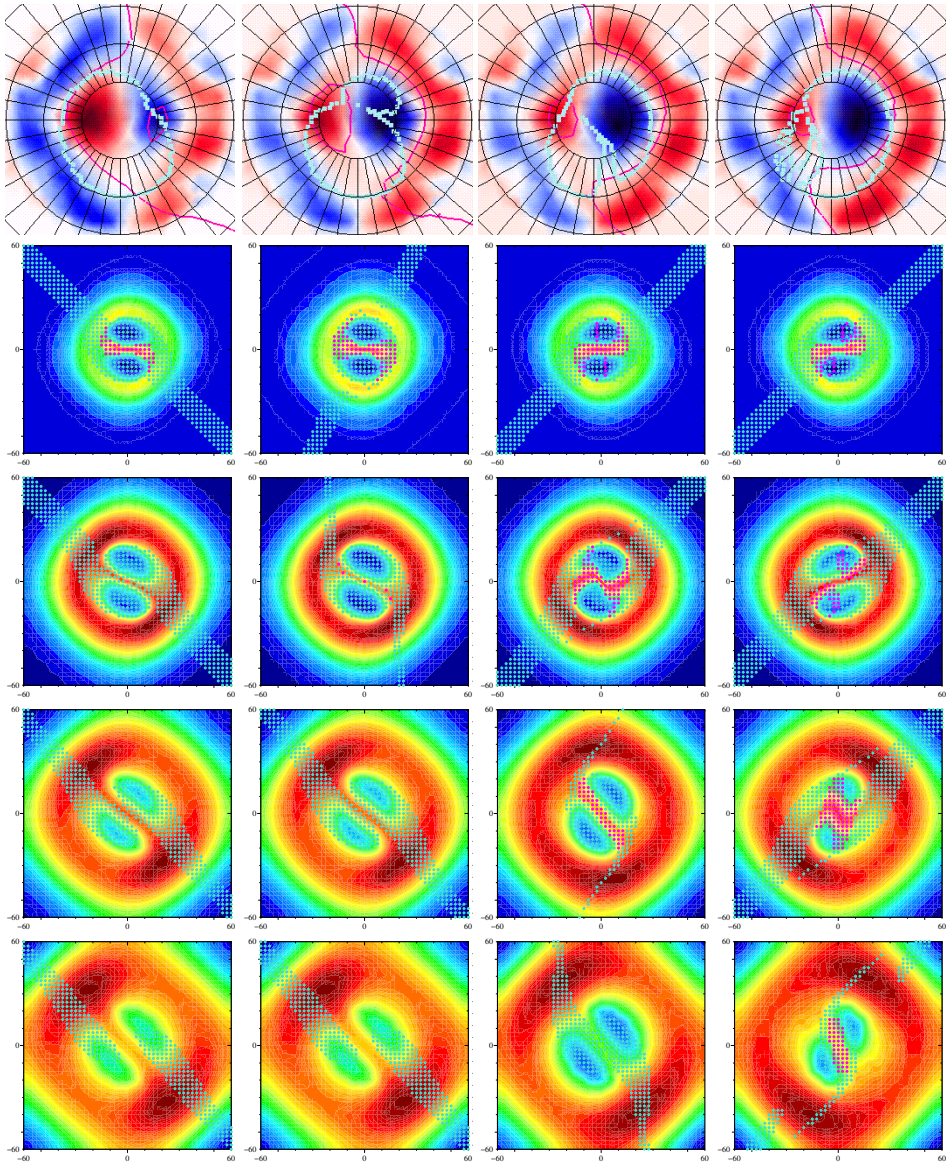

Fig. 2. Simulation results for an MHD run with a fast (2 minutes) IMF B_y sign change from -5 nT to $+5$ nT after two hours constant IMF and constant positive IMF B_z of $+5$ nT. The columns (from left to right) show the state of the magnetosphere $-8, 7, 22$ and 37 minutes after the center of the IMF B_y sign-change region ($B_y = 0$) has passed the dayside magnetopause (at $x = 10\mathrm{R_E}$). The first row shows the northern ionosphere. The second to last row show tail cross sections at $x = -10, x = -30, x = -60$ and $x = -90\mathrm{R_E}$. The plots are defined in the same way as in Figure 1.

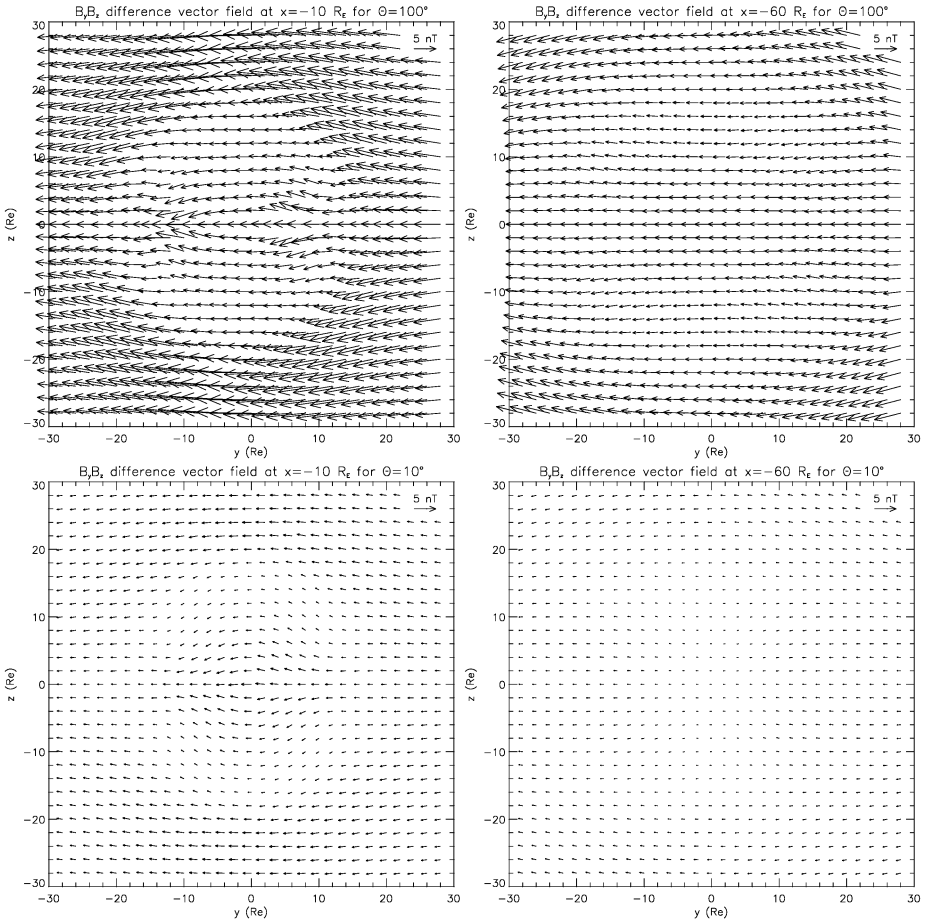

Fig. 3. The IMF penetration into the magnetotail at different tail cross sections for two constant IMF runs. The plots are produced by mirroring the $B_y B_z$ vector components of the corresponding tail cross section along the z-axis, subtracting the mirror vectors from the original vectors and dividing the results by two.

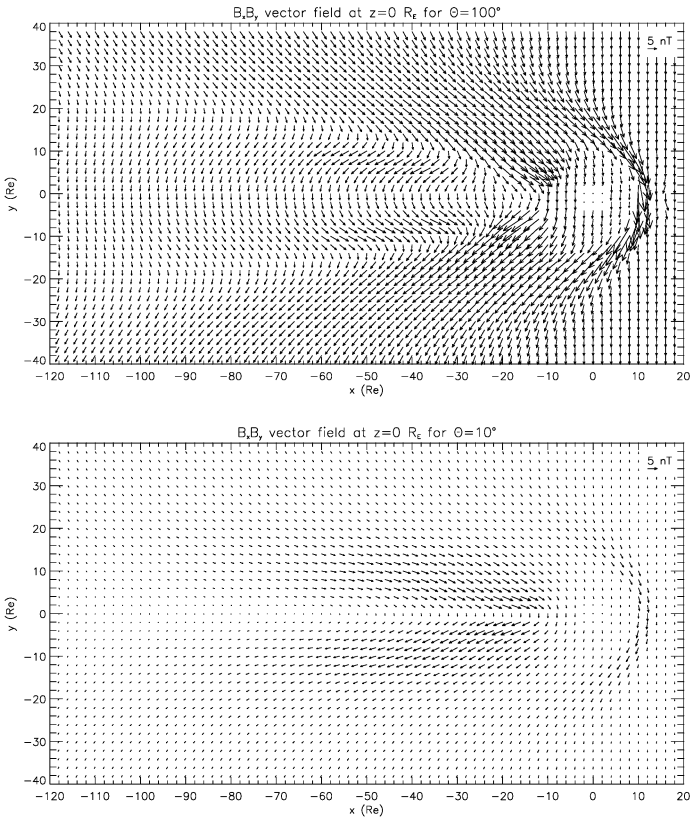

Fig. 4. The magnetic field in the equatorial plane for two constant IMF runs. The component vectors are plotted every 2 R_E down to a distance of 4 R_E from the Earth center.

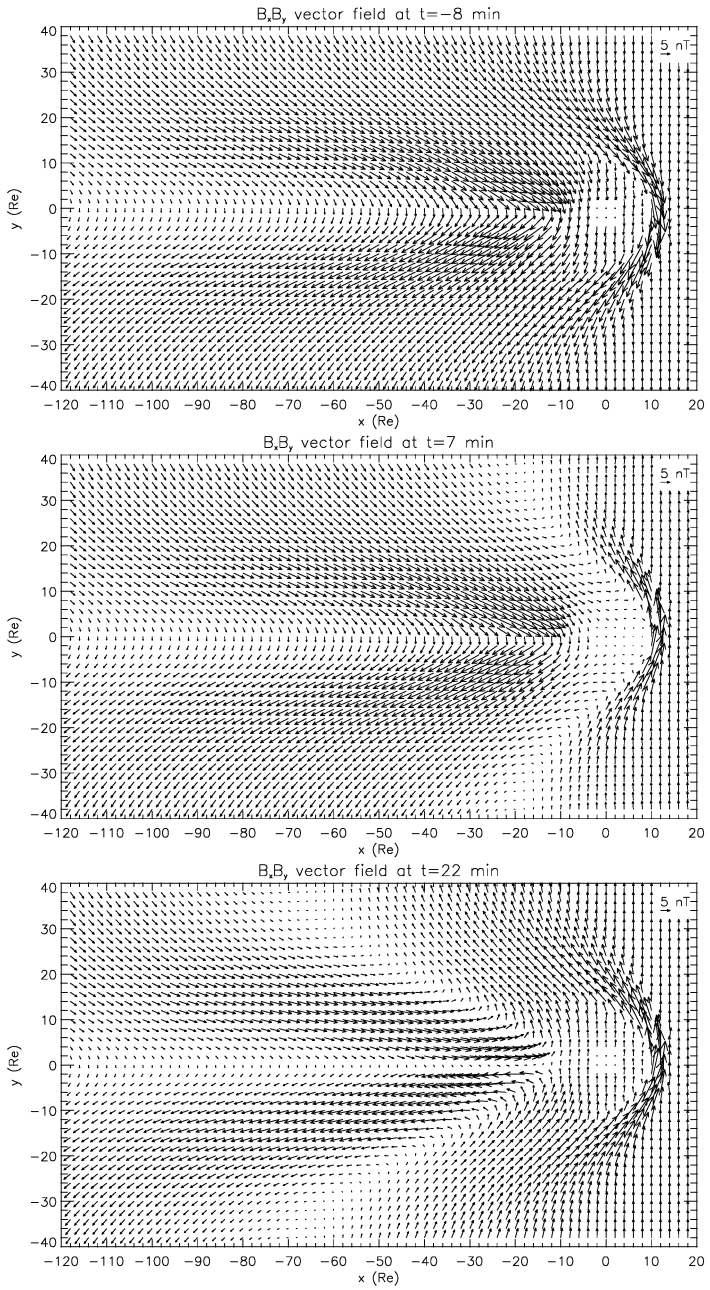

Fig. 5. The magnetic field in the equatorial plane for different points of time during the fast IMF B_y sign-change run.

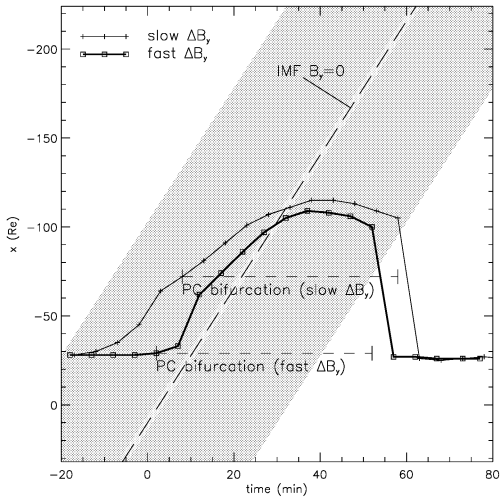

Fig. 6. The length of the closed field line region versus time during the fast and the slow IMF B_y sign-change run. The time is given here in minutes after the center of the sign-change region has passed the dayside magnetopause. The tailward propagating IMF sign-change region and the time interval during which a polar cap bifurcation occurs are marked for both runs.

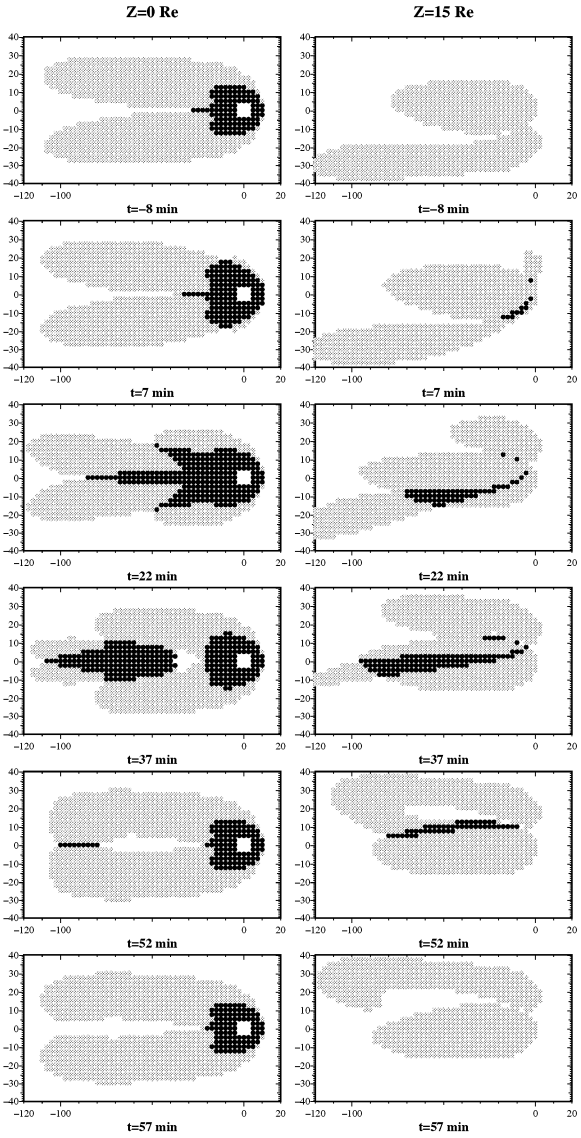

Fig. 7. Open (grey) and closed (black) field line regions in the equatorial plane (left column) and above it (right column) for different points of time during the fast IMF B_y sign-change run.

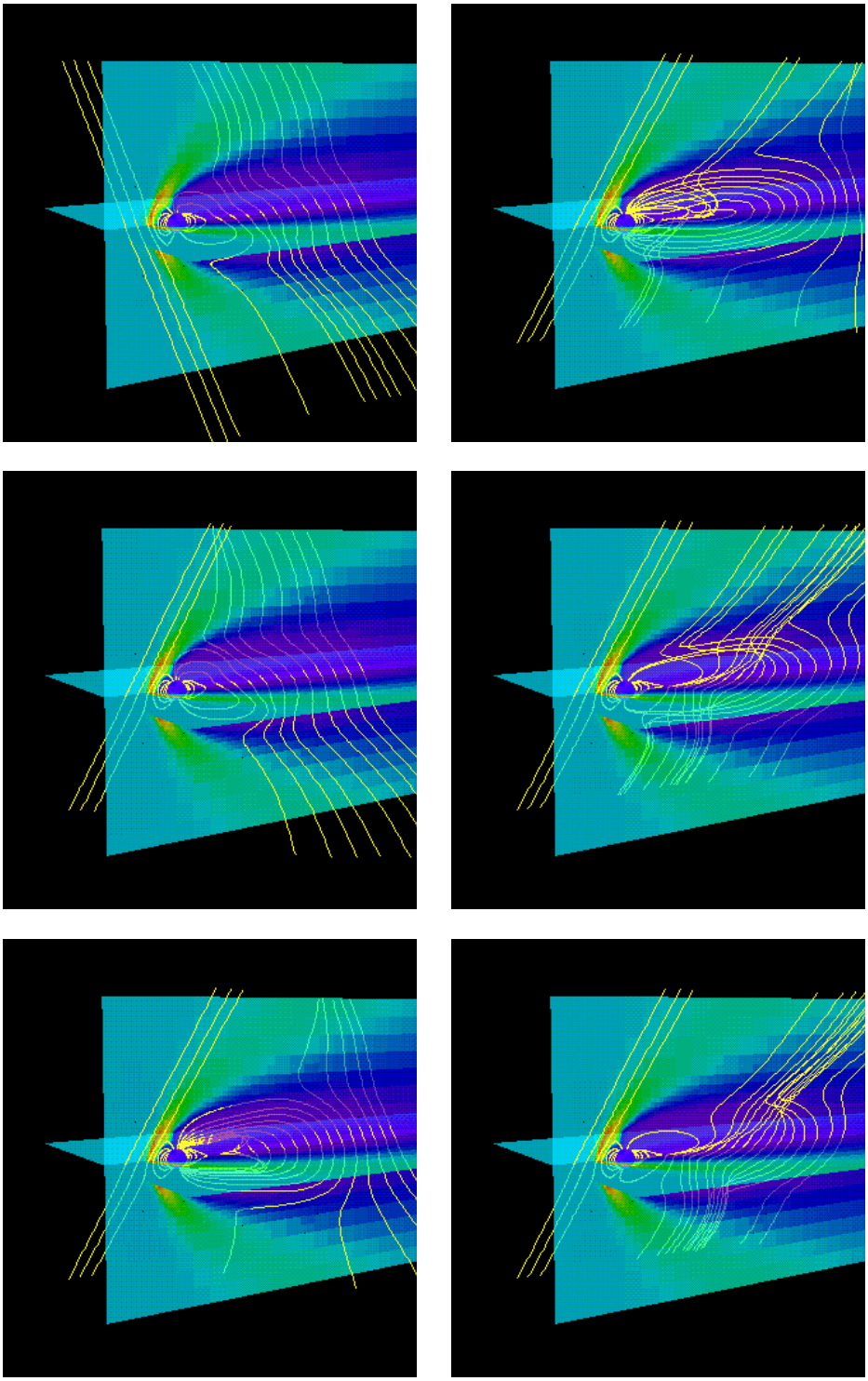

Fig. 8. A 3D view on field lines crossing the x-axis for the fast IMF B_y sign change run. The plots show the state of the magnetosphere -8, 7, 22 minutes (first column from top to bottom) and 37, 52, 57 minutes (second column, from top to bottom) after the center of the IMF B_y sign-change region ($B_y = 0$) has passed the dayside magnetopause.

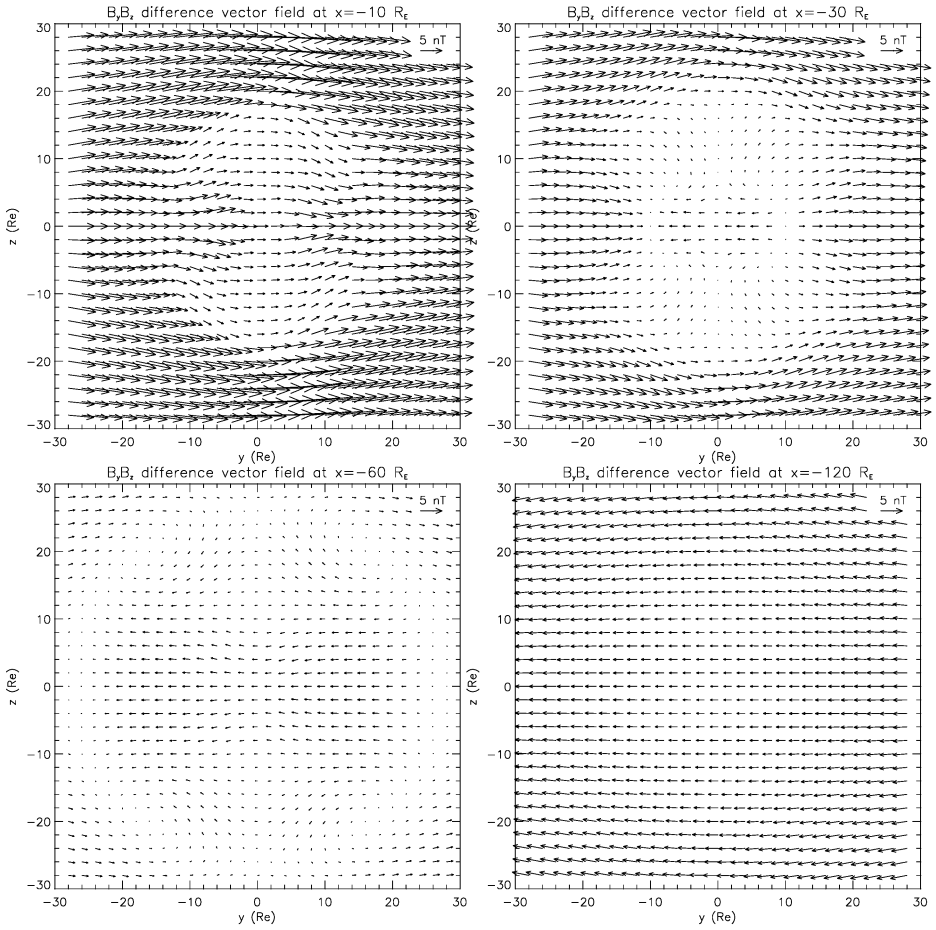

Fig. 9. The IMF penetration into the magnetotail at different tail cross sections during the fast IMF B_y sign-change run. The plots are produced in the same way as Figure 3 and show the penetration field 22 minutes after the center of the sign-change region has passed the dayside magnetopause.

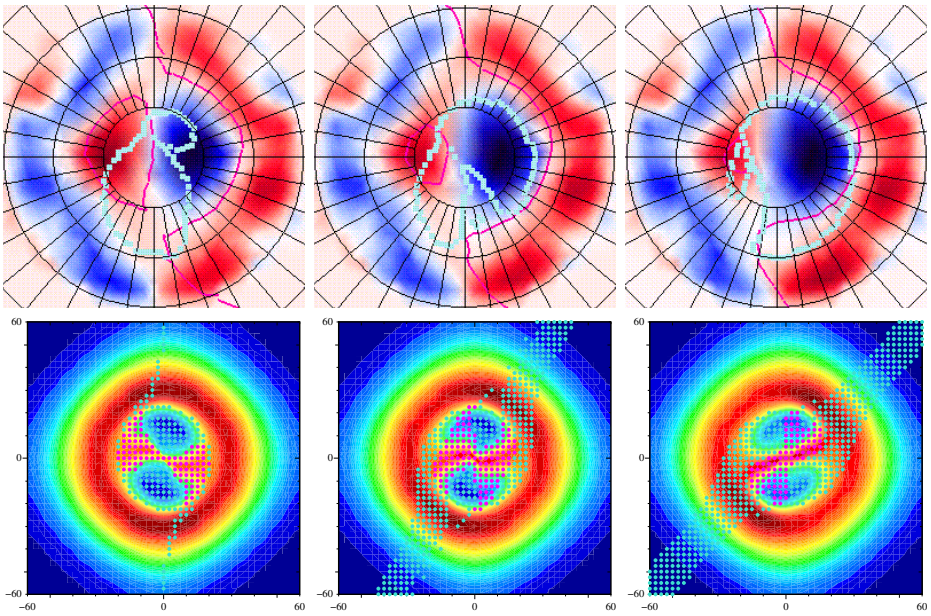

Fig. 10. Simulation results for an MHD run with a slow (1 hour) IMF B_y sign change from -5 nT to $+5$ nT after two hours constant IMF and constant positive IMF B_z of $+5$ nT. The columns (from left to right) show the state of the magnetosphere $13, 28$ and 43 minutes after the center of the IMF B_y sign-change region has passed the dayside magnetopause. The first row shows the northern ionosphere and the second row shows tail cross sections at $x = -30\mathrm{R_E}$. The plots are defined in the same way as in Figure 1.

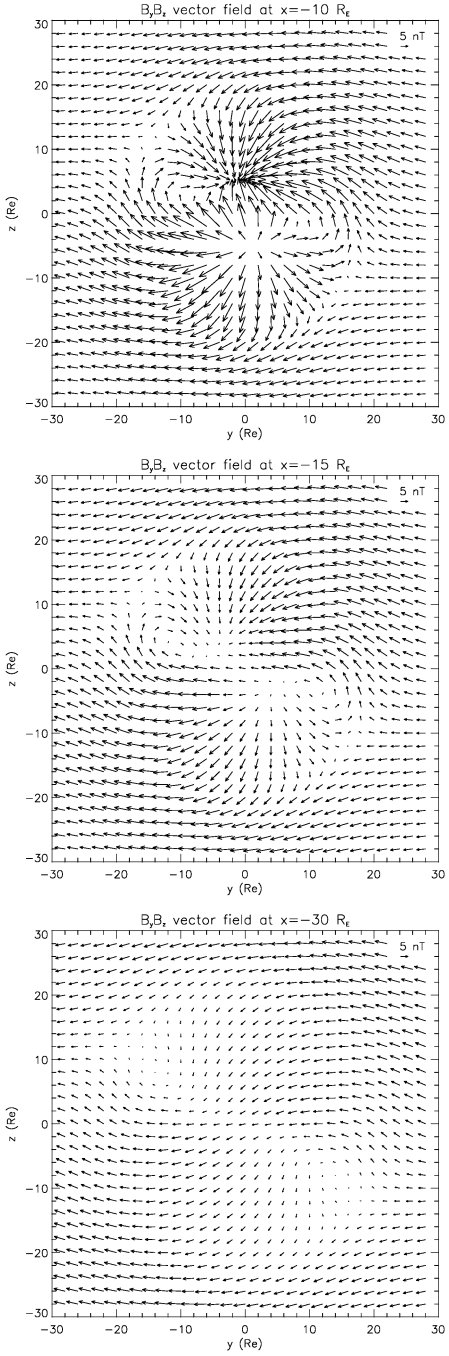

Fig. 11. The magnetic field at different tail cross sections after two hours constant IMF with an IMF clock angle of 90° and a magnitude of 5.0 nT.